Photon Migration and Imaging of Objects Hidden in Layered and Bulk Random Scattering Media

by

JEAN J. DOLNE

A dissertation submitted to the Graduate faculty in Engineering in partial fulfillment of the requirements for the degree of Doctor of Philosophy, The City University of New York.

1996

This manuscript has been read and accepted for the Graduate Faculty in Engineering in satisfaction of the dissertation requirement for the degree of Doctor of Philosophy.

12/11/95
Date

Chair of Examining Committee
Professor R. R. Alfano

12/11/95
Date

Executive Officer
Dean G. Lowen

Professor A. Z. Genack

Professor J. Gersten

Professor P. P. Ho

Professor F. Liu

Professor J. Malinsky

Professor K. Shum

Supervisory committee

The City University of New York

Abstract

Photon Migration and Imaging of Objects Hidden in Layered and Bulk Random Scattering Media

by

JEAN J. DOLNE

Advisor: Prof. R. R. Alfano

Three wavelengths of laser light operating in the CW mode and a spatial filter system were used to image an object hidden behind a random scattering medium. The best image contrast was obtained when the spatial filter aperture was closed to allow only the lowest spatial frequencies representing mostly the ballistic/snake light to pass through and for the longest wavelength of radiation.

A two-layered medium was reconstructed using the Fourier transform of the diffusion equation. The inverse parameters of the two layers were found to be unique when the top layer thickness was less than half the source detector separation.

Light scattered all around a random scattering medium has been measured by a multiple-fiber collection system. It was found that the scattered signal decreased all around the medium. A novel method to measure the optical parameters such as the

transport mean free path and the absorption length of a scattering medium has been found. This method uses only the peak intensity and the risetime of the pulse intensity profile.

It has been shown that light scattering data around the reference medium can be "measured" by using only one detector at an appropriate position and an appropriate theory.

The angular dependence of scattered light was measured. It was found that in the non-diffuse region, the detected light intensity depended strongly on the orientation of the detector. In the diffuse region, however, there was only a negligible angular dependence in the scattered intensity profile.

The photon trajectories that photons follow inside a scattering medium have been measured. It has been found that these paths arrive at specific times and angles at the detector. These specific times of arrival make it possible to locate a hidden object inside a scattering medium.

The transmitted light scattered from random media of different sizes has been found to be independent of the sizes of the particles in the diffusion region.

Acknowledgments

I consider myself fortunate to have had the opportunity to study under the guidance of Professor R. R. Alfano. I greatly appreciate his unrelenting work to stay at the top of the field. His constant availability, his bright insights, his deep involvement, and his creative imagination are the reasons why this work has been possible. I am particularly grateful to Prof. F. Liu for his vast help and ideas and for providing many software programs used in this thesis.

I thank Professors A. Z. Genack, Joel Gersten, Ping P. Ho, Kai Shum, and Joseph Malinski for being on my doctoral dissertation committee.

I would like to thank all the members of IUSL, particularly Prof. P. P. Ho and Dr. B. B. Das, for their general advice and help during the course of this research work. I thank Dr. A. Ya. Polishchuk for his immense work that has made the layer reconstruction possible and for his discussions on photon paths.

I would like to thank my wife and my daughter for their support, for their encouragement, for their advice, and for puting through during all this thesis work.

I thank God for giving me strength, patience, health, and determination throughout the years.

I would like to thank CASI for providing my support for this thesis study.

This thesis was made possible with the financial support from NSF, NASA, ONR, and Mediscience Technology Corp..

Table of Contents

List of Figures

Chapter 1

Introduction

1.1 Background

Over the years, scientists have been curious about light scattering phenomena. One great puzzle for the scientists in the last century was the blue of the sky. Newton had suggested that it was due to interference of rays reflected from front and back surfaces of water droplets but later Rayleigh correctly noted that it was due to scattering of the sun light[1-2]. The blue of the sky is explained by the scattering of the blue light more than the other light colors in the sunlight. When one looks at the sky (not directly at the sun), the only light that can be detected by the eye is the scattered light. The blue light having the shortest wavelength is the most scattered and is therefore mostly detected. Over the past several years, many areas of science and engineering have showed increased interest in the study of scattering of electromagnetic waves for several applications. Communication engineers are concerned with the phase and amplitude fluctuations of waves as they propagate through atmospheric and ocean turbulence. Radar engineers are concerned with scattering from storms, rain, snow, or hail.

With the recent advent of lasers and ultrafast detection systems, light propagation in highly scattering media have received considerable attention because of its possible applicability to medical diagnosis [3-4] such as the detection of breast tumors or cancers. Studies have shown that one in ten women develop breast cancer which is the number one killer of women over forty. Women aged over 35 have often been advised to go for a breast screening examination. Breast screening has usually been performed using

high energy sources such as x-rays. Although these X-ray sources can yield high quality images, they are nevertheless ionizing. This current technology can become the cause of the breast cancer when one is subjected to huge level of radiation for a long time. In 1976, Bailar[5], reflecting on the radiation risk of breast screening mammography, voiced the possibility that routine mammography caused more cancer deaths than it prevented. In 1977, investigators from the National Cancer Institute have reported for instance an excess of breast cancers in three populations previously exposed to radiation[5]: (1) Japanese women ten years or older who had survived atomic bomb blasts in Hiroshima and Nagasaki; (2) women who had had extensive fluoroscopy examinations to monitor pneumothorax treatments for tuberculosis; and 3) women who had been treated by radiation therapy for postpartum mastitis. More recently, reports about the high proportion of women in Long Island (New York) with respect to the rest of the population affected by breast cancer have caused great alarm. Although the dose of radiation women are exposed to during an X-Ray mammogram is much less than in the cases cited above, one nevertheless needs to be concerned about taking mammograms too often. One alternative to the radiation problem of the current technologies may be to use light because light is not ionizing.

Using light to detect tumors inside human tissues has caught the attention of scientists as far back as the middle of the nineteenth century. In 1843, Curling reported the use of a flare lantern to transilluminate the scrotum of his patients to screen for tumors. A visible light system known as diaphanography to detect breast tumors has resulted in the first half of the twentieth century[6]. This system failed to resolve deep structures such as tumors inside human tissues. The image information from the deep structures has been lost in

the diffuse background noise caused by multiple scattering of light. Transillumination imaging is based on the component of light travelling the straight path from source to detector projecting a shadow of the object on the detector. When the object is placed inside a non-scattering medium such as water, for instance a fish inside a fish tank filled with water, the edge details of the object can be clearly seen by a detector placed on the medium. When the medium is highly scattering, however, the details of the edges of the object are lost in the multiply scattered light that contributes to the diffuse noise. Inside a medium of tissue, photons undergo multiple scattering. The average depth that a photon can travel before being randomized is less than 1mm. The multiple scattering of the light washes out the image carrying light.

Most recently, groups from all over the world have used various optical techniques to reduce the amount of multiply scattered light detected and have used different parts of the signal profile to reconstruct a hidden object inside the scattering medium with different degrees of resolutions. Liu, Yoo, and Alfano[7] have unburied an image signal from a highly scattering medium through the use of absorption. The absorption technique is based on the observation that multiply scattered light travels a much longer distance than the ballistic light. By including more absorption into the scattering medium, the light travelling longer distance will be preferably absorbed. Wang, Ho, and Alfano[8] have showed that the image carrying light can be preferably detected through the use of an ultrafast optical Kerr gate. Fujimoto et al.[9-10] have used low coherence interferometry to image internal tissue microstructures in mammalian tissues and to image the anterior eye and retina. This method is based on combining the light back-scattered from a sample and the light returning from a calibrated reference arm. An interferometric signal is

generated when the distance to a site in the sample matches the length of the reference arm to within the source coherence length. Since light multiply scattered travels much longer distances than the image carrying light, an interferometric pattern for the image carrying light can be obtained by matching the reference arm length to the sample arm focal plane distance.

Light propagating through a scattering medium inside a slab of thickness L, scattering length, l_s, absorption length, l_a, and transport mean free path, l_t breaks up into several components: a ballistic component that travels through the medium undeviated reaches the detector first and is attenuated as $e^{-L(\frac{1}{l_s}+\frac{1}{l_a})}$. In optical tomography, the media considered are slightly absorbing. The attenuation of the ballistic light is therefore mainly due to scattering. A snake component(I_s) that scatters mostly in the forward direction, is attenuated as $I_s = A(\Delta t)e^{-b(\Delta t)L/l_t}$ and reaches the detector right after the ballistic light. The constants $A(\Delta t)$ *and* $b(\Delta t)$ depend on the time window Δt after the ballistic light arrival. Finally, a diffuse component goes all over the medium and arrives much later[11-12]. These components vary according to the key properties of the random medium. The key properties of the random medium are: the scattering mean free path, l_s, the transport mean free path, l_t, and the absorption length, l_a.

The scattering length is the average distance that the photons travel between scattering. This length is given by: $l_s = 1/\rho\sigma_s$, where ρ is the number of scatterers per unit volume (number density), σ_s is the scattering cross section of a single scatterer. The scattering cross section depends on the shape, the size, and the index of refraction of the particle with respect to the background medium. The scattering cross section produces the total observed scattered power at all angles around the particle. It is related to the

differential cross section by: $\sigma_s = \int_{4\pi} \sigma_d d\omega$ where $d\omega$ is the differential solid angle. The differential cross section is the cross section that would cause some uniform scattered power flux density over one steradian of solid angle about the direction of observation $\vec{s}$.

For a particle much smaller than a wavelength, the scattering is isotropic and is inversely proportional to the fourth power of the wavelength and proportional to the square of the volume of the particle [1] ($\sigma_s \approx \frac{V^2}{\lambda^4}$). If the size of the particle is much greater than a wavelength, the light is scattered mostly in the forward direction (anisotropic scattering) within an angle $1.22\lambda/d$ where λ is the wavelength of radiation, and d is the diameter of the particle. The scattered cross section is also almost equal to the geometric cross section of the particle.

The transport mean free path is the distance after which the photon direction is randomized and is defined as the distance between off angle scattering events given by $l_t = 1/n\sigma_m$ where σ_m is the momentum transfer cross section. The momentum transfer cross section is defined as the light scattered in all directions except the forward direction and is given by:

$$\sigma_m = \int \sigma_d(\theta, \phi)(1 - cos\,\theta) sin\,\theta d\theta d\phi \,. \tag{1.1}$$

The transport mean free path is related to the scattering mean free path through $l_t = \frac{l_s}{1-g}$, where g, the anisotropy factor, is the average of the cosine of the scattering angle, and is given by:

$$g = \langle cos\,\theta \rangle = \frac{\int \sigma_d(\theta, \phi) cos\theta\, sin\,\theta\, d\theta d\phi}{\int \sigma_d(\theta, \phi)\, sin\,\theta\, d\theta d\phi} \,. \tag{1.2}$$

For the case of isotropic scattering, g=0 and $l_t = l_s$. The photon direction is therefore randomized after one scattering. For purely forward or backward scatterings the anisotropy factor g is equal to 1 and -1, respectively. As g approaches 1, l_t approaches ∞. This means that for purely anisotropic media, g=1, the photon must encounter infinitely many scatterers before its direction is randomized.

For particle of arbitrary shape, it is not yet possible to calculate the differential cross section. For spherical particles that are used in this thesis, solutions are given from Mie theory[1-2].

In most cases, light propagation in random scattering medium can not be described exactly using analytical methods. Approximations such as transport theory, diffusion, Kubelka-Munk, Twersky are often used to investigate light propagation in scattering media[1, 13-16].

CW light have often been used to image a hidden structure inside some scattering medium. This is possible only if the ballistic component is greater than the diffuse component. For media of thicknesses many times the transport mean free path length, mainly diffuse noise will be detected; the ballistic signal decays as $e^{-\frac{L}{l_t}-\frac{L}{l_a}}$ and can not be separated from the diffuse signal. With the advent of ultrashort lasers and ultrafast detection, it has become possible to detect the ballistic light separately from the diffuse light because the ballistic light reaches the detector much earlier than the diffuse light. This technique has found wide practices in the optical community in the search for better imaging contrasts[17-19]. Different portions of the scattered pulse profile have been used to image a hidden object. In this thesis, the ballistic, snake, and diffuse components of the scattered signal will be used to image an object hidden inside or behind a scattering

medium.

1.2 Thesis Statement and Organization

This thesis will investigate experimentally and theoretically light propagation through various types of highly scattering media using pulse and CW light at different laser wavelengths in the NIR. It focuses on detecting objects hidden inside or behind highly scattering media. It will cover scattered light in the forward and backward directions for different concentrations of scattering media. The organization of this thesis is as follows:

Chapter 2 reviews the theoretical model that will be used in later chapters. The transport mean free path and the anisotropy factor are found from Mie theory. The transfer equation is derived heuristically. For highly scattering media, the transfer equation is approximated by the diffusion equation.

Chapter 3 covers the steady state imaging of an object hidden behind a highly scattering medium. Different wavelengths in the visible to NIR regions are studied. The absorption of water in the NIR region is taken advantage of to eliminate some diffuse noise. To obtain a better signal to noise ratio, a spatial filter is used in the Fourier plane of the 4–F system. The spatial filter removes the diffuse light that falls on it and lets through the ballistic/snake light.

Chapter 4 presents a layered random medium. Highly scattering medium on top of a solid chunk of wax is considered. The transport mean free path, l_t and the index of refraction, n of the two layers are different. The thickness and the optical parameters of the different layers are reconstructed from the back-scattered intensity profiles using the diffusion model approach for layers.

Chapter 5 describes photon migration in random media as these media become more or less scattering. It is shown, for a slab model, that scattered light do not increase in the forward nor in the backward directions when the medium becomes more and more scattering. In fact, both forward and back scattered light decrease. A novel way of obtaining the parameters of the scattering medium is obtained.

Chapter 6 shows the angular dependence of the scattered light in the non-diffuse region which is an indication that there may be groups of photons following very specific paths inside the scattering medium.

Chapter 7 presents the notion of most favorable paths that groups of photons may follow inside some scattering medium given a source detector configuration. It is shown that these photon paths arrive at specific times at the detector and that it is possible to probe different depths in the scattering medium by considering different times of photon arrival.

Chapter 8 summarizes the results of this thesis study and chapter 9 introduces some future research directions.

1.3 References

1. A. Ishimaru, *Wave propagation and scattering in random media*, (Academic Press, New York, 1978).

2. H. C. van de Hulst, *Light Scattering by Small Particles*, (Dover, New York, 1981).

3. For recent references, see OSA Proceedings on Advances in Optical Imaging and Photon Migration, edited by R. R. Alfano (Optical Society of America, Washington, DC 1994) Vol. 21.

4. See SPIE Proceedings on Photon Migration and Imaging in Random Media and Tissues, edited by B. Chance, R. R. Alfano (SPIE, Washington, DC, 1993) Vol. 1888.

5. R. L. Egan, *Breast Imaging: Diagnosis and Morphology of Breast Diseases*, (W. B. Saunders Company, Pa, 1988).

6. M. Cutler, "Transillumination as an aid in the diagnosis of breast lesions," Surg. Gynecol. Obstet., **48**, 721, 1929.

7. F. Liu, Ph. D. Thesis, The City University of New York, 1993.

8. L. Wang, P. P. Ho, C. Liu, G. Zhang, and R. R. Alfano, "Ballistic 2–D imaging through scattering walls using an ultrafast optical Kerr gate," Science **253**, pp. 769–771, 1991.

9. D. Huang, J. Wang, C. P. Lin, C. A. Puliafito, and J. G. Fujimoto, "Micron-resolution ranging of cornea anterior chamber by optical reflectometry," Las. Surg. Med. **11**, 419–425, 1991.

10. D. Huang, E. A. Swanson, C. P. Lin, J. S. Schuman, W. G. Stinson, W. Chang, M. R. Hee, T. Flotte, K. Gregory, C. A. Puliafito, and J. G. Fujimoto, "Optical coherence tomography," Science **254**, pp. 1178–1181, 1991.

11. See SPIE series on Medical Optical Tomography: Functional Imaging and Monitoring, edited by G. J. Muller (SPIE, Washington, DC, 1993) Vol. IS11.

12. K. M. Yoo and R. R. Alfano, "Time-resolved coherent and incoherent components of forward light scattering in random media," Opt. Lett. **15**, pp. 320–322 1990.

13. F. Liu, K. M. Yoo, and R. R. Alfano, "Transmitted photon intensity through biological tissues within various time windows," Optics Lett., **19**, pp. 740–742, 1994.

14. A. E. Profio, "Light transport in tissue," Appl. Opt., **28**, pp. 2210–2215, 1989.

15. N. Garcia, A. Z. Genack, and A. A. Lisyansky, "Measurement of the transport mean free path of diffusing photons," Phys. Rev. B, **46**, pp. 14475–14479, 1992.

16. K. M. Yoo, F. Liu, and R. R. Alfano, "When does the diffusion approximation fail to describe photon transport in random media ?," Phys. Rev. Lett. **64**, pp. 2647–2650.

17. K. M. Yoo, K. Arya, G. C. Tang, J. L. Birman, and R. R. Alfano, "Coherent backscattering of a picosecond pulse from a disordered medium: Analysis of pulse shape in the time domain," Phys. Rev. A, **39**, pp. 3728–3731, 1989.

18. D. Huang, E. A. Swanson, C. P. Lin, J. S. Schuman, W. G. Stinson, W. Chang, M. R. Hee, T. Flotte, K. Gregory, C. A. Puliafito, and J. G. Fujimoto, "Optical coherence tomography," Science **254**, pp. 1178–1181, 1991.

19. F. Liu, K. M. Yoo, and R. R. Alfano, "Speed of the coherent component of femtosecond laser pulses propagating through random scattering media," Opt. Lett. 15, pp. 351–353, 1991.

Chapter 2

Light transport theory

2.1 Introduction

The propagation of light in random scattering media can be described by the transport theory(radiative transfer theory)[1-3]. This theory deals with the transport of energy through a medium containing scattering particles. The derivation of the theory is heuristic and it lacks the mathematical rigor of analytical theories such as Maxwell or wave equations. The basic equation used is the transfer equation which is equivalent to Boltzman's equation used in kinetic theory of gases and in neutron transport theory[4-6]. A general solution to this equation has not been obtained yet. An approximation to this equation for light propagation in highly scattering media is the diffusion equation[7-9]. The diffusion approximation has found wide uses in the optical community in trying to describe the propagation of a laser pulse in scattering media such as tissues[10].

In this chapter the equation of transfer will be derived heuristically. The diffusion equation will be derived from the transfer equation by assuming the case of light propagation through highly scattering media.

2.2 Overview of Mie theory

Mie theory has often been used to calculate the scattering cross section and the anisotropy factor of a spherical scattering particle. For a sphere of radius a and relative refractive index m in another medium (m=refractive index of sphere/refractive index of background medium), the scattering cross-section is given by Mie theory as[8-9]:

$$\sigma_s = \frac{2\pi a^2}{(ka)^2} \sum_{n=1}^{n=\infty} (2n+1)\left(|a_n|^2 + |b_n|^2\right), \tag{2.1}$$

where $k = \frac{2\pi}{\lambda}$ is the wavenumber,

$$a_n = \frac{\psi_n(\alpha)\psi_n'(\beta) - m\psi_n(\beta)\psi_n'(\alpha)}{\zeta_n(\alpha)\psi_n'(\beta) - m\psi_n(\beta)\zeta_n'(\alpha)}, \tag{2.2}$$

$$b_n = \frac{m\psi_n(\alpha)\psi_n'(\beta) - \psi_n(\beta)\psi_n'(\alpha)}{m\zeta_n(\alpha)\psi_n'(\beta) - \psi_n(\beta)\zeta_n'(\alpha)}, \tag{2.3}$$

$\alpha = ka$ *and* $\beta = kma$, and where $\psi_n(x) = \sqrt{\pi x/2} J_{n+\frac{1}{2}}(x)$ *and* $\zeta_n(x) = \sqrt{\pi x/2}\left[J_{n+\frac{1}{2}}(x) + i(-1)^n J_{-n-1/2}(x)\right]$ are the Ricatti-Bessel functions.

The normalized scattering cross section Q_s is given by:

$$Q_s = \frac{\sigma_s}{\pi a^2}. \tag{2.4}$$

The anisotropy factor is given by:

$$\begin{aligned} g\frac{\sigma_s}{\pi a^2} = {} & \frac{4}{(ka)^2} \sum_{n=1}^{n=\infty} \frac{n(n+2)}{n+1} Re\left(a_n a_{n+1}^* + b_n b_{n+1}^*\right) \\ & + \frac{1}{(ka)^2} \sum_{n=1}^{n=\infty} \frac{2n+1}{n(n+1)} Re\left(a_n b_n^*\right), \end{aligned} \tag{2.5}$$

where Re stands for the real part and * stands for the complex conjugate.

The normalized transport cross section is related to the normalized scattering cross section as: $Q_t = Q_s(1-g)$. In terms of the normalized transport cross section, the transport mean free path is given by:

$$l_t = \frac{1}{\pi a^2 \rho} \frac{1}{Q_t}. \tag{2.6}$$

where ρ is the number of particles per unit volume.

When the index of refraction of the background medium is close to that of the scatterer (m=1), one sees that, from eq. 2.1, $\sigma_s - > 0$ as there is no scattering independent of the size of the scatterer.

Once the diameter and the index of refraction of the sphere are known, one can calculate the scattering and the transport cross sections at different wavelengths. The normalized scattering cross section $Q_s = \frac{\sigma_s}{\pi a^2}$ and the anisotropy factor g for various sizes of polystyrene latex microspheres scattering suspensions are plotted in Figs. 2–1 and 2–2, respectively. The index of the scatterers is taken as 1.59 and the host medium is water(index=1.33). The volume concentration of the scatterers is 1%. The scattering increases and then oscillates at around 2 for large particles. The anisotropy factor against the diameter of the particle up to $20\mu m$ is shown in Fig. 2–2a. The diameter axis in Fig. 2–2a is expanded to $6\mu m$ in Fig. 2–2b. The anisotropy factor increases rapidly to about 0.92 and then oscillates for particles of diameters around $4\mu m$ and stabilizes at around g=0.92 (Fig.2–2a and b).

Fig. 2–3 shows the wavelength dependence of the anisotropy factor for polystyrene spheres of $0.46\mu m$ diameter. The anisotropy factor decreases for long wavelengths (i.e. small particles). The anisotropy decreases from 0.92 at λ =300nm to 0.72 at λ =850nm.

Fig. 2.4 shows the dependence of the transport mean free path and the scattering length on the size of the particle for 1% volume concentration of the scattering particles. For small particles, l_t=l_s. This means that for small particles, it may be difficult to see the diffuse signal in the transmission geometry at moderate source to detector separations (about $10l_t$) because the ballistic signal might be too intense. For large particles, l_t is

much larger than l_s.

2.3 Transfer equation

Consider a specific intensity $I(\vec{r}, \hat{s}, t)$, which is the number of photons per unit area per unit time per unit solid angle, at r at time t, travelling in the direction $\hat{s}$, and incident on a cylindrical elementary volume with unit cross section and length ds and particle density ρ (Fig. 2–5). The volume ds contains ρds particles at time t. At time t, each particle absorbs the power $\sigma_a I(\vec{r}, \hat{s}, t)$ and scatters $\sigma_s I(\vec{r}, \hat{s}, t)$, where σ_a *and* σ_s are the absorption and the scattering cross-sections, respectively. The decrease in specific intensity, with the total cross section $\sigma_t = \sigma_a + \sigma_s$, is:

$$dI(\vec{r}, \hat{s}, t) = -ds\rho(\sigma_a + \sigma_s)I(\vec{r}, \hat{s}, t) = -ds\rho\sigma_t I(\vec{r}, \hat{s}, t). \tag{2.7}$$

The contribution to the specific intensity for one particle is obtained by the specific intensity incident on the volume from other directions $\hat{s}'$ that is scattered into $\hat{s}$ and is given by:

$$\frac{\sigma_t}{4\pi} \int_{4\pi} p(\hat{s}, \hat{s}') I(\vec{r}, \hat{s}', t) d\omega'. \tag{2.8}$$

The phase function $p(\hat{s}, \hat{s}')$ represents the probability that a photon travelling in direction $\hat{s}'$ will be scattered into direction $\hat{s}$ and is related to the scattering cross section as: $\sigma_s = \frac{\sigma_t}{4\pi} \int_{4\pi} p(\hat{s}, \hat{s}') d\omega$.

The "equation of transfer" for ρds particles and a source of photons S, assuming that it takes at least t seconds for a photon travelling the distance ds at a speed v (i.e. ds=vdt)

to exit the volume is given as:

$$\frac{dI(\vec{r},\hat{s},t)}{vdt}+\frac{dI(\vec{r},\hat{s},t)}{ds}=-\rho\sigma_t I(\vec{r},\hat{s},t)+\frac{\rho\sigma_t}{4\pi}\int_{4\pi}p(\hat{s},\hat{s}')I(\vec{r},\hat{s}',t)d\omega'+S(\vec{r},\hat{s},t). \quad (2.9)$$

Consider the photon number density(number of photons per unit volume) $n(\vec{r},t)$ at position $\vec{r}=(x,y,z)$ at time t. The amount of energy leaving a small area da in a direction normal to it within a solid angle $d\omega$ in time dt is $I(\vec{r},\hat{s},t)dad\omega dt$. This energy occupies a volume vdadt. The energy density $dn(\vec{r},t)$ in that small volume element is

$$dn(\vec{r},t)=\frac{I(\vec{r},\hat{s},t)dad\omega dt}{vdadt}=\frac{I(\vec{r},\hat{s},t)d\omega}{v}. \quad (2.10)$$

Integrating eq. 2.10 over all directions, the photon density becomes:

$$n(\vec{r},t)=\frac{1}{v}\int_{4\pi}I(\vec{r},\hat{s},t)d\omega. \quad (2.11)$$

The photon number density is due to the radiation in all directions. The photon flux represents the amount and the direction of the net flow of power and is given by:

$$\vec{J}(\vec{r},t)=\hat{s}_j J(\vec{r},t)=\int_{4\pi}I(\vec{r},\hat{s},t)\hat{s}d\omega. \quad (2.12)$$

2.4 Diffusion equation and Boundary conditions

2.4.1 Diffusion equation

The specific intensity is composed of two parts: ballistic/snake, $I_b(\vec{r},\hat{s},t)$, which travels a path almost straight from the source to the detector and diffuse, $I_d(\vec{r},\hat{s},t)$, which

travels all over the scattering medium($I(\vec{r},\hat{s},t) = I_b(\vec{r},\hat{s},t) + I_d(\vec{r},\hat{s},t)$). Replacing this expression for the total intensity breaks eq. 2.9 in two parts. The ballistic/snake component satisfies the equation:

$$\frac{dI_b(\vec{r},\hat{s},t)}{vdt} + \frac{dI_b(\vec{r},\hat{s},t)}{ds} = -\rho\sigma_t I_b(\vec{r},\hat{s},t) + S(\vec{r},\hat{s},t). \tag{2.13}$$

The diffuse part satisfies the equation:

$$\begin{aligned} &\frac{dI_d(\vec{r},\hat{s},t)}{vdt} + \frac{dI_d(\vec{r},\hat{s},t)}{ds} = -\rho\sigma_t I_d(\vec{r},\hat{s},t) + \\ &\frac{\rho\sigma_t}{4\pi}\int_{4\pi} p(\hat{s},\hat{s}')\, I_d(\vec{r},\hat{s}',t)d\omega' + S_b(\vec{r},\hat{s},t) \\ &where\ S_b(\vec{r},\hat{s},t) = \frac{\rho\sigma_t}{4\pi}\int_{4\pi} p(\hat{s},\hat{s}')\, I_b(\vec{r},\hat{s}',t)d\omega'. \end{aligned} \tag{2.14}$$

Remark that $\frac{dI_d(\vec{r},\hat{s},t)}{ds} = \hat{s}\cdot\nabla I_d(\vec{r},\hat{s},t) = \hat{s}\cdot\hat{a}_r\frac{dI_d(\vec{r},\hat{s},t)}{dr}$ where in cartesian coordinates $\hat{a}_r\frac{d}{dr} = \hat{a}_x\frac{\partial}{\partial x} + \hat{a}_y\frac{\partial}{\partial y} + \hat{a}_z\frac{\partial}{\partial z}$ and $\hat{s}\cdot\hat{a}_r = cos\theta = \mu$.

After replacing the above expression for $\frac{dI_d(\vec{r},\hat{s},t)}{ds}$, eq. 2.14 becomes:

$$\begin{aligned} &\frac{dI_d(\vec{r},\mu,t)}{vdt} + \mu\frac{dI_d(\vec{r},\mu,t)}{dr} = -\rho\sigma_t I_d(\vec{r},\mu,t) + \\ &\frac{\rho\sigma_t}{4\pi}\int_{-1}^{1} p(\mu,o;\mu',o')\, I_d(\vec{r},\mu',t)d\phi' d\mu' + S_b(\vec{r},\mu,t) \end{aligned} \tag{2.15}$$

where the substitution $d\omega' = sin\theta' d\theta' d\phi' = -d\mu' d\phi'$ is made. Integrating eq. 2.15 over ϕ yields:

$$\begin{aligned} &\frac{dI_d(\vec{r},\mu,t)}{vdt} + \mu\frac{dI_d(\vec{r},\mu,t)}{dr} = -\rho\sigma_t I_d(\vec{r},\mu,t) + \\ &\frac{\rho\sigma_t}{2}\int_{-1}^{1} d\mu' \left[\frac{1}{2\pi}\int_0^{2\pi} do\,\frac{1}{2\pi}\int_0^{2\pi} d\phi' p(\mu,o;\mu',o')\right] I_d(\vec{r},\mu',t) + S_b(\vec{r},\mu,t). \end{aligned} \tag{2.16}$$

The source of photons is assumed to have no ϕ dependence.

A standard way to solve this equation is to expand the different terms in spherical harmonics. The diffuse intensity can be expanded into a series of Legendre polynomials as:

$$I_d(\vec{r},\mu,t) = \sum_{l=0}^{l=\infty} I_l(\vec{r},t)P_l(\mu) \ , \tag{2.17}$$

where the first terms of the Legendre polynomials are: $P_0(\mu) = 1$, $P_1(\mu) = \mu$, and $P_2(\mu) = \frac{1}{2}(3\mu^2 - 1)$.

After multiplying eq. 2.17 by $P_n(\mu)$ and integrating over μ from -1 to 1, one finds:

$$I_l(\vec{r},t) = \frac{2l+1}{2}\int_{-1}^{1} I_d(\vec{r},\mu,t)P_l(\mu)d\mu, \tag{2.18}$$

where the orthogonality relation for the Legendre polynomials:

$$\int_{-1}^{1} P_l(\mu)P_n(\mu)d\mu = \begin{cases} 0 \ if \ l \neq n \\ \dfrac{2}{2l+1} \ if \ l = n \end{cases} \tag{2.19}$$

has been used.

Substituting l by 0 in eq. 2.18, one has:

$I_0(\vec{r},t) = \frac{1}{2}\int_{-1}^{1} I_d(\vec{r},\mu,t)d\mu$ that is related to the photon density (eq. 2.11) by:

$$n(\vec{r},t) = \frac{4\pi}{v} I_0(\vec{r},t), \qquad l = 0. \tag{2.20}$$

Substituting l by 1 in eq. 2.18 gives:

$$I_1(\vec{r},t) = \frac{3}{2}\int_{-1}^{1} \mu I_d(\vec{r},\mu,t)d\mu \tag{2.21}$$

which is related to the flux (eq. 2.12) by:

$$J(\vec{r},t) = \frac{4\pi}{3} I_1(\vec{r},t) \qquad l = 1. \tag{2.22}$$

The elementary diffusion equation is obtained by taking P_l=0 for $l > 1$[7,8,11]. That is the angular distribution is represented by only the first two terms in the spherical harmonics expansion. The expression for eq. 2.17 becomes:

$$I_d(\vec{r},\mu,t) \approx I_0(\vec{r},t) + \mu I_1(\vec{r},t) \tag{2.23}$$

which gives the diffuse intensity as:

$$I_d(\vec{r},\mu,t) \approx \frac{cn(\vec{r},t)}{4\pi} + \frac{3\mu J(\vec{r},t)}{4\pi} \tag{2.24}$$

where $n(\vec{r},t)$ is the photon number density(# of photons per unit volume) and $J(\vec{r},t)$ is the photon flux(# of photons per unit area per unit time).

The first term is considerably larger than the second term of eq. 2.24.

The derivation of the diffusion equation is proceeded by expanding the different terms of eq. 2.16 by their spherical harmonics.

If the scattering is symmetric about the direction of the incident radiation, the phase function $p(\mu,\phi;\mu',\phi')$ is expanded in spherical harmonics as:

$$p(\mu,\phi;\mu',\phi') = \sum_{l=0}^{\infty} W_l P_l(cos\gamma) \tag{2.25}$$

where $W_o = \frac{\sigma_s}{\sigma_t}$ *and* $W_1 = 3gW_0$, γ is the angle between (μ,ϕ) *and* (μ',ϕ') and

$$P_l(cos\gamma) = P_l(\mu)P_l(\mu') + 2\sum_{m=1}^{l} \frac{(l-m)!}{(l+m)!} P_l^m(\mu)P_l^m(\mu')cos(\phi-\phi'). \tag{2.26}$$

Substituting eq. 2.26 into the phase function expansion eq. 2.25, and replacing eq. 2.25 into eq. 2.16 gives:

$$\frac{dI_d(\vec{r},\mu,t)}{vdt} + \mu\frac{dI_d(\vec{r},\mu,t)}{dr} = -\rho\sigma_t I_d(\vec{r},\mu,t) + \frac{\rho\sigma_t}{2}\sum_{l=0}^{\infty} W_l P_l(\mu)\int_{-1}^{1} d\mu' P_l(\mu') I_d(\vec{r},\mu',t) + S_b(\vec{r},\mu,t). \tag{2.27}$$

Integrating eq. 2.27 with respect to μ (which is equivalent to multiplying by $P_0(\mu)$ and then integrating with respect to μ; this concept will be applied for the second term on the right hand side of eq. 2.27 so that the orthogonality principle can be used) and substituting the expressions for the photon density and flux give:

$$\frac{d}{vdt}\frac{vn(\vec{r},t)}{2\pi} + \frac{d}{dr}\frac{J(\vec{r},t)}{2\pi} = -\rho\sigma_t\frac{vn(\vec{r},t)}{2\pi} + \rho\sigma_t W_0\frac{vn(\vec{r},t)}{2\pi} + S_0(\vec{r},t), \tag{2.28}$$

where $S_0(\vec{r},t) = \int_{-1}^{1} S_b(\vec{r},\mu,t)d\mu$.

After multiplication by 2π, eq. 2.28 yields:

$$\frac{d}{dt}n(\vec{r},t) + \frac{d}{dr}J(\vec{r},t) = -\rho\sigma_a vn(\vec{r},t) + 2\pi S_0(\vec{r},t). \tag{2.29}$$

Multiplying eq. 2.27 by $P_1(\mu)$ and integrating with respect to μ while applying the orthogonality principle and replacing the expression for the flux gives:

$$\frac{1}{2\pi v}\frac{dJ(\vec{r},t)}{dt} + \frac{d}{dr}\int_{-1}^{1}\mu P_1(\mu) I_d(\vec{r},\mu,t)d\mu = -\rho\sigma_t\frac{J(\vec{r},t)}{2\pi} + \frac{\rho\sigma_t}{3}W_1\frac{J(\vec{r},t)}{2\pi}. \tag{2.30}$$

The integral of the source term is zero for an isotropic source. The expression $I_d(\vec{r},\mu,t) \approx I_0(\vec{r},t)P_0(\mu) + I_1(\vec{r},t)P_1(\mu)$ which is the approximation of the Legendre polynomials expansion given earlier is replaced in the second term on the left hand side of eq. 2.30. Neglecting the time derivative term of the flux in eq. 2.30, we have, after applying the relation

$$\int_{-1}^{1} \mu P_n(\mu)P_l(\mu)d\mu = \begin{cases} 0 \; if \; l \neq n+1 \\ \dfrac{n+1}{2n+1}\dfrac{2}{2(n+1)+1} \; if \; l = n+1. \end{cases} \tag{2.31}$$

$$\frac{v}{3}\frac{d}{dr}n(\vec{r},t) = -\rho(\sigma_s(1-g)+\sigma_a)J(\vec{r},t). \tag{2.32}$$

In vector form, eq. 2.32 is written as:

$$\frac{v}{3}\nabla n(\vec{r},t) = -\rho(\sigma_s(1-g)+\sigma_a)\vec{J}(\vec{r},t). \tag{2.33}$$

This equation is Fick's law of diffusion and is often written as:

$$\vec{J}(\vec{r},t) = -D\nabla n(\vec{r},t) \tag{2.34}$$

where $D = \frac{v}{3\rho(\sigma_s(1-g)+\sigma_a)} = \frac{vl_t}{3}$ is the diffusion coefficient and is independent of time and space and the absorption cross-section is negligible with respect to the scattering cross-section. Taking the divergence of eq. 2.34 and replacing it in eq. 2.29 gives:

$$\frac{\partial n(\vec{r},t)}{\partial t} = D\nabla^2 n(\vec{r},t) - \frac{v}{l_a}n(\vec{r},t) + 2\pi S_0(\vec{r},t). \tag{2.35}$$

At time 0 for an impulse source at $\vec{r} = \vec{r^j}$, eq. 2.35 is often written as[12–14]:

$$\frac{\partial n(\vec{r},t)}{\partial t} = D\nabla^2 n(\vec{r},t) - \frac{v}{l_a} n(\vec{r},t) + \delta\left(\vec{r} - \vec{r^j}\right)\delta(t). \tag{2.36}$$

This approximation is called the diffusion equation and is valid for source-detector separated by at least $7l_t$[15]. The term on the left hand side is the rate of photon generation. The first term on the right hand side is the diffusion term; the second and third terms on the right hand side are the absorption and the source terms, respectively.

2.4.2 Boundary Conditions

Consider a scattering medium of boundaries as shown in fig. 2–6 where $\hat{p}$ is a unit vector normal to the boundary and directed toward the scattering medium and $\hat{s}$ is a unit vector in the direction of observation.

The exact boundary condition is that at the surface there should be no diffuse intensity coming from outside the medium to inside the medium. Because of the approximative nature of the diffusion equation and of the specific intensity, this boundary condition can not be satisfied exactly. One must have recourse to approximate boundary conditions one of which is that the total flux directed inward must be zero i.e.:

$$\int_{2\pi} I_d(\vec{r}_s,\hat{s},t)(\hat{p}\cdot\hat{s})d\omega. \tag{2.37}$$

where $\vec{r}_s$ stands for a position at the surface.

Replacing 2.24 in 2.37 and replacing $\mu = cos\theta = \hat{s}\cdot\hat{s}_j$, one obtains:

$$\int_{2\pi} \left(\frac{cn(\vec{r},t)}{4\pi} + \frac{3\vec{J}(\vec{r},t)\cdot\hat{s}}{4\pi} \right)(\hat{p}\cdot\hat{s})d\omega = 0 \tag{2.38}$$

where $\vec{J}(\vec{r},t) = \hat{s}_J J(\vec{r},t)$.

Substituting the flux by a sum of a normal(J_{dn}) and tangential components(J_{dt}) where $\vec{J} = J_{dn}\hat{p} + J_{dt}\hat{t}$, and replacing in eq. 2.38 give:

$$\int_{2\pi} \frac{cn}{4\pi}\hat{p}\cdot\hat{s}d\omega + \frac{3}{4\pi}\int_{2\pi} J_{dn}\hat{p}\cdot\hat{s}(\hat{p}\cdot\hat{s})d\omega + \frac{3}{4\pi}\int_{2\pi} J_{dt}\hat{t}\cdot\hat{s}(\hat{p}\cdot\hat{s})d\omega = 0$$
$$where\ \hat{p}\cdot\hat{s} = cos\theta \tag{2.39}$$
$$\hat{t}\cdot\hat{s} = sin\theta cos\phi$$

Performing these integrations gives the boundary condition as:

$$J_{dn}(\vec{r}_s) = -\frac{n(\vec{r}_s)c}{2} \tag{2.40}$$

Substituting $J_{dn}(\vec{r}_s,\hat{p},t) = \hat{p}\cdot(-D\nabla n(\vec{r},t))|_{\vec{r}=\vec{r}_s} = -D\frac{\partial n(\vec{r}_s,t)}{\partial p}$ gives the boundary condition as:

$$n(\vec{r}_s,t) - \frac{2l_t}{3}\frac{\partial n(\vec{r}_s,t)}{\partial p} = 0. \tag{2.41}$$

This boundary condition(eq. 2.41) means that the photon density should approximate to zero at a distance equal to $2l_t/3 = 0.667l_t$ beyond a plane separating a diffusive medium from vacuum. This is, however, an approximation. According to the more exact transport theory, the extrapolation distance has been shown to be $0.7104l_t$.

In this thesis, the extrapolation distance of $0.7104l_t$ is used.

2.5 Conclusion

The diffusion equation approximation to the transfer equation for highly scattering media has been derived. The boundary condition at the surface has showed that the photon number density vanishes at a linear extrapolation distance beyond the medium boundary. In the succeeding chapters, the diffusion will be solved in time or frequency domains according to the geometry of the particular problem. Better approximation might be needed in the future to fit more accurately the experimental data.

2.6 References

1. S. Chandrasekhar, *Radiative transfer*, (Oxford University Press, London, 1950).

2. J. J. Duderstadt and L. J. Hamilton, *Nuclear reactor analysis*, (Wiley, New York, 1976).

3. K. M. Case, P. F. Zweifel, *Linear transport theory*, (Addison-Wesley, Massachusetts, 1969).

4. K. M. Case, F. D. Hoffman, and G. Placzek, *Introduction to the theory of neutron diffusion*, (Los Alamos Scientific Lab., New Mexico, 1953).

5. B. Davison, *Neutron transport theory*, (Oxford University Press, London, 1958).

6. M. Lax, *Symmetry principles in solid state and molecular physics*, (Wiley, New York, 1974).

7. G. I. Bell and S. Glasstone, *Nuclear reactor theory*, (D. Van Nostrand Company, New Jersey, 1970).

8. A. Ishimaru, *Wave propagation and scattering in random media*, (Academic Press, New York, 1978).

9. H. C. van de Hulst, *Light Scattering by Small Particles*, (Dover, New York, 1981).

10. See SPIE series on Medical Optical Tomography: Functional Imaging and Monitoring, edited by G. J. Muller (SPIE, Washington, DC, 1993) Vol. IS11.

11. F. Liu, K. M. Yoo, and R. R. Alfano, "Should the photon flux or the photon density be used to describe the temporal profiles of scattered ultrashort laser pulses in random media?," Opt. Lett. **18**, pp. 432–434, 1993.

12. K. Furutsu, "Diffusion equation derived from the space-time transport equation," J. Opt. Soc. of Am. **70**, 360–366, 1980.

13. K. Furutsu, "Diffusion equation derived from the space-time transport equation in anisotropic random media," J. Math. Phys. **21**, 765–777, 1980.

14. M. S. Patterson, B. Chance, and B. C. Wilson, "Time-resolved reflectance and transmittance for the noninvasive measurement of tissue optical properties," Appl. Opt. **28**, pp. 2331–2336, 1989.

15. K. M. Yoo, F. Liu, and R. R. Alfano, "When does the diffusion approximation fail to describe photon transport in random media ?," Phys. Rev. Lett. **64**, pp. 2647–2650.

2.7 Figures

Figure 2.1 Plot of the normalized scattering cross-section vs. diameters of polystyrene latex microspheres at the laser wavelength of 625nm. The volume concentration is 1%. The index contrast is the ratio of the index of refraction of the intralipid scatterers to the index of the host medium which is water in this case.

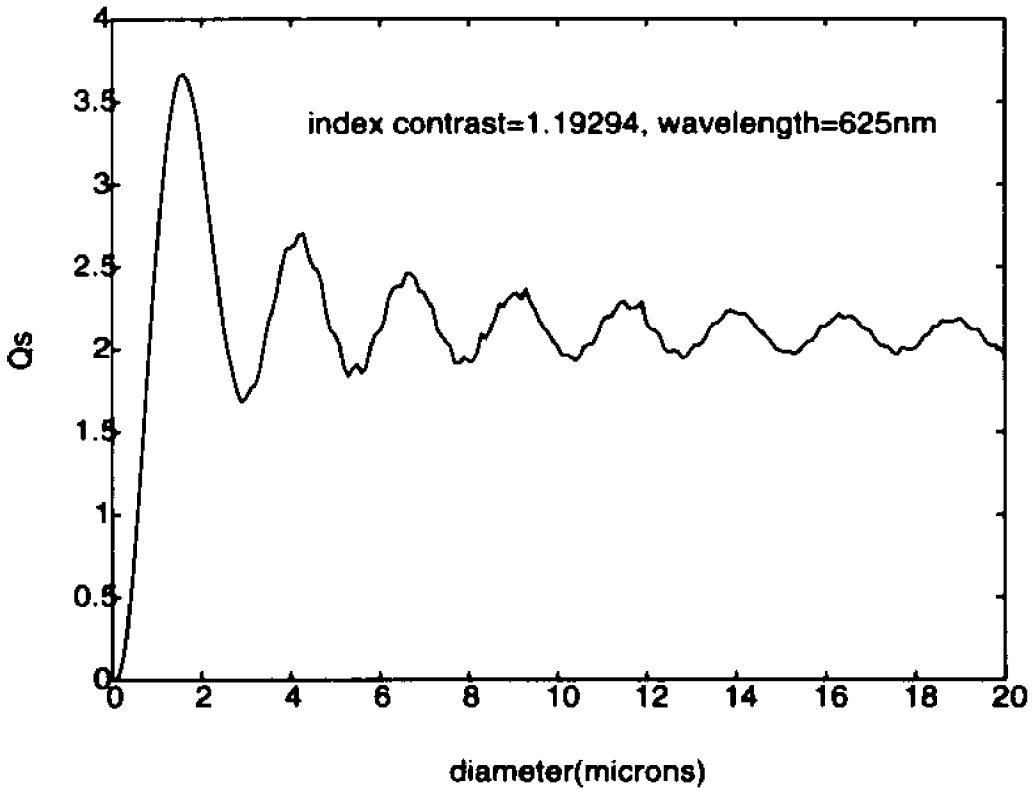

Figure 2.2 Plot of the anisotropy factor vs diameters up to a) 20 μm and up to b) 6μm of polystyrene latex microspheres scattering suspensions at the laser wavelength of 625nm. The index contrast is the ratio of the index of refraction of the polystyrene latex microspheres to the index of the host medium which is water in this case.

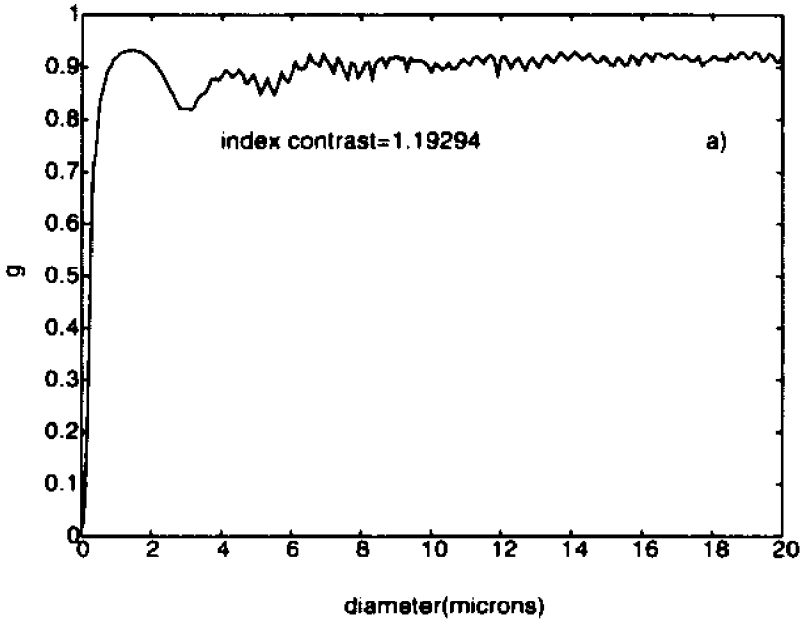

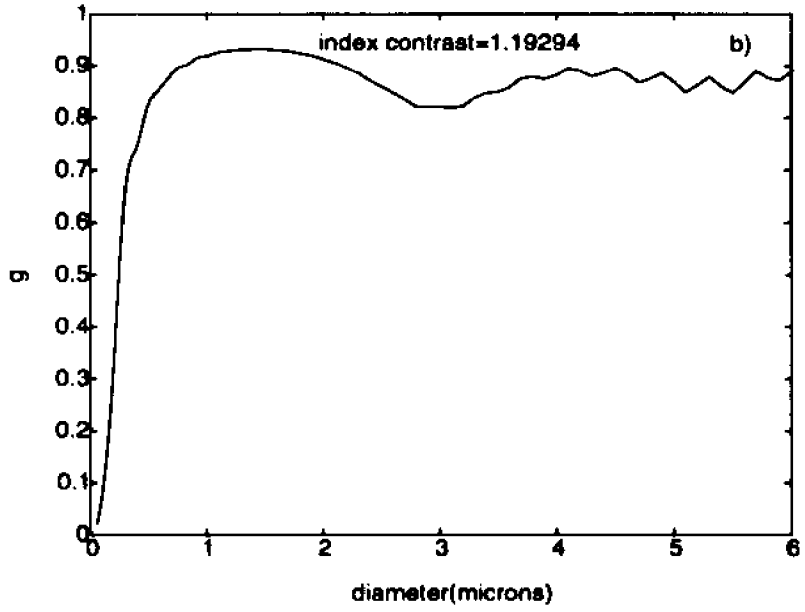

Figure 2.3 Plot of the anisotropy factor vs. wavelengths of radiation for polystyrene latex microspheres of diameter 0.46microns. The index contrast is the ratio of the index of refraction of the scatterers to the index of water .

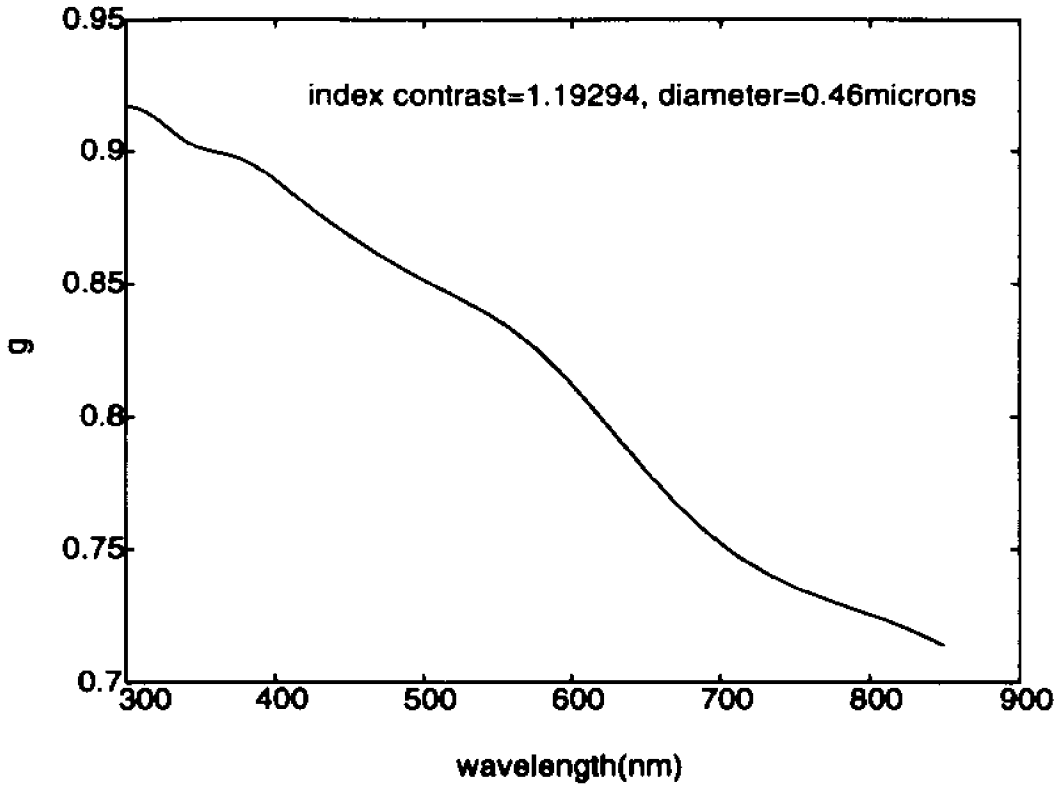

Figure 2.4 The transport mean free path and the scattering length plotted vs the particle diameter for an index contrast of 1.19294 at the wavelength of 625nm. The volume concentration is 1%.

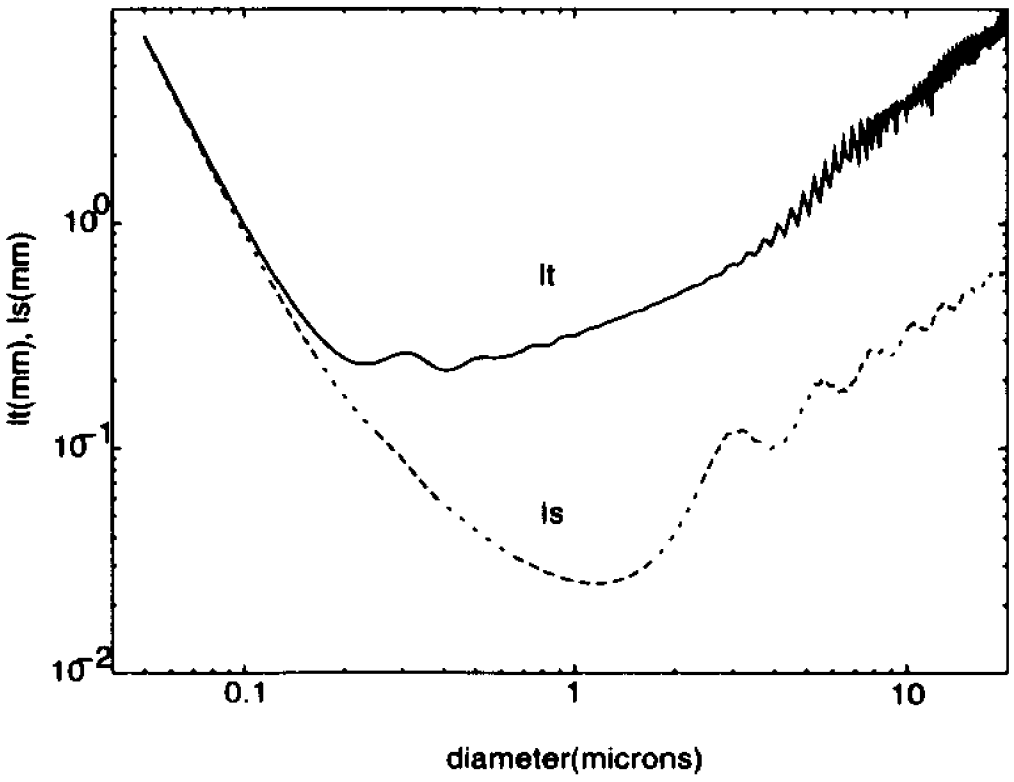

Figure 2.5 An incident beam incident on a volume of scattering medium is scattered from the direction $\hat{s}'$ into the direction $\hat{s}$.

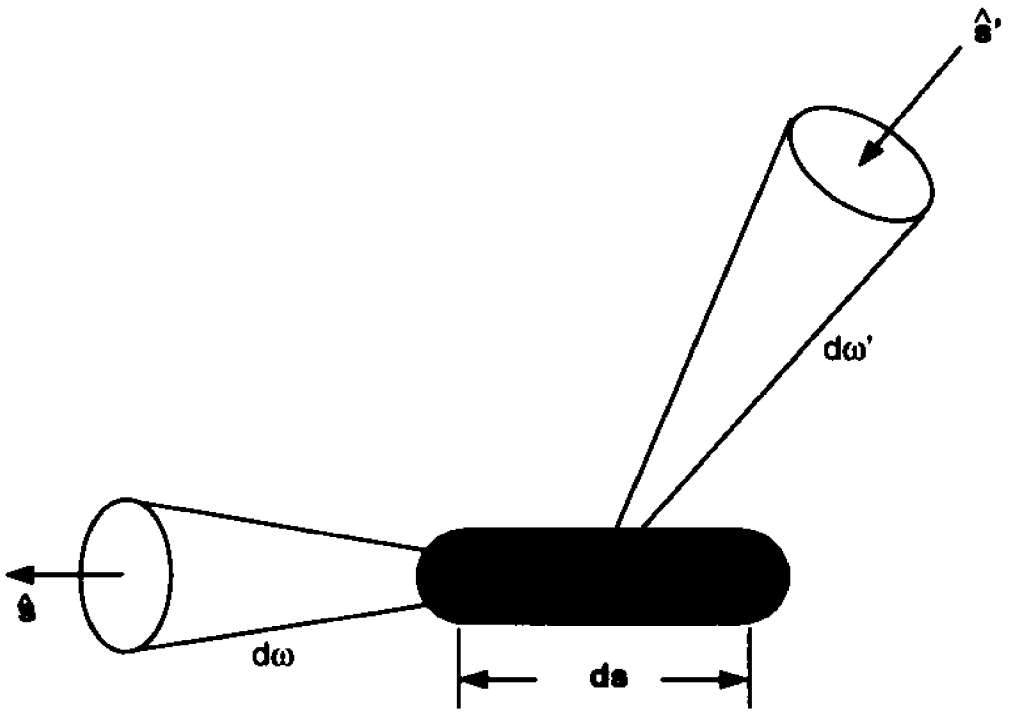

Figure 2.6 A diffusive medium is separated from a vacuum medium.

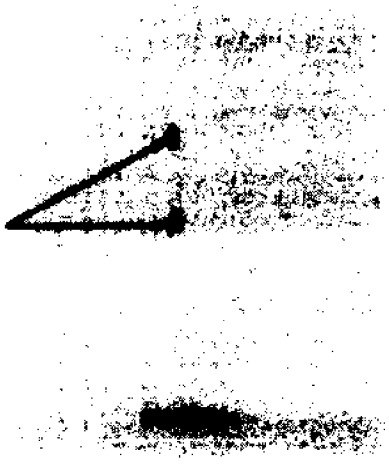

Chapter 3

CW imaging of an object hidden behind a highly scattering wall

3.1 Introduction

Imaging an object hidden behind randomly scattering medium has received increased attention in the optical community in recent years. For highly scattering medium, the ballistic light which projects a shadow of the object on the detector is extremely low and can be many orders of magnitude below the diffuse light . The edges of the object become extremely blurred by the diffuse noise. It becomes almost impossible to obtain an image with decent contrast. Many time-resolved methods, such as streak camera[1-3], Kerr-gate[4] and ultrafast holography[5] have been introduced to selectively extract the ballistic light image information from the diffuse noise information. The time-resolved methods usually require complicated and expensive instrumentations. A simpler CW method has been presented by Alfano et al.[6] who have used absorption to improve the contrast in imaging through a scattering wall. The image became clearer and clearer as absorption was increased by adding more absorbing dyes. The underlying principle is that the diffuse light travels an average distance of $\frac{L^2}{2l_t}$ which is much longer than the distance L that the ballistic light travels. The more distance the light travels, the more probable it is for the light to be absorbed. Therefore, the diffuse light will be absorbed much more than the ballistic light. This technique can be exploited further by naturally varying the absorption in the medium. A natural way to change the absorption in the medium is to vary the wavelength of radiation.

In this chapter, we introduce a novel technique that uses a spatial filter and several laser wavelengths in the NIR region that can reduce the diffuse light below that of the ballistic/snake component. This technique is based on the Fourier transform properties of an optical lens and the absorption of the host medium in the NIR wavelengths[7]. The diffraction pattern of an object illuminated by a plane wave is formed at the focal plane of the transform lens[8–10]. That pattern consists of different spatial frequencies. The central spot in the diffraction pattern is the D.C. term corresponding to zero spatial frequency (ballistic light). As the spots in the Fourier plane get farther from the central axis, their associated spatial frequencies representing the multiply scattered light increase. A suitable mask may be used to remove most of these high Fourier frequencies and image preferably the ballistic component on the image plane. Some diffuse light exit the medium collinearly with the ballistic/snake signal and can be removed by absorption of the medium. The absorption of the medium varies with the wavelength of radiation. The longer the wavelength is in the therapeutic window (from 700nm to 1300nm), the more absorption water has.

This method can allow the separation of large objects whose spatial frequencies are low from small objects whose spatial frequencies are high. With this capacity, objects such as tumors might be detected and removed at a very early stage as opposed to current technologies such as X-Ray which can detect objects of several mm sizes.

3.2 Theory

The attenuation of the light components upon exiting a slab of scattering medium of thickness L are as follows. The ballistic component is given by:

$$I_b = I_0 e^{-(\frac{1}{l_s}+\frac{1}{l_a})L}, \tag{3.1}$$

where I_0 is the input energy; l_s, the scattering length, and l_a, the absorption length. The snake component for media whose transport mean is much less than the absorption length ($l_t << l_a$) is given by[11]:

$$I_s = I_0 A(\Delta t) e^{-b(\Delta t)L/l_t}. \tag{3.2}$$

The diffuse component of the transmitted light is obtained by solving the diffusion equation:

$$\frac{\partial n(\vec{r},t)}{\partial t} = D\nabla^2 n(\vec{r},t) - \frac{v}{l_a} n(\vec{r},t) + \delta\left(\vec{r} - \vec{r'}\right)\delta(t), \tag{3.3}$$

where $n(\vec{r},t)$ is the photon number density; $D = \frac{vl_t}{3}$, is the diffusion constant; v is the speed of light in the medium, l_t, is the transport mean free path; l_a is the absorption length; $\delta\left(\vec{r} - \vec{r'}\right)\delta(t)$ is the photon source effectively randomized at r'=(0,0,z') at time t=0.

For a slab of thickness L located between $z=z_0$ ($z_0=0.7104l_t$ is the extrapolation length) and $z=L+z_0$, with the condition that the photon density vanishes at z=0 and $z=L+2z_0$, the photon number density is given by[12]:

$$n(\vec{r},t) = \frac{e^{-\frac{R^2}{4Dt}}}{(4\pi Dt)^{3/2}} \sum_{m=-\infty}^{m=+\infty} \left\{ e^{-(2md+z'-z)^2/4Dt} - e^{-(2md-z'-z)^2/4Dt} \right\} e^{-vt/l_a}, \tag{3.4}$$

where $R = \sqrt{x^2+y^2}$, and $d=L+2z_0$. The photon density can be written using Poisson sum formula as:

$$n(\vec{r},t) = \frac{e^{-\frac{R^2}{4Dt}}}{4\pi Dtd} \sum_{m=-\infty}^{m=\infty} \sin\frac{m\pi z'}{d} \sin\frac{m\pi z}{d} e^{-Dt(m\pi/d)^2} e^{-vt/l_a}. \tag{3.5}$$

The photon flux derived from Fick's law of diffusion, $j_z = -D\frac{\partial n}{\partial z}$, through the slab in the z-direction with z'=z_0 and z=L+z_0 is given by:

$$j_z = \frac{De^{-\frac{R^2}{4Dt}}}{(4\pi Dt)d} \sum_{m=-\infty}^{m=\infty} \frac{m\pi}{d} sin\frac{2m\pi z_0}{d} cos\frac{m\pi z_0}{d} e^{-Dt(m\pi/d)^2} e^{-vt/l_a}. \tag{3.6}$$

The temporal profile of the flux magnitude is obtained by integrating j_z over the whole transmitted surface as:

$$I_{trans}(t) = 2\pi \int_{R=0}^{R=\infty} j_z R dR. \tag{3.7}$$

The expression for the transmitted intensity is found as:

$$I_{trans}(t) = \frac{D}{d} \sum_{m=1}^{m=\infty} \frac{m\pi}{d} sin\left(\frac{m\pi L}{d}\right) e^{-Dt(m\pi/d)^2} e^{-vt/l_a}. \tag{3.8}$$

The total transmitted intensity is obtained by integrating the temporal profile of (eq. 3.8):

$$I_{total} = \int I_{trans}(t) dt. \tag{3.9}$$

The expression for the total intensity is:

$$I_{total} = \frac{1}{\pi} \sum_{m=1}^{m=\infty} \frac{m sin\frac{m\pi L}{d}}{m^2 + \frac{vd^2}{l_a D\pi^2}}. \tag{3.10}$$

Using the equivalence: $\sum_{k=1}^{k=\infty} \frac{k \sin kx}{k^2+a^2} = \frac{\pi}{2} \frac{\sinh a(\pi - x)}{\sinh a\pi}$, one writes the total intensity as[12-14]:

$$I_{total} = \frac{sinh\left[(3/l_t l_a)^{1/2}(d-L)\right]}{2sinh\left[(3/l_t l_a)^{1/2}d\right]} . \tag{3.11}$$

The average time taken by a diffuse photon to travel from the source location to the transmitted surface is :

$$\langle t \rangle = \frac{\int_0^\infty t\, I_{trans}(t)dt}{\int_0^\infty I_{trans}(t)dt} . \tag{3.12}$$

Assuming that the absorption is negligible i.e. $l_a - > \infty$, the average time is found to be:

$$\langle t \rangle = \frac{L(L+4z_0)}{2vl_t} . \tag{3.13}$$

In most cases, the thickness of the medium is much larger than the transport mean free path, $L >> l_t$. The average time is then given by[12, 14]:

$$\langle t \rangle \approx \frac{L^2}{2vl_t} . \tag{3.14}$$

The average distance travelled by the diffuse photon is obtained as:

$$\langle z \rangle = v\langle t \rangle \approx \frac{L^2}{2l_t}, \tag{3.15}$$

which is much longer than the path travelled by the ballistic/snake photons, $\approx L$.

For example, for L=10mm, l_t=1mm, the average distance travelled by the diffuse photons is 50mm which is five times as long as the distance travelled by the ballistic/snake photons of 10mm. If any absorption is introduced in the medium, the diffuse photons are attenuated as e^{-50/l_a} while the ballistic photons are attenuated as e^{-10/l_a} as a result of the absorption alone. Taking l_a as 200mm, the diffuse intensity is 0.78 and the ballistic/snake intensity is 0.95. The ballistic signal is 22% more than the diffuse signal. Increasing the absorption length to 50mm gives 0.36 for the diffuse photons and 0.82 for the ballistic photons. The ballistic light is now 227% more than the diffuse light and the most change happens in the diffuse signal(the diffuse signal changes from 0.78 to 0.36).

3.3 Experimental Methods

The Fourier gate imaging experimental set-up is shown in Fig. 3–1. Three CW semiconductor laser sources operating at 670 nm, 830 nm, and 1300 nm of power 9.5mW, 14.5 mW, and 4.5 mW, respectively are used to obtain shadow images of an object hidden behind the scattering medium. These wavelengths are of particular importance because they fall within the therapeutic window (700 nm to 1300 nm) where blood and melanin absorb weakly. This light penetrates deep into the body and reaches internal tissues. The light beam at 830nm goes through the two mirrors system. The light beam at the wavelength of 670nm is reflected by the first mirror and goes through the second mirror. The laser beam at 1300nm is reflected by the second mirror. The diameters of the beams are approximately 4mm. The laser light is expanded about six times (to assume plane

wave incidence) and collimated by the two-lens system onto an object sample placed behind a 1cm glass cell containing some scattering medium. The object consists of a grid sample of square openings of 1mm x 1mm. The scattering medium consists of intralipid particles diluted in water. The original 10% concentration of intralipid suspensions is diluted at the ratio of 1 to 50 and 1 to 18 for 2 % and 5.5 %, respectively. The average diameter of the intralipid scatterer is $0.4\mu m$. With water absorption, some scattered light are absorbed. The longer the wavelength, the more water absorbs. As can be seen from Fig. 3–2, at shorter wavelengths, the total cross-section is essentially the scattering cross section because the water absorption is negligible. At around 1 μm, water absorption becomes significant and the absorption cross section must be included into the total cross section. The absorption of the scattered light is more significant than that of the ballistic light because as mentioned above, the diffuse light travels a longer path ($\approx \frac{L^2}{2l_t}$) than the ballistic component ($\approx L$) where L is the thickness of the sample, l_t is the transport mean free path. Absorption does not however get rid of all the diffuse noise. To eliminate more of the noise, a spatial filter is used before the scattering medium.

The spatial filter system consists of a transform lens of focal length 5cm that Fourier transforms the light that falls on it, an aperture that cuts off the diffuse light at spatial frequencies higher than its cut-off frequency ($\frac{d}{2\lambda f}$) with d the diameter of the aperture, λ, the wavelength of the laser light, and f, the focal length of the lens, and an imaging lens of focal length 5cm which performs the inverse Fourier transform to yield an image of the object. For d=1mm, f= 5cm, and laser wavelength=670nm, the highest spatial frequency that can pass the spatial filter is 15 lines/mm. This means that the smallest size of discernible detail in the filtered image is about 67microns which is much bigger

than the size of the intralipid particles.

The lower spatial frequencies contain direct information from the object. By adjusting the spatial filter aperture to collect as much as possible the frequencies closer to the ballistic one (spot at the center in the Fourier plane) the contrast of the image can increase enormously.

Images were taken with various aperture sizes from 1mm to 5mm at 1mm step increment. The shadow was then detected by a PbS type infrared camera and displayed on a video monitor. The image signals were recorded and digitized by a 8–bit frame grabber and the transferred to a computer for signal analysis. Hard copies of the images were printed by a video printer.

Combining the results given for light attenuation in water vs wavelength from Ishimaru with Mie theory[15–16] assuming that the particle is a sphere of 0.4 μm diameter, the optical properties of the 2% concentration scattering medium were determined as follows: l_a=500 mm, g= 0.73, l_s= 0.66 mm, and l_t= 2.44 mm at 670 nm; l_a= 200 mm, g=0.64, l_s=1.09 mm, and l_t=3.02 mm at 830 nm; and l_a= 5mm, g=0.28, l_s= 2.57 mm, and l_t=3.57mm at 1300nm.

3.4 Results

Images of the grid sample through the 2% concentration for a 1 mm spatial filter opening are displayed in Fig. 3–3 for laser light wavelengths of 670 nm, 830 nm, and 1300 nm. Fig. 3–3 a shows the 2D image of the grid using 670 nm while Fig. 3–3 b displays the digitized intensity distribution along a line across the grid image as indicated in the image profiles. In these two figures, the transparent portions of the grid represented

by bright spots (or high intensity values) can be easily differentiated from the opaque sections of the grid represented by the blurry section (low intensity values) of the image.

Figs. 3–3c and d show the image and intensity profile for the 830nm incident light, respectively. The intensity profiles are either zero (dark regions) or high (bright regions). The image and intensity profile, corresponding to 1300 nm illumination are displayed in Figs. 3–3e and f. Again a clear image of the grid is obtained.

The 2D images and digitized profiles when the aperture diameter is increased to 4 mm are presented in Fig. 3–4. Fig. 3–4a shows the image for 670nm laser; the bright spots are observed on a blurry white background, indicating a poor image quality. The contrast of bright to dark background is reduced to about 50% as shown in the intensity profile (Fig. 3–4b). Nevertheless, the images and intensity profiles produced by 830 nm and 1300 nm lights still show remarkably good image quality (Figs. 3–4c-f).

Images and profiles of the grid through a high concentration (5.5%) intralipid medium for 1 mm spatial filter opening are displayed in Fig. 3.5. Figs. 3–5a–b show the results obtained for a 670nm laser; no image but a white background was observed. Because of the intense diffuse light produced by this concentration, no image was observed. For the 830 nm radiation, bright spots are located on a strong background but the grid is clearly observed (Fig. 3–5c). The signal passing through the transparent regions of the grid is greater than the background noise formed by the diffuse light (Fig. 3–5d). For the longer 1300 nm wavelength radiation, the image shown in Fig. 3–5e and f shows an excellent contrast. The bright region of the grid is clearly observed with high contrast.

When the aperture diameter is increased to 4 mm, we observe no information signals in the images from 670 nm and 830 nm lights (Figs. 3–6a-d); only white background

formed by the diffuse light is seen. The grid is completely hidden from view. However, for 1300 nm light, a perfect image of the grid with almost no diffuse noise (Figs. 3–6e and f) is detected.

3.5 Discussion

From these data, it is clear that the best images are achieved when the aperture diameter is the smallest, i. e. 1 mm and the light wavelength is the longest. There is no significant change for 830 nm and 1300 nm light as compared with that for 670 nm by opening the aperture from 1 mm to 5 mm for the 2 % concentration intralipid medium. This is because the small aperture allows only the portion of the light that scatters within a small angle from the axis of the transform lens to pass through. This small angular distribution of light consists mainly of the ballistic and snake components. The other portion , the diffuse signal is blocked by the filter whose cut-off spatial frequency is as specified above: $d/2\lambda f$. This is why a clear image is seen with a small spatial filter diameter. As the aperture diameter is increased, the intensity of the diffuse light is increased more rapidly than that of the ballistic light on the detector resulting in a blurry image. This blurring is not observed for 830 nm and 1300 nm lights which are not scattered as much as the 670 nm light. In addition, at 830 nm and 1300 nm, the host medium is partially absorbing; a good part of the scattered light is then absorbed by the medium. The images for longer wavelengths (830 nm and 1300 nm) remain clear and are not significantly affected by the aperture openings.

The contrasts of the images are computed from $(I_{max} - I_{min})/(I_{max} + I_{min})$, where I_{max} and I_{min} are the maximum and the minimum values of transmitted intensity, respectively. The ideal values of 100 % are obtained for 830 nm and 1300 nm but low

values under 35 % are obtained for 670 nm as displayed in Fig. 3–7 for the 2% medium. The low contrast value for 670 nm light comes from the high value of I_{min} which is the consequence of the high degree of scattering and the low degree of absorption of the medium at this wavelength. Changing the aperture from 1 mm aperture to 4 mm for the 5.5% medium, a steady decrease of the contrast is observed and no change in contrast occurs above 4 mm as presented in Fig. 3–8. The large amount of scattering in the higher concentration (5.5 %) scattering medium makes the grid more difficult to image.

Compared with 670 and 830 nm radiations, the 1300 nm radiation experiences the least amount of scattering and the most amount of absorption. The reduction in scattering and enhanced absorption for 1300 nm allows a good image to be obtained from 1 mm to 4 mm spatial apertures. For 670 nm and 830 nm radiations, the scattering cross-section is larger than that for 1300nm (Fig.3–2) and the images produced by setting the aperture diameter as small as 1mm are still poor. The absorption being negligible for these two laser wavelengths, most of the scattered light that exists paraxially with the ballistic light reaches the detector. Consequently, the image contrasts are lower for 670 nm and 830 nm as observed in Fig.3–8. For d=1 mm, the contrasts increase with increasing wavelength and are 2.6 % for 670 nm, 29 % for 830 nm, and 100 % for 1300 nm. For larger aperture openings, higher spatial frequencies pass through the spatial filter. Their presence contributes to the blurring of the image and the deterioration of contrast. For d=4 mm, the contrasts for 670 nm and 830 nm drop down to 1.6 % and 4.1 %, respectively, as shown in Fig. 3–8. The contrast for 1300 nm remains at 100 % for the same previously stated reasons. The increase in aperture size does not decrease the image contrast because there is little diffuse light transmitted through the intralipid medium for 1300nm laser

wavelength. This clearly shows that the scattering cross-section decrease to a low value for the long wavelength, 1300nm, and most of the transmitted light remains ballistic.

3.6 Conclusion

Images of a grid through two different concentrations of intralipid suspensions in water media for laser wavelengths of 670 nm, 830 nm, and 1300 nm using a spatial filter of different aperture sizes are measured. When the aperture diameter is set at 1 mm, the best images are observed because the higher spatial frequencies are removed. As the aperture diameter increases or the wavelength of the light decreases, the image quality decreases. For the lower concentration scattering medium, the 670 nm radiation produces the poorest images while those at 830nm and 1300nm remain relatively good. For the higher 5.5% concentration scattering medium, images for 670nm and 830nm are blurry with contrasts of 1.6% and 4.1%, respectively for 4mm aperture. These measurements demonstrate the advantage of using the 1300 light beam because of more absorption and less scattering of light. The best contrast is obtained for 1300nm light for all the aperture diameters. Tunable laser radiation from 1100nm to 1350nm emitted from Forsterite laser may be introduced to image breast tumor inside the human body.

This chapter shows that the Fourier gate imaging of an object hidden in a highly scattering medium is possible. A combination of increase in absorption and decrease in scattering significantly improves the image quality. Within the therapeutic window, the best wavelength to image a small particle appears to be 1300 nm.

3.7 References

1. B. B. Das, K. M. Yoo, and R. R. Alfano, "Ultrafast time-gated imaging in thick tissues: a step toward optical mammography," Opt. Lett. **18**, pp. 1092–1094, 1993.

2. J. C. Hebden, R. A. Kruger, and K. S. Wong, "Time Resolved imaging through a highly scattering medium," Appl. Lett. **30**, pp. 788–794, 1991.

3. P. P. Ho, P. Baldeck, K. S. Wong, K. M. Yoo, D. Lee, and R. R. Alfano, "Time dynamics of photon migration in semiopaque random media," Appl. Opt. **28**, pp. 2304–2310, 1989.

4. L. Wang, P. P. Ho, and R. R. Alfano, "Time-resolved Fourier spectrum and imaging in highly scattering media," Appl. Opt. 32, 5043–5048, 1993.

5. H. Cheng, Y. Chen, D. Dilworth, E. Leith, J. Lopez, and J. Valdmanis, "Two-dimensional imaging through diffusing media using 150–fs gated electronic holographic techniques," Opt. Lett. **16**, pp. 487, 1991.

6. K. M. Yoo, F. Liu, and R. R. Alfano, "Imaging through a scattering wall using absorption," Opt. Lett. **16**, pp. 1068, 1991.

7. J. J. Dolne, K. M. Yoo, F. Liu, and R. R. Alfano, "IR Fourier Space Gate and Absorption Imaging through random media," Lasers in Life Sciences **6**, pp. 1–11.

8. J. W. Goodman, *Introduction to Fourier Optics*, (McGraw Hill, New York, 1968).

9. A. Hecht, *Optics*, (Addison Wesley, New York, 1987).

10. See *Applications of Optical Fourier Transforms* edited by H. Stark (Academic Press, New York, 1982).

11. F. Liu, K. M. Yoo, and R. R. Alfano, "Transmitted photon intensity through biological tissues within various time windows," Opt. Lett. **19**, pp. 740–742, 1994.

12. M. Lax, V. Nayaramamurti, and R. C. Fulton, "Classical diffusive Photon transport in a slab," in Proc. of the Symposium on Laser Optics Of Condensed Matter edited by J. L. Birman, H. Z. Cummings, and A. A. Kaplyanskii (Plenum, New York, 1987), pp. 229–235

13. F. Liu, Ph. D. Thesis, The City University of New York, 1993.

14 J. H. Li, A. A. Lisyanski, T. D. Cheung, D. Livdan, and A. Z. Genack, "Transmission and Surface Intensity Profiles in Random Media," Europhys. Lett. **22**, pp. 675–680

15. K. M. Yoo, Ph. D. Thesis, The City University of New York, 1990.

16. A. Ishimaru, *Wave propagation and scattering in random media*, (Academic Press, New York, 1978).

17. H. C. van de Hulst, *Light Scattering by Small Particles*, (Dover, New York, 1981).

3.8 Figures

Figure 3.1 4-f imaging experimental set-up: F: ND filter, G: grid, R.M.: random medium, B/S. C.: Ballistic/Snake component, D. S.: Diffuse signal, S.P.: spatial filter, IR. Ca: Infrared camera, F. G.: Frame grabber.

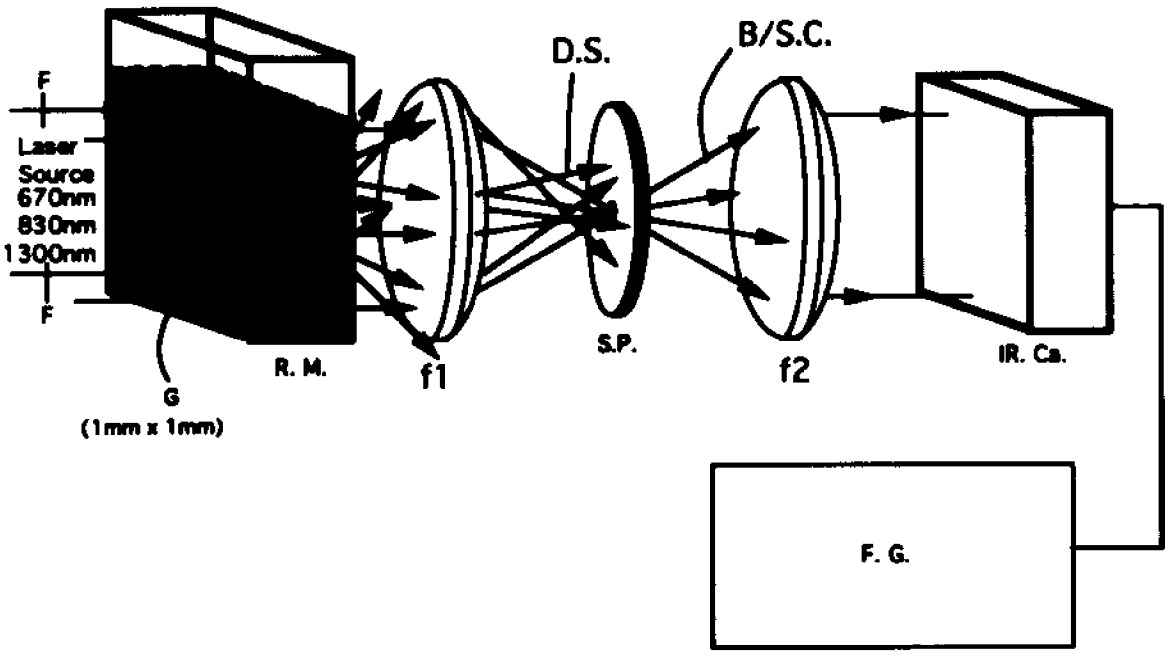

Figure 3.2 Optical density(OD) vs wavelength for water and intralipid suspensions in water inside a 1cm quartz cell. a) water; b) 5.5% intralipid concentration, and c) 2% concentration.

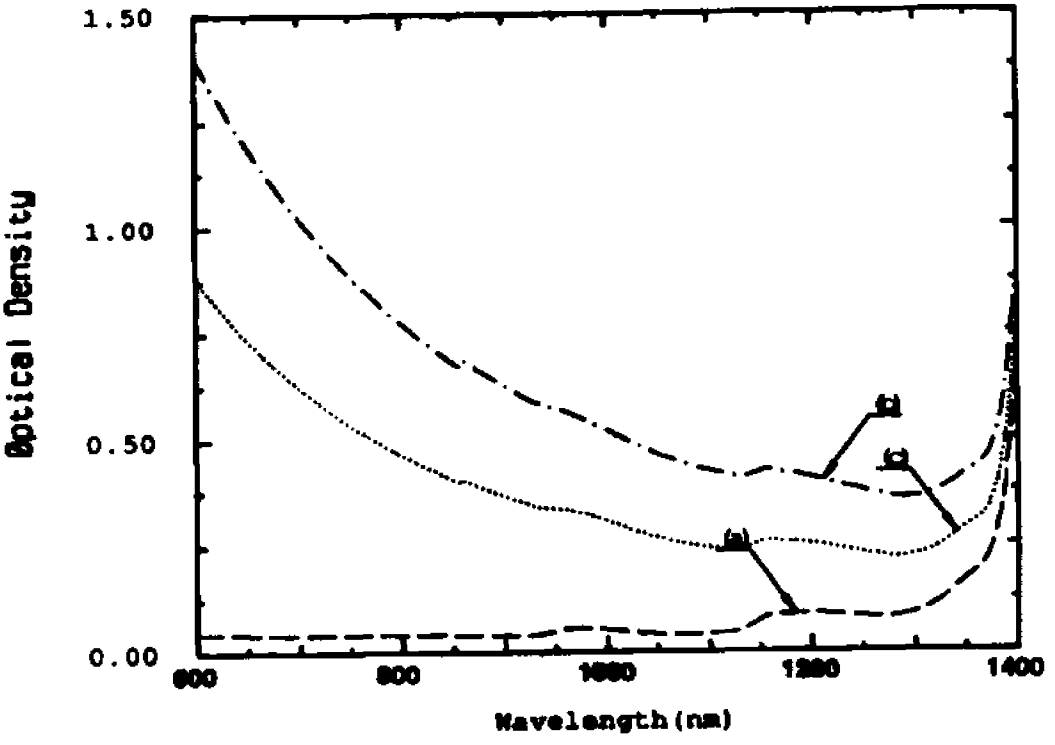

Figure 3.3 Images of a grid object placed behind a 1cm thick 2% intralipid suspensions illuminated by different laser light wavelengths for the spatial filter of diameter d=1mm. a) 2D image obtained from 670nm laser; b) 1D intensity distribution along a line across the grid image of a); c) 2–D image obtained from 830nm laser; d) 1D intensity distribution along a line across the grid image of c); e) 2–D image from 1300nm laser; and f) 1D intensity distribution for the grid image e).

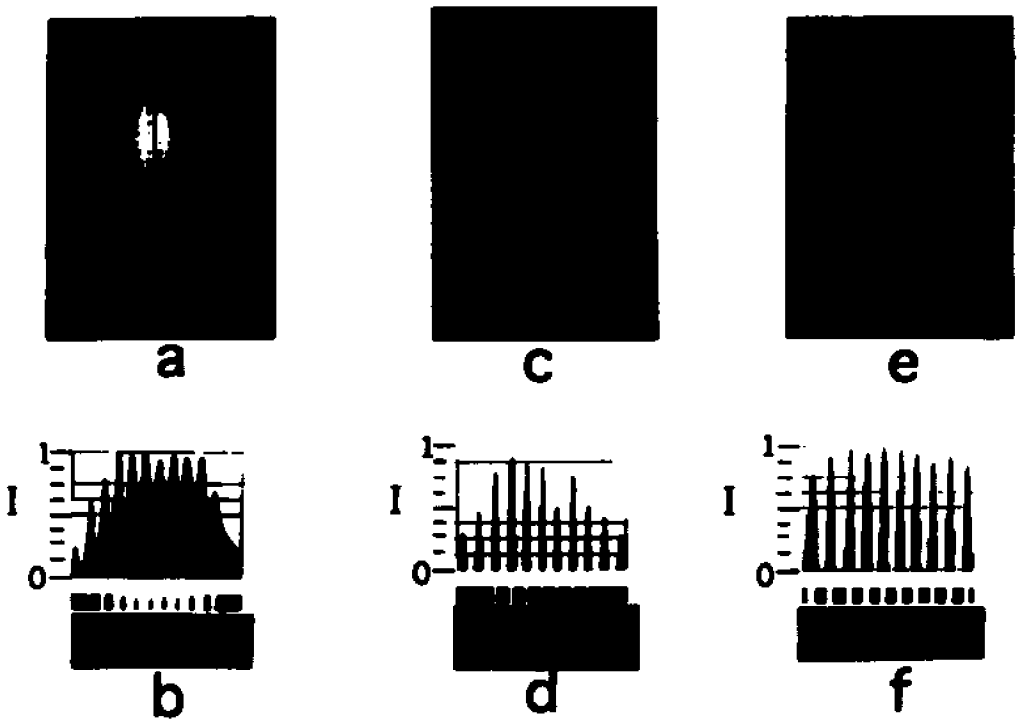

Figure 3.4 Images of a grid object placed behind a 1cm thick 2% intralipid suspensions illuminated by different laser light wavelengths for the spatial filter of diameter d=4mm. a) 2D image obtained from 670nm laser; b) 1D intensity distribution along a line across the grid image of a); c) 2-D image obtained from 830nm laser; d) 1D intensity distribution along a line across the grid image of c); e) 2-D image from 1300nm laser; and f) 1D intensity distribution for the grid image e).

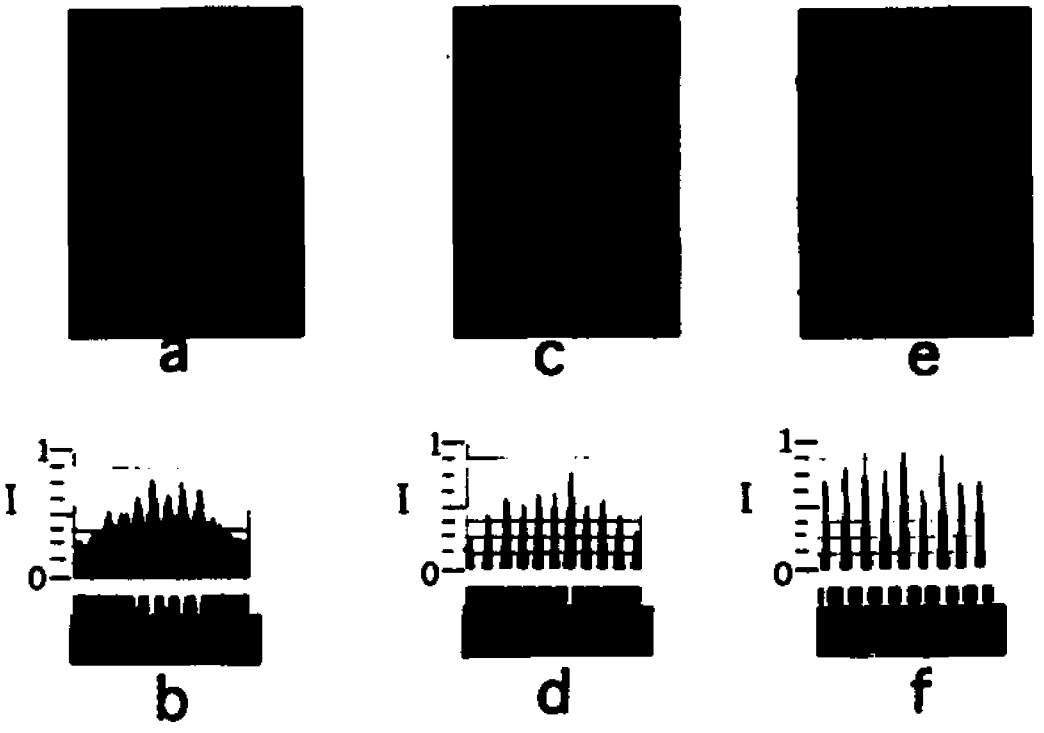

Figure 3.5 Images of a grid object placed behind a 1cm thick 5.5% intralipid suspensions illuminated by different laser light wavelengths for the spatial filter of diameter d=1mm. a) 2D image obtained from 670nm laser; b) 1D intensity distribution along a line across the grid image of a); c) 2–D image obtained from 830nm laser; d) 1D intensity distribution along a line across the grid image of c); e) 2–D image from 1300nm laser; and f) 1D intensity distribution for the grid image e).

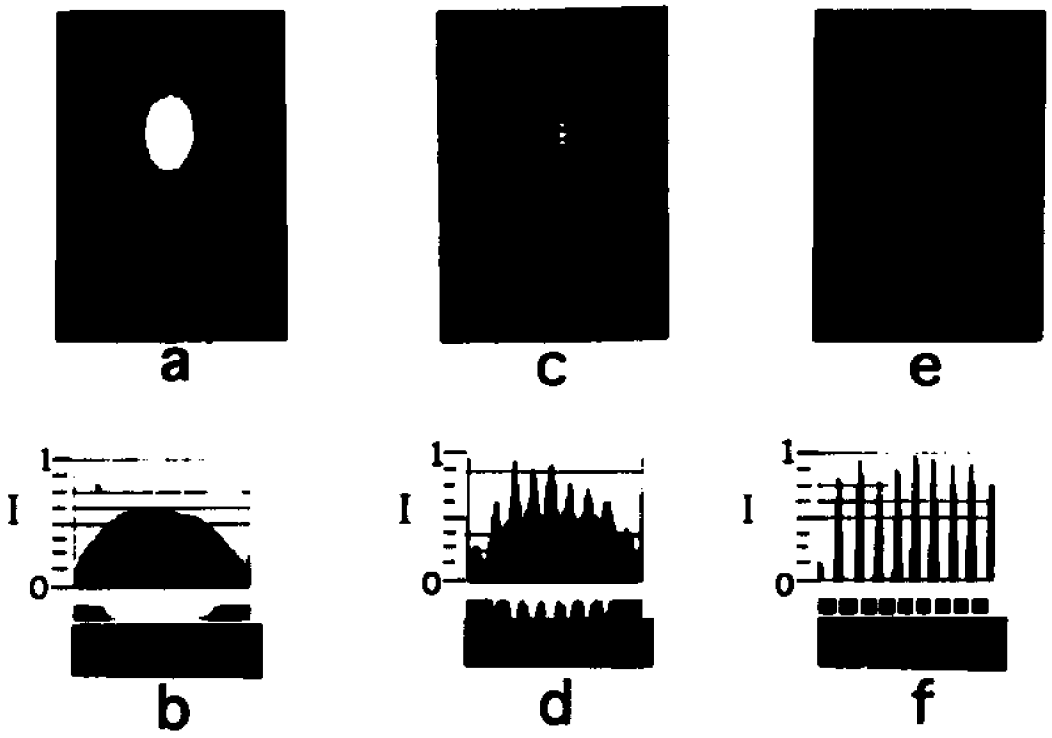

Figure 3.6 Images of a grid object placed behind a 1cm thick 5.5% intralipid suspensions illuminated by different laser light wavelengths for the spatial filter of diameter d=4mm. a) 2D image obtained from 670nm laser; b) 1D intensity distribution along a line across the grid image of a); c) 2–D image obtained from 830nm laser; d) 1D intensity distribution along a line across the grid image of c); e) 2–D image from 1300nm laser; and f) 1D intensity distribution for the grid image e).

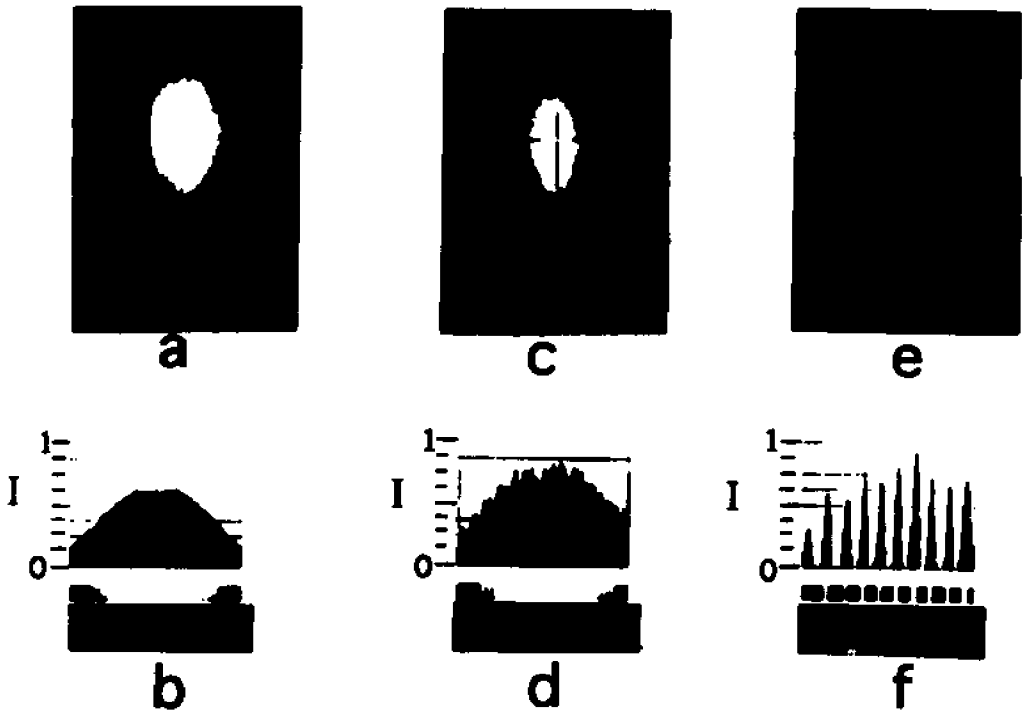

Figure 3.7 Contrast vs aperture diameters (spatial cut-off frequencies) for the three wavelengths for 2% concentration random scattering medium; a) 670nm; b) 830nm; and c) 1300nm.

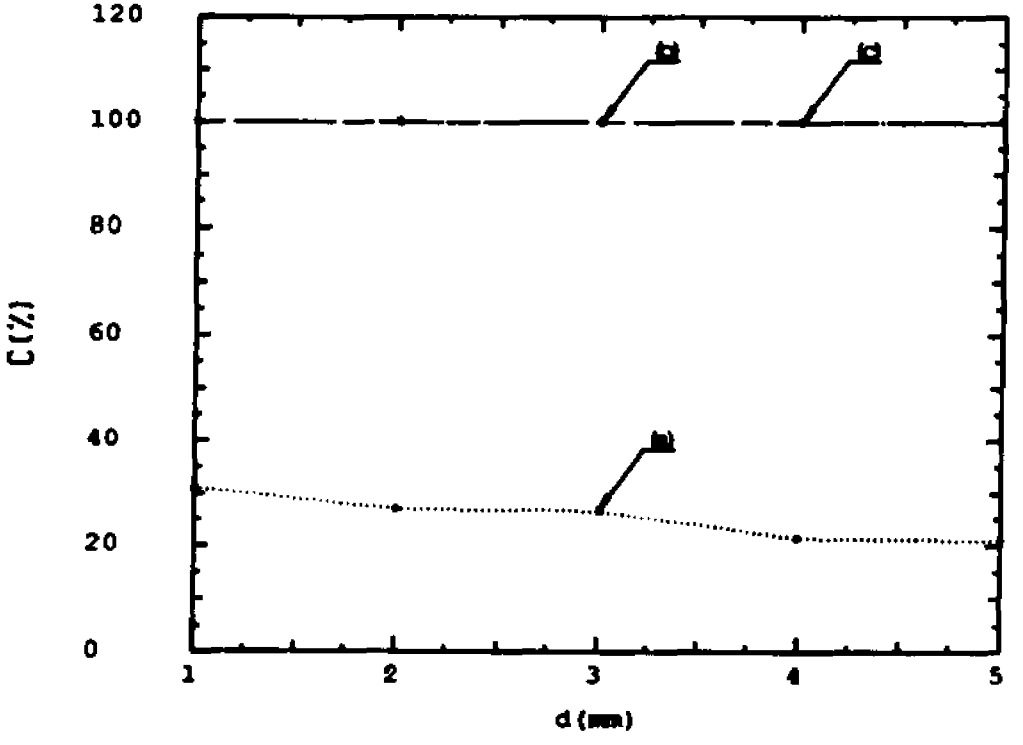

Figure 3.8 Contrast vs aperture diameters (spatial cut-off frequencies) for the three wavelengths for 5.5% concentration random scattering medium; a) 670nm; b) 830nm; and c) 1300nm.

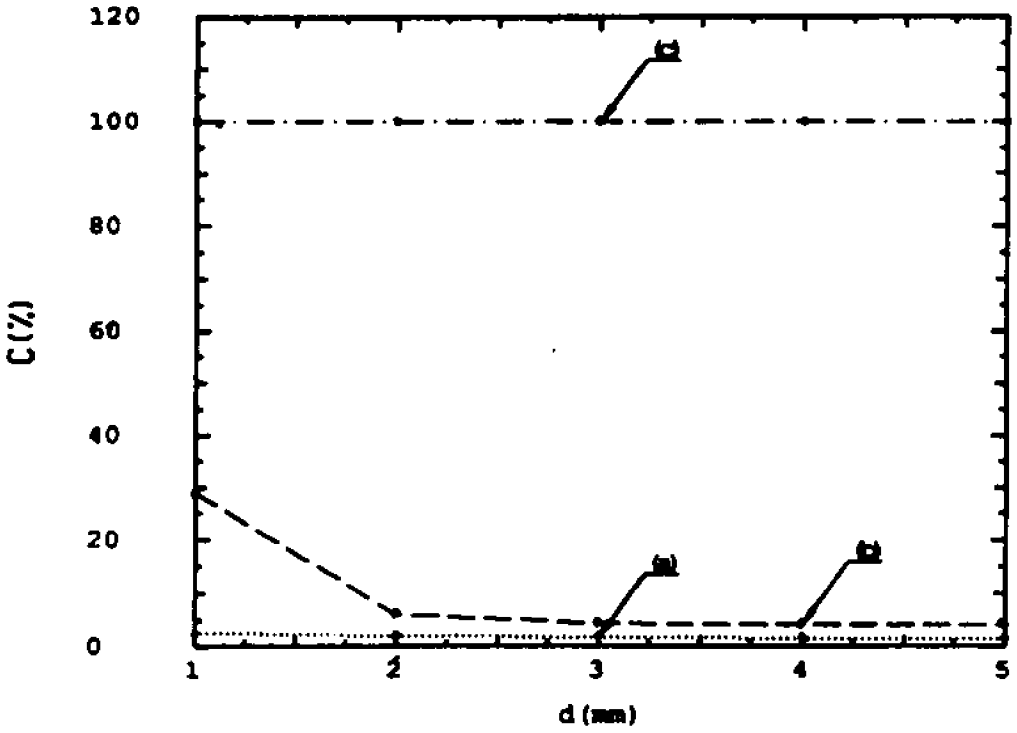

Chapter 4

A scattering layer on top of a scattering host medium

4.1 Introduction

Light scattering studies have usually been performed on a homogeneous slab where the optical properties such as the transport mean free path, l_t, the absorption length, l_a, and the index of refraction, n, are assumed to be constant throughout the scattering medium[1–4]. In reality, no medium is completely homogeneous. Many media that are encountered in real life are composed of layers. Determining the optical properties of the different underlying layers is of extreme importance if an object hidden in between or behind the layers is to be recovered or in case of therapy administer the right dose of photon radiation to a selected region. Over the years, light scattering studies to characterize layered media have been performed by several research groups[5–7]. Taitelbaum et al[5] have simulated a two-layer medium with same scattering lengths and different absorption lengths. The information from the underlying layer was obtained only when the absorption length of the upper layer was less than that of the bottom layer. Ostrander et al and Takatani et al[6–7] have showed that intensity contribution from deep layers may be obtained by increasing the source-detector separation in the backward direction. They have investigated the effects of the hemoglobin content, hemoglobin oxygen saturation on the net reflectance from the two-layer model. Fujimoto et al[8] have obtained delineated images of epithelial and sub-epithelial layers in soft tissues of mammalian gastro-intestinal tissues, and have used Optical Coherence Tomography[9] to image the anterior layers of the human eye. These models have for the most part used steady state light propagation. The steady–state

model can not describe the time light first reaches the layer nor can one transform the profile into frequency domain to see the contribution from each frequency. Such techniques can be applied only when using pulses of light.

In this chapter, a layer of intralipid suspensions placed on top of a huge solid piece of wax forming a single layer on a semi-infinite medium will be reconstructed using the Fourier transform model of the diffusion equation to fit the Fourier transform of the time-resolved experimental data. This inverse approach method in frequency domain from time domain data allows one to fit the different frequency modes of a scattered pulse profile.

4.2 Theory

The diffusion equation model is used to obtain the inverse parameters for the semi-infinite medium in which a layer of scattering medium is placed on another scattering medium of different optical properties. The simulated model for the structure is showed in Fig. 4–1. An impulse source of photons is placed at the surface of the intralipid layer of thickness d. A detector that collects the back-scattered photons is placed at a radial distance R from the photon source.

Figure 4.1 The experimental geometry for a two-layered medium:

Source detector is separated by R. The thickness of the top layer is d.

Wax- Intralipid Medium

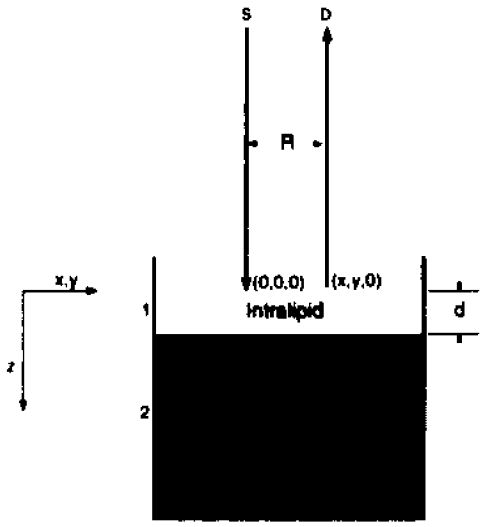

In this section, the theoretical model that is used to fit the experimental data to obtain the transport mean free paths and the absorption lengths of both scattering media and the thickness of the top layer is derived.

The model is obtained by solving the diffusion equation given by[10-11] :

$$\frac{\partial n(\vec{r},t)}{\partial t} = D\nabla^2 n(\vec{r},t) - \frac{v}{l_a} n(\vec{r},t) + \delta\left(\vec{r} - \vec{r'}\right)\delta(t) \qquad (4.1)$$

where n(r,t) is the photon density at position r at time t; D, the diffusion coefficient, is assumed to be constant in space and time; v , speed of light in the medium; l_a, the absorption length; $\vec{r} = (x, y, z)$ *and* $\vec{r'} = (x', y', z')$ are the positions of the detector and source, respectively.

The boundary conditions are given by[7, 12]:

$$
\begin{aligned}
n_1(x, y, z = 0, t) &= 0 \\
\frac{n_1(x, y, z, t)}{n_2(x, y, z, t)} &= \frac{n_1^2}{n_2^2} \quad at\ z = d \\
D_1 \frac{\partial n_1(x, y, z, t)}{\partial z} &= D_2 \frac{\partial n_2(x, y, z, t)}{\partial z}\ at\ \ z = d
\end{aligned}
\tag{4.2}
$$

where n_1 and n_2 are the indices of refraction of the top and bottom layers, respectively. The subscripts 1 and 2 refer to the top layer and bottom medium, respectively. The boundary conditions show that the photon density is zero at the boundary z=0, that the photon densities at the boundaries of the two media are continuous to within a constant given by the square of the two indices of refraction, and that the photon fluxes at the boundaries of the two scattering media are continuous.

The diffusion equation (4.1) can not be easily solved in time and space for a layer of scattering medium placed on top of a scattering medium. Such difficulties can be reduced by transforming equation 4.1 into frequency domain. In the frequency domain, there will be two kinds of frequencies: one frequency ω which is the transform in time t and another frequency k which is the transform of space (x,y). To avoid difficulties in distinguishing specifically between the two transforms, the frequency domain corresponding to ω will be called temporal frequency domain and the one corresponding to k will be called spatial frequency domain. The phrase "frequency domain" will be reserved to the general transform into ω *and* k.

The Fourier transform $\hat{n}(k_x, k_y, z, \omega)$ of a function n(x,y,z,t) in time and space is defined as follows:

$$\hat{n}(k_x, k_y, z, \omega) = \int_{t=0}^{t=\infty} dt e^{i\omega t} \int_{y=-\infty}^{y=\infty} \int_{x=-\infty}^{x=\infty} e^{-ik_x x} e^{-ik_y y} n(x, y, z, t) dx dy \,. \tag{4.3}$$

The Fourier transform of 4.1 is obtained as follows. First, the Fourier transform of the term on the left hand side of (4.1) , after changing the order of integration, is:

$$\int_{y=-\infty}^{y=\infty} \int_{x=-\infty}^{x=\infty} \int_{t=0}^{t=\infty} dt e^{i\omega t} \frac{\partial n(x, y, z, t)}{\partial t} e^{-ik_x x} e^{-ik_y y} dx dy \,. \tag{4.4}$$

After integrating by parts with respect to time, this integral becomes:

$$-i\omega \hat{n}(k_x, k_y, z, \omega) = -i\omega \int_{t=0}^{t=\infty} dt e^{i\omega t} \int_{y=-\infty}^{y=\infty} \int_{x=-\infty}^{x=\infty} e^{-ik_x x} e^{-ik_y y} n(x, y, z, t) dx dy \,. \tag{4.5}$$

Second, in the same manner after integrating by parts with respect to the spatial coordinates x and y, the Fourier transform of the first term of the right hand side of 4.1 is obtained as:

$$D\left(-k_x^2 - k_y^2 + \frac{\partial^2}{\partial z^2}\right) \hat{n}(k_x, k_y, z, \omega). \tag{4.6}$$

The photon density $\hat{n}(k_x, k_y, z, \omega)$ is dependent on spatial frequencies k_x and k_y and temporal frequency ω. This frequency dependent density will be simply noted by $\hat{n}$.

Third, the Fourier transform of the second term of the right hand side of 4.1 is simply:

$$-\frac{v}{l_a} \hat{n}. \tag{4.7}$$

Fourth, the Fourier transform of the third term of the right hand side of 4.1 is, taking the position of the source at time t=0 to be (0,0,z'), :

$$\delta(z - z') . \tag{4.8}$$

Setting eq. 4.5 equal to the sum of eqs. 4.6, 4.7, and 4.8, the Fourier transform of equation 4.1 becomes:

$$-i\omega\hat{n} = D\frac{\partial^2\hat{n}}{\partial z^2} + D(-k_x^2 - k_y^2)\hat{n} - \frac{v}{l_a}\hat{n} + \delta(z - z') . \tag{4.9}$$

Rearranging these terms and setting $k^2 = k_x^2 + k_y^2$ gives

$$\frac{\partial^2\hat{n}}{\partial z^2} - \left(k^2 + \frac{v}{l_a D} - \frac{i\omega}{D}\right)\hat{n} = -\frac{1}{D}\delta(z - z') . \tag{4.10}$$

The Fourier transforms of the boundary conditions are:

$$\begin{gathered} \hat{n}_1(k_x, k_y, z = 0, \omega) = 0 \\ \frac{\hat{n}_1(k_x, k_y, z, \omega)}{\hat{n}_2(k_x, k_y, z, \omega)} = \frac{n_1^2}{n_2^2} \quad at\ z = d \\ D_1\frac{\partial\hat{n}_1(k_x, k_y, z, \omega)}{\partial z} = D_2\frac{\partial\hat{n}_2(k_x, k_y, z, \omega)}{\partial z}\ at\ z = d. \end{gathered} \tag{4.11}$$

The time dependent partial differential diffusion equation has been transformed into a frequency dependent ordinary differential equation. The solution to this equation (eq. 4.10) in the top layer can be divided into two parts: one part for an infinite medium (fundamental solution) with a source at z' and another part so that the total solution

satisfies the boundary conditions. The solution in the second layer has no fundamental part since there is no source there.

The fundamental solution in frequency domain to this equation for an infinite medium and a source at z' is given by:

$$\hat{n} = Ae^{-|z-z'|\sqrt{k^2+\frac{v}{l_a D}-\frac{i\omega}{D}}}, \tag{4.12}$$

where A is an arbitrary constant to be determined from the source intensity. Integrating eq. 4.10 over a small path from $z' - \varepsilon$ to $z' + \varepsilon$ gives:

$$\int_{z'-\epsilon}^{z'+\epsilon} dz \frac{\partial^2 \hat{n}}{\partial z^2} = -\frac{1}{D}\int_{z'-\epsilon}^{z'+\epsilon} dz \delta(z - z') . \tag{4.13}$$

Note that the integral of the second term of the left hand side of eq. 4.10 is zero since the function is continuous. The first derivative is discontinuous however over that interval. These are the fundamental properties of Green's functions[13-14]. Solving eq. 4–13 gives :

$$\frac{\partial \hat{n}}{\partial z}\Big|_{z'-\epsilon}^{z'+\epsilon} = -\frac{1}{D} . \tag{4.14}$$

Taking the derivative of the photon density (eq. 4–12) gives:

$$\frac{\partial \hat{n}}{\partial z} = \begin{cases} -\left(\sqrt{k^2+\frac{v}{l_a D}-\frac{i\omega}{D}}\right) Ae^{-(z-z')\sqrt{k^2+\frac{v}{l_a D}-\frac{i\omega}{D}}} & z>z' \\ \left(\sqrt{k^2+\frac{v}{l_a D}-\frac{i\omega}{D}}\right) Ae^{-(z'-z)\sqrt{k^2+\frac{v}{l_a D}-\frac{i\omega}{D}}} & z<z' \end{cases} . \tag{4.15}$$

Replacing these expressions into eq. 4–14 and setting $\epsilon -> 0$ gives:

$$A = \frac{1}{2D\sqrt{k^2 + \frac{v}{l_a D} - \frac{i\omega}{D}}} . \tag{4.16}$$

Setting $\eta = \sqrt{k^2 + \frac{v}{l_a D} - \frac{i\omega}{D}}$, one can write eq. 4.12 as

$$\hat{n} = \frac{1}{2D\eta} e^{-\eta|z-z'|} . \tag{4.17}$$

This is the photon density in frequency domain(spatial and temporal) for a point source in an infinite medium.

The other part of the solution for layer 1 is obtained by replacing the source term in eq. 4.10 by zero and is given by:

$$\frac{1}{2D_1\eta_1}(Be^{-\eta_1 z} + Ce^{\eta_1 z}) \tag{4.18}$$

The total solution in the first layer is given by adding 4–17 and 4–18:

$$\hat{n}_1 = \frac{1}{2D_1\eta_1}\left(e^{-\eta_1|z-z'|} + Be^{-\eta_1 z} + Ce^{\eta_1 z}\right). \tag{4.19}$$

The solution for the second layer is:

$$\hat{n}_2 = \frac{E}{2D_2\eta_2} e^{-\eta_2 z} . \tag{4.20}$$

The coefficients B, C, and E are frequency dependent and are determined from the boundary coefficients (eq. 4.11). The values of B and C are:

$$C = \frac{e^{\eta_1 z_0} - e^{-\eta_1 z_0}}{1 + \frac{D_1\eta_1 n_1^2 + D_2\eta_2 n_2^2}{D_1\eta_1 n_1^2 - D_2\eta_2 n_2^2} e^{-2\eta_1 z_1}}$$

$$and\ B = -C - e^{-\eta_1 z_0}. \tag{4.21}$$

The coefficient E is of no importance here since only the flux in the backward direction is being considered. Hereafter, only the density in the first layer is considered.

Usually, the experimental data can be taken only at a few spatial points. This makes it almost impossible to be able to take the spatial Fourier transform of the experimental data. To have enough spatial points, one would need a special scanning apparatus that could scan the whole surface of the scattering medium. In contrast, with the synchroscan streak camera, the temporal profile can have easily 1000 points. The temporal Fourier transform of the experimental data can be easily performed with these temporal points. To go around this problem, one can invert transform the calculated photon density from spatial frequency domain and fit the experimental data in temporal frequency domain.

The inverse Fourier transform from spatial frequency domain(k_x, k_y) to spatial domain(x,y) is given by:

$$\hat{n}_1(x, y, z, \omega) = \frac{1}{(2\pi)^2} \int\int e^{i(k_x x + k_y y)} \hat{n}_1(k_x, k_y, z, \omega) dk_x dk_y. \tag{4.22}$$

This integral can be performed much simpler in cylindrical coordinates. Setting

$$\begin{aligned} x &= R\cos\phi \\ y &= R\sin\phi \\ k_x &= k\cos\theta \\ k_y &= k\sin\theta \\ R^2 &= x^2 + y^2 \\ k^2 &= k_x^2 + k_y^2 \end{aligned} \tag{4.23}$$

gives

$$\hat{n}_1(x,y,z,\omega) = \frac{1}{(2\pi)^2}\int_0^{2\pi}\int_0^{\infty} e^{ikR(\cos\theta\cos\phi+\sin\theta\sin\phi)}\hat{n}_1 k\,dk\,d\theta\,. \tag{4.24}$$

Noting that

$$\int_0^{2\pi} e^{ikR\cos(\theta-\phi)}d\theta = 2\pi J_0(kR)\,. \tag{4.25}$$

one writes Eq. 4.24 as

$$\hat{n}_1(x,y,z,\omega) = \frac{1}{2\pi}\int J_0(kR)\hat{n}_1 k\,dk \tag{4.26}$$

Replacing $\hat{n}_1$ in eq. 4.26 gives:

$$\hat{n}_1(x,y,z,\omega) = \frac{1}{4\pi D_1}\int_0^{\infty}\frac{k}{\eta_1}J_0(kR)\left\{B e^{-\eta_1 z} + C e^{\eta_1 z} + e^{-\eta_1|z-z_1|}\right\}dk \tag{4.27}$$

which is the photon density in the first layer in temporal frequency domain. The dependence of the photon density on ω is through η_1 repeated here for convenience:$\eta = \sqrt{k^2 + \frac{v}{l_a D} - \frac{i\omega}{D}}$. The density in time is given by :

$$n_1(x, y, z, t) = \frac{1}{2\pi} \int_{\omega} \hat{n}_1(x, y, z, w) e^{-i\omega t} d\omega. \tag{4.28}$$

Solving this integral is tedious. For this reason, the parameters of the layers will be reconstructed in frequency domain. The flux in temporal frequency domain in the back-scattered direction is given by:

$$\vec{J}_1 = -D_1 \frac{\partial \hat{n}_1(x, y, z, w)}{\partial z}. \tag{4.29}$$

The magnitude of the back-scattered photon flux is:

$$J_1(x, y, z, \omega) = \frac{1}{4\pi} \int_0^{\infty} k J_0(kR) \Big\{ -B e^{-\eta_1 z} + C e^{\eta_1 z} + e^{-\eta_1 |z - z'|} \Big\} dk. \tag{4.30}$$

This equation of the photon flux (eq. 4.30) in the backscattered direction will be used to find the inverse parameters of the intralipid layer and the wax medium.

Typical curves of the calculated photon flux(eq. 4.30) for different heights of the top layer ranging from 3mm to 12mm are shown in Fig. 4–2 for l_{t1}=3.1mm, l_{t2}=1.6mm, and R=20mm. These plots show that as the top layer thickness increases, the back-scattered intensity becomes larger and larger. The peak intensity increases by about 65% from

d=3mm to d=6mm and by 25% from d=6mm to d=8mm. For large thickness of the top layer, the back-scattered profiles are pretty much close to each other; only an increase of about 8% in the peak intensities is calculated when the thickness of the top layer is increased from d=8mm to d=12mm. In Fig. 4–3, the profiles given in Fig. 4–2 are normalized where the four curves are multiplied by a factor to bring all the intensity values at frequency $\omega = 0$ to the same level. The shapes for d=8mm and d=12mm are very close to each other. Therefore, it may be difficult to uniquely reconstruct a layer with thickness about half the source-detector separation. As the thickness of the layer decreases, the sensitivity of the scattered intensity to the layer thickness increases as is seen for d=8mm and d=6mm. The width of the profiles becomes narrower as the thickness of the top layer decreases. The narrowing of the profile in frequency domain is equivalent to a broadening of the pulse profile in the time domain.

4.3 Experimental methods

The set-up to experimentally investigate the layers is shown in Fig. 4–4. A colliding pulse mode-locked (CPM) dye laser produces ultrashort laser pulses of 100fs duration at 625nm wavelength and at a repetition rate of 82 MHz. The beam diameter is approximately 5mm. The average power of the laser beam is about 10mW. The beam is split in three parts: one part goes to the photodiode that triggers the streak camera; another small part is used as a reference to monitor the stability and to mark the arrival time of the signal. The main part used as the photon source is focused by a lens to about 300 μm spot size onto a layer of intralipid scattering medium, 0.25% by volume (transport mean free path l_{t1}=3 mm), placed on top of a solid piece of wax (l_{t2}=1.5 mm) contained in a cylindrical glass cup 88mm height x 80mm diameter. The height

of the intralipid is varied by extracting some intralipid solution and raising the container containing the two layers so that the fiber detector always touches the top layer in the perpendicular direction. The height of the wax medium is kept fixed at 55mm.

The detector is a multimode optical fiber of 400 μm core size and is placed at different distances from the source. The optical fiber delivers the light to the streak camera to be time-resolved and a CCD camera system detects the signal. The time resolution of the streak camera is about 10ps. The gain of the streak camera is kept fixed at maximum (gain 5) to avoid errors in the number of photons detected by changing from one gain to the other. To maintain the detected signal at safe level for the streak camera without affecting the signal to noise ratio, only neutral density filters are removed or added as needed. The neutral density factor is taken into account when processing the data so that the backscattered light intensity profiles can be compared to each other for the same amount of input energy. The slow speed of the streak camera is used to obtain the whole intensity profile. The intensity values in the absolute intensity profiles are given as a fraction of the input energy.

These experimental values of the transport mean free path are obtained by independent experiments where data obtained from light scattered from homogeneous wax medium are fitted with the diffusion equation model.

4.4 Results

The scattered temporal pulse profile along with the fitting from diffusion theory from a homogeneous wax medium is displayed in Fig. 4–5a. The source to detector separation in the back-scattered direction is 25mm. The best fit is found to be for lt (wax)=1.5mm.

A typical transmitted pulse profile for a homogeneous medium of intralipid scatterers of l_t=3mm for a source detector separation of $20l_t$ is shown in Fig. 4–5b.

The experimental temporal profile for the top layer of thickness d=10mm, R=S-D=20mm, l_{t1}=3mm, l_{t2}=1.5mm is shown in Fig. 4–6. The peak intensity is about 1.4×10^{-9}. The intensity values come down to 0 for times more than about 1600ps.

Fig. 4–7 shows the experimental temporal profile when the top layer thickness is d=6mm, the source to detector distance is R=S-D=20mm, and l_{t1}=3mm and l_{t2}=1.5mm. The peak intensity increases to 0.85×10^{-9} compared to the peak intensity when the thickness of the top layer is 10mm. The temporal pulse profile is broader for d=6mm. Such observation can be seen from the theoretical frequency profiles plotted above where the bandwidth (FWHM) increases as the top layer thickness increases. This narrowing of the temporal pulse profile for d=10mm can be explained as follows: As the thickness of the top layer increases, the detected back-scattered signal comes from light that has propagated mostly in the top layer. Since the top layer is less scattering than the bottom layer, the signal coming from the top layer only tends to be narrower and of higher peak intensity than the light that has reached both layers.

4.5 Discussion

4.5.1 Inverse fitting procedures

The aim of the fitting is to determine the optical parameters of the two layers and the height of the top layer. The procedure to do the fitting is as follows and is showed in the flow-chart below. First, the experimental data is obtained in time. The temporal profiles are then transformed into temporal frequency domain. Each transformed data profile is then compared with the temporal Fourier transform profile of the photon flux obtained

from the diffusion theory. Different combinations of l_t, l_a, and d are used to compute the photon flux. The set of parameters that matches best the experimental data is used as the inverse parameters of the scattering medium.

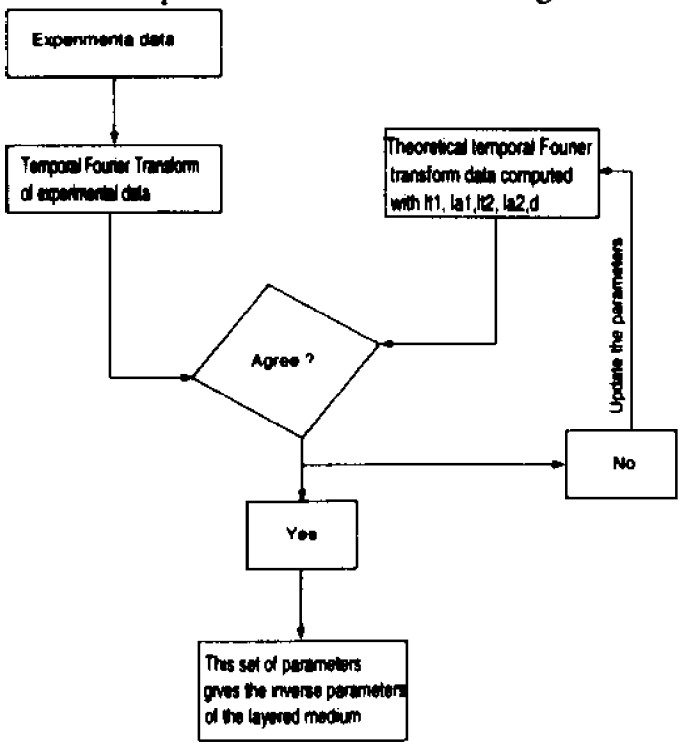

4.5.2 Reconstruction of the layers

Reconstruction of the temporal pulse profile given in Fig. 4.6 where the experimental optical parameters are: l_{t1}=3mm, l_{t2}=1.5mm , d=10mm and a source detector separation, R=20mm, are shown in Figs. 4–8 and 4–9. The transport mean free path for the top and bottom layers are obtained as $l_{t1} = 3.1mm \pm 0.2mm$, and $l_{t2} = 1.6mm \pm^{\infty}_{0.2mm}$ as compared to the experimental values of l_{t1}=3mm, and l_{t2}=1.5mm, respectively. The height of the top layer is found to be about $10mm \pm 2mm$. To assess the uniqueness of the fitting parameters, different curves with different transport mean free paths for the bottom layer are superimposed on the fitting curve. In Fig. 4–8 the transport mean free path of the bottom layer is varied. For this thickness of the top layer, however,

the bottom layer does not seem to influence too much the detected intensity when its transport mean free path is more than 1.6mm because values of transport mean free paths above 1.6mm do not change the fitting curve. Therefore this is not a unique fitting of l_{t2}. This is why a big error in l_{t2} is given above. In Fig. 4–9, the transport mean free path of the top layer is varied. Clear differences are seen as l_{t1} is varied from below to above the fitting parameter. For this thickness of the top layer, the parameters of the bottom layer are not unique. This situation was predicted above by comparing the shapes of the curves for different depths of the top layer.

Fig. 4–10 shows the reconstruction of the temporal profile given in Fig. 4–7 where the height of the intralipid suspension forming the top layer is 6mm. The parameters are reconstructed as follows $l_{t1} = 3.1mm \pm 0.2mm$, $l_{t2} = 1.6mm \pm 0.3mm$, and $d = 6 \pm 1mm$ as compared to the same experimental values l_{t1}=3mm, l_{t2}=1.5mm, and d=6mm. These parameters are very close to the experimental values. The uniqueness of this l_{t2} is verified by plotting curves with different l_{t2} on the same graph. As seen from these plots, the profiles look different for different l_{t2}. The parameters for this depth of the layer are more uniquely comparable to the experimental parameters.

These results show that it is indeed possible to reconstruct the parameters of a two layered scattering medium by using the diffusion equation. When the top layer is large (about 10mm), the transport mean free path of the bottom layer and the height of the top layer are not uniquely reconstructed. This limitation is because the backscattered light does not contain significant information from the bottom layer. The backscattered light is mainly from the top layer. If the bottom layer is made more scattering, more light will reach the detector and the parameters of the layers will be reconstructed more

accurately. This is showed in Fig. 4–7 where the difference between the profiles for l_{t2}=1.6mm and l_{t2}=1.1mm is clear.

When the top layer thickness is decreased to 6mm, however, the backscattered light contains much more significant informations from the bottom layer and this makes it possible to reconstruct more or less uniquely the parameters of the layers.

4.6 Conclusions

With the two-layered diffusion model, a two-layered scattered medium is reconstructed. The parameters of the top and bottom layers (l_{t1}, l_{t2}, and d) have been shown to match the theoretical ones obtained from diffusion theory for layers. When the depth of the top layer is large, no significant amount of backscattered light from the bottom layer reaches the detector. The parameters of the bottom layer are then not uniquely reconstructed. Almost any number more than 1.6mm for the transport mean free path for the bottom layer can fit the experimental data. The transport mean free path and the depth of the top layer fit the experimental data within 6% and 20%, respectively. For a lesser 6mm thickness of the top layer, both top and bottom layer parameters are more or less found with less error, about 17% in the depth. This gives a lot of hope in trying to image layered structures(skin, skull) that are highly scattering. Once the light can penetrate all the layers, it is indeed possible to reconstruct with minimal errors multiple structures. This difficulty in uniquely reconstructing the parameters of the scattering medium reveals the need for a better theory to reconstruct the optical parameters of a layered medium.

4.7 References

1. F. Liu, K. M. Yoo, and R. R. Alfano, " Should the photon flux or the photon density be used to describe the temporal profiles of scattered ultrashort laser pulses in random media," Opt. Lett. **18**, pp. 432–434, 1993.

2. K. M. Yoo and R. R. Alfano, "Determination of attenuation lengths arising from scattering and absorption from the temporal profile of the back-scattered pulse," Opt. Lett. **15**, pp. 276, 1990.

3. M. S. Patterson, B. Chance, and B. C. Wilson, "Time-resolved reflectance and transmittance for the non-invasive measurement of tissue optical properties," Appl. Opt. **28**, pp. 2331–2336, 1989.

4. A. H. Grandjbakhche, G. H. Weiss, R. F. Bonner, and R. Nossal, "Photon path-length distributions for transmission through optically turbid slabs," Phys. Rev. E **48**, pp. 810–818, 1993.

5. H. Taitelbaum, S. Havlin, and G. H. Weiss, "Approximate theory of photon migration in a two-layer medium," Appl. Opt. **28**, 2245–2249 (1989).

6. W. Cui and L. E. Ostrander, "The relationship of surface reflectance measurements to optical properties of layered biological media," IEEE Trans. on Biomed. Eng. **39**, pp. 194–201, 1993.

7. S. Takatani and M. D. Graham, "Theoretical analysis of diffuse reflectance from a two-layer tissue model," IEEE Trans. Biomed. Eng. **BME-26**, pp. 656–664, 1979.

8. J. A. Izatt, M. R. Hee, G. Tearny, G. M. Owen, E. Swanson, and J. G. Fujimoto, "Optical coherence microscopy," OSA Proceedings in Optical Imaging and Photon Migration, R. R. Alfano, ed. pp. 249–252, 1994.

9. J. A. Izatt, M. R. Hee, D. Huang, J. G. Fujimoto, E. A. Swanson, C. P. Lin, J. S. Schuman, and C. A. Puliafito, "Optical Coherence Tomography for Medical Diagnostics," SPIE series on Medical Optical Tomography: Functional Imaging and Monitoring, G. J. Muller, ed. pp. 450–472, 1993.

10. P. M. Morse and H. Feshback, *Methods of Theoretical Physics* (McGraw Hill, New York, 1953).

11. A. Ishimaru, *Wave propagation and scattering in random media*, (Academic Press, New York, 1978).

12. J. M. Schmitt, G. X. Zhou, and E. C. Walker, "Multilayer model of photon diffusion," J. Opt. Soc. A. 7, pp. 2141–2153, 1990.

13. I. Stakgold, *Green's Functions and Boundary Value Problems*, (John Wiley and Sons, New York, 1979).

14. S. L. Sobolev, *Partial Differential Equations of Mathematical Physics*, (Pergamon Press, New York, 1964).

4.8 Figures

Figure 4.2 Absolute calculated back-scattered intensity profiles in frequency domain for different depths of the top layer and fixed transport mean free paths and source-detector separation using eq. 4.30.

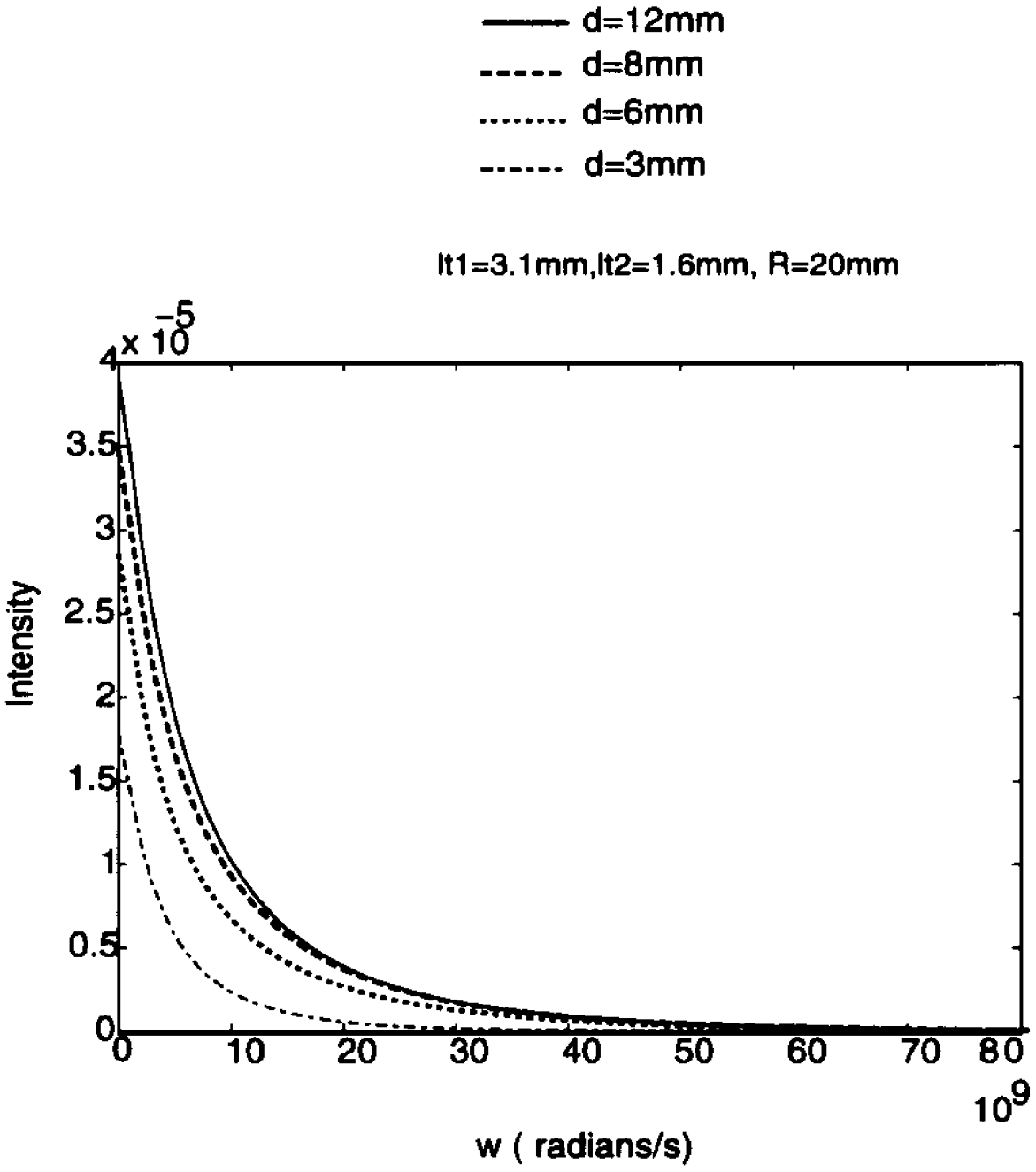

Figure 4.3 Normalized calculated back-scattered intensity profiles in frequency domain for different depths of the top layer and fixed transport mean free paths and source-detector separation using eq. 4.30.

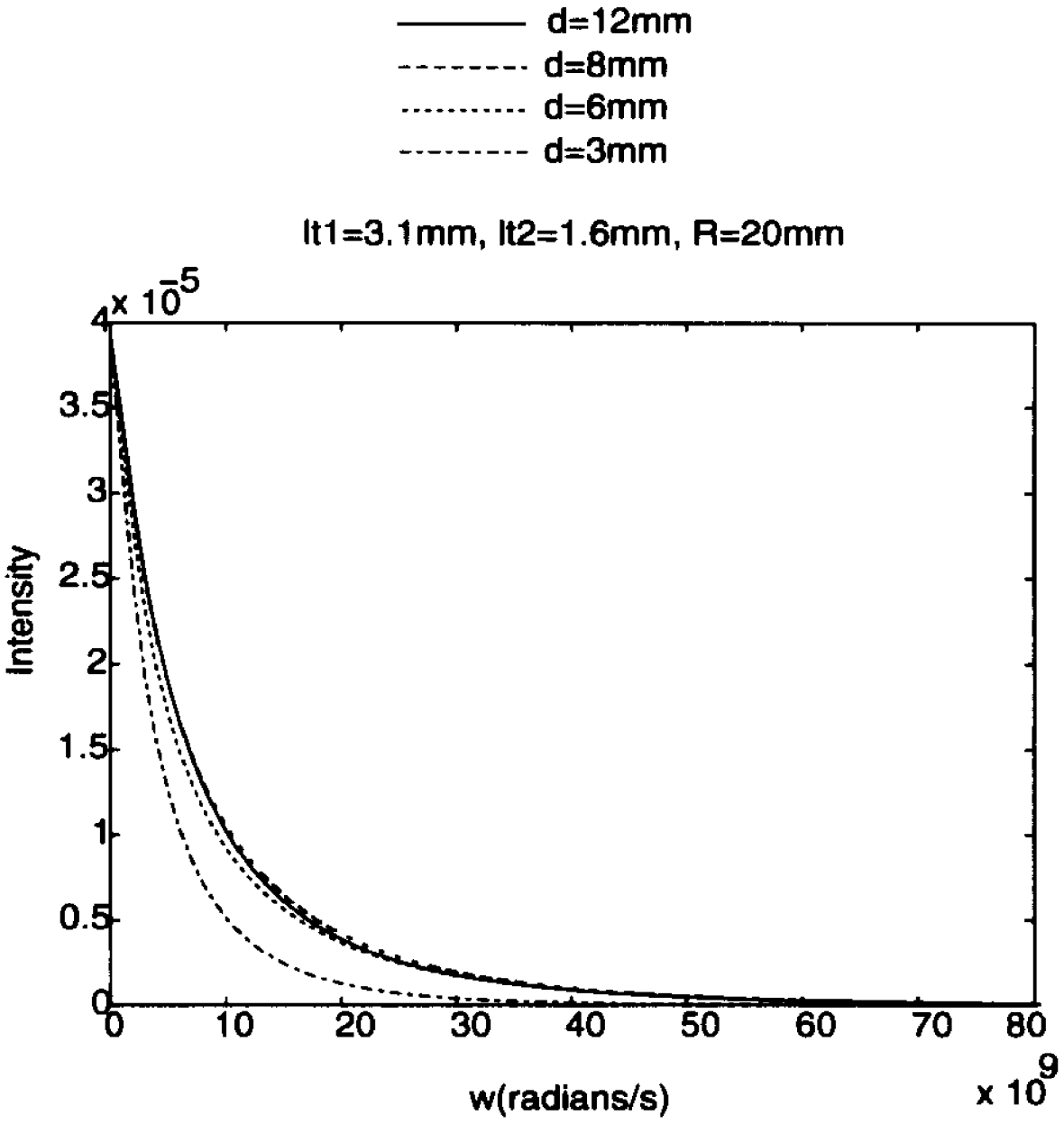

Figure 4.4 CPM light is incident on a scattering medium. The backscattered signal is collected by a fiber and time-resolved by an ultrafast streak camera and CCD detection system

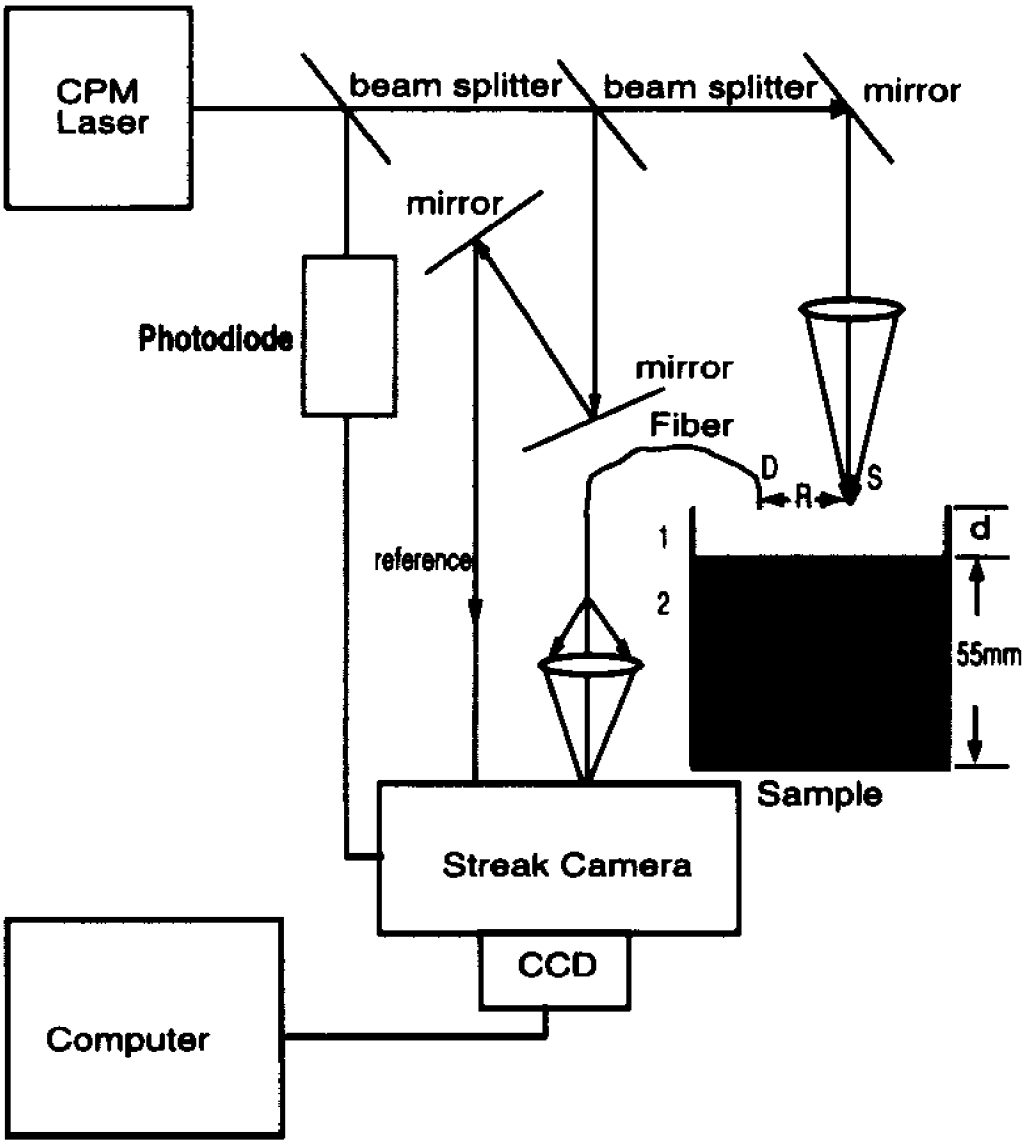

Figure 4.5 a)Fitting with the diffusion equation model of the intensity profile from a homogeneous sample of wax; b) Fitting with the diffusion model of the scattered pulse profile from a homogeneous sample of intralipid scatterers.

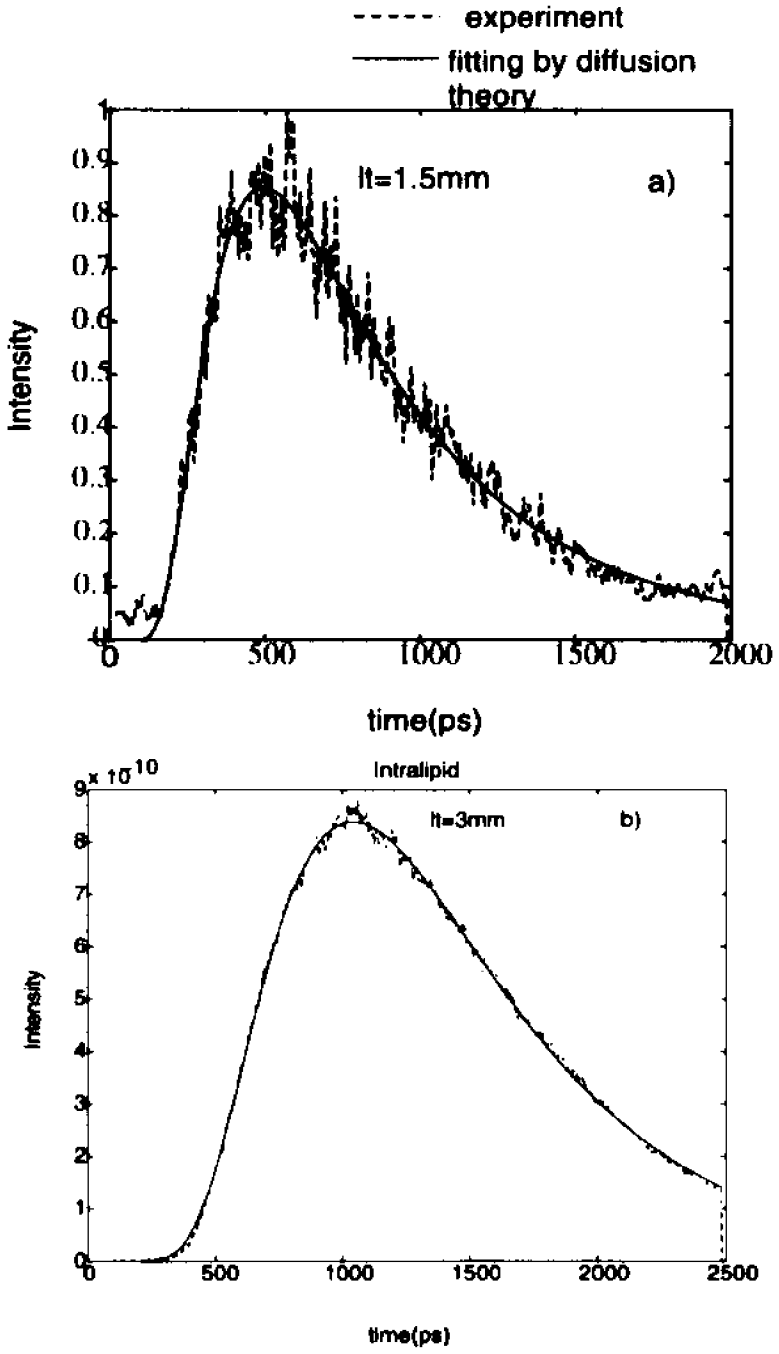

Figure 4.6 Temporal experimental profile of the back-scattered intensity from the two-layered medium. The depth of the top layer is 10mm.

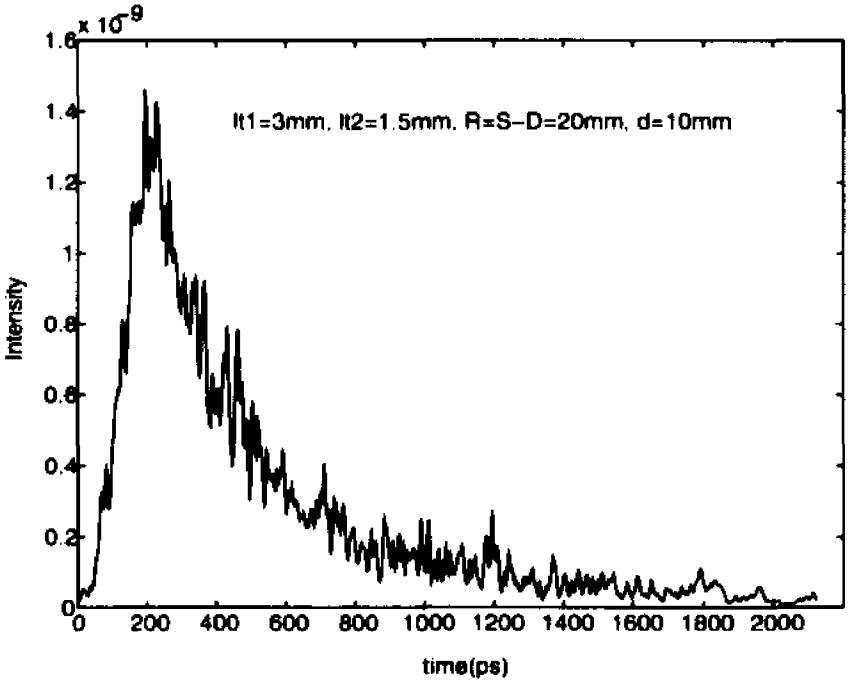

Figure 4.7 The temporal profile of light backscattered from a two-layered scattering medium. The depth of the top layer is 6mm.

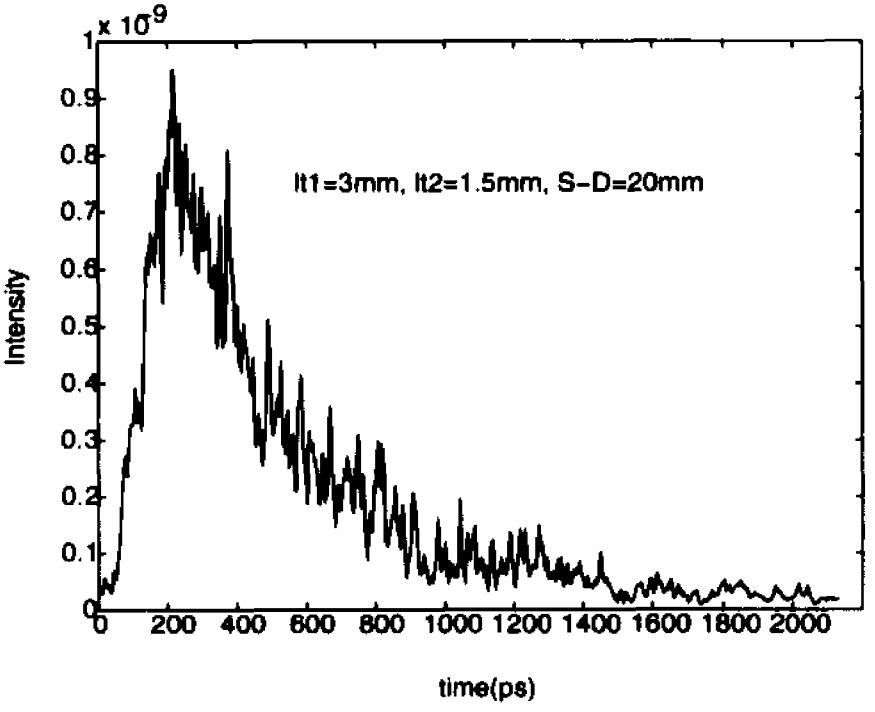

Figure 4.8 Experimental and theoretical fittings of back-scattered intensity profile from a two-layered random medium for a source-detector separation of 20mm. The transport mean free path of the bottom layer is varied to check for the uniqueness of the parameters of the bottom layer.

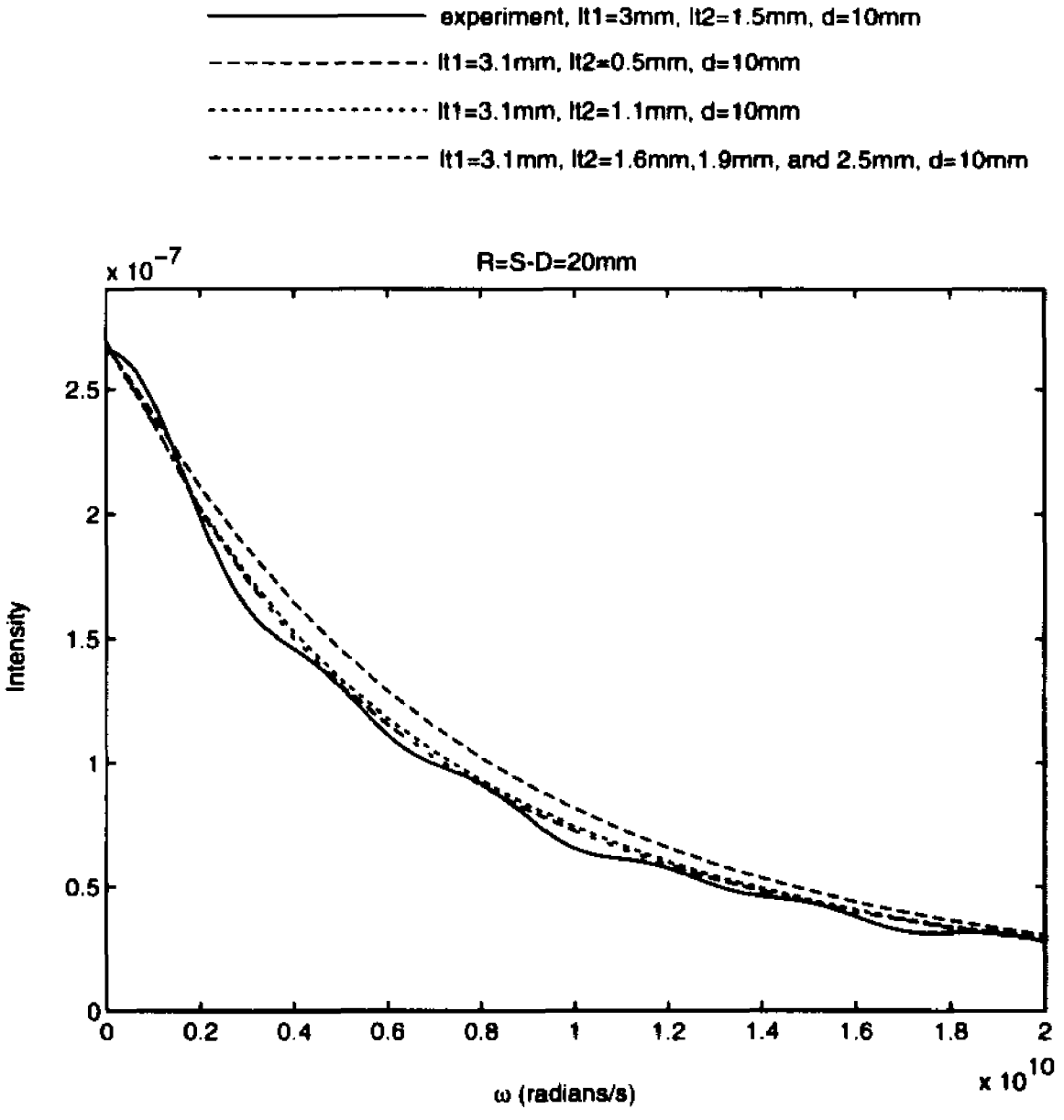

Figure 4.9 Experimental and theoretical fittings of back-scattered intensity profile from a two-layered random medium for a source-detector separation of 20mm. The transport mean free path of the top layer is varied to check for the uniqueness of the parameters of the top layer.

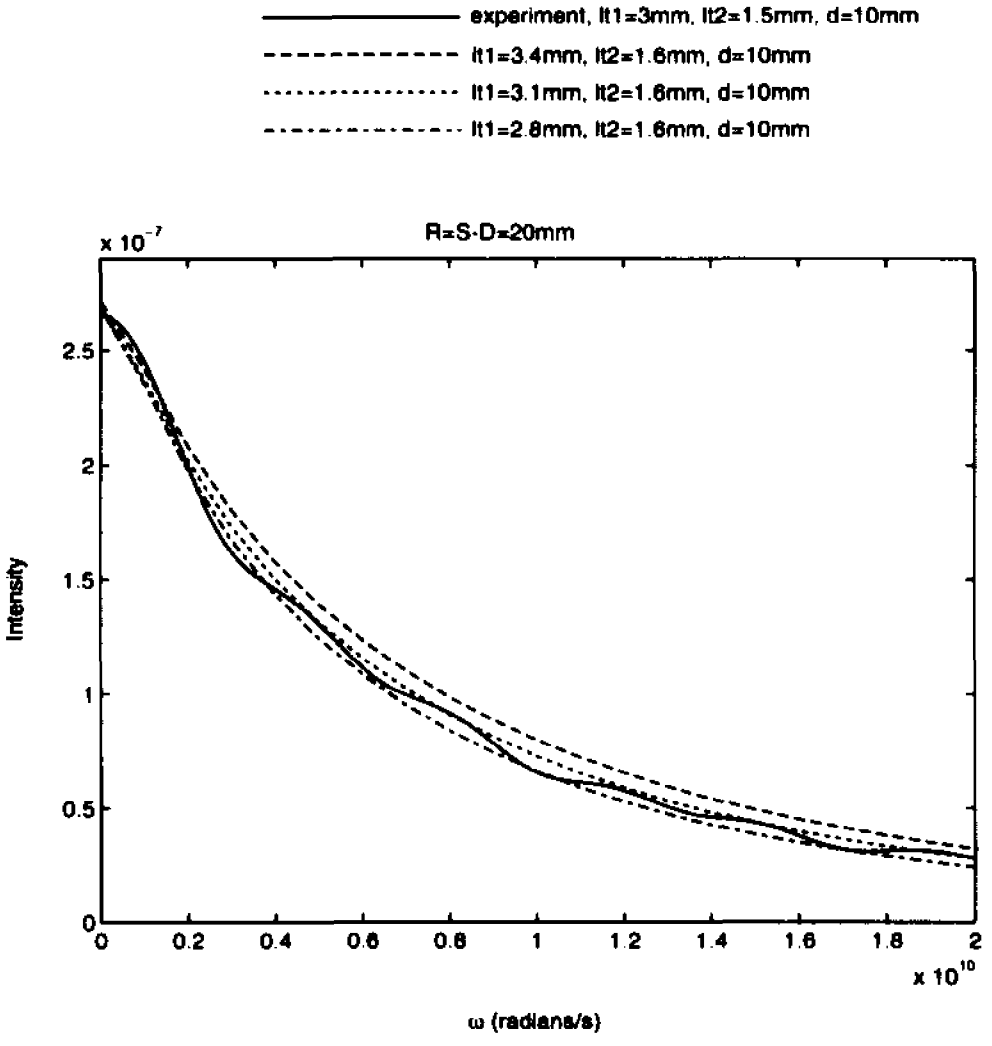

Figure 4.10 Experimental and theoretical fittings of back-scattered intensity profile from a two-layered random medium for a source-detector separation of 20mm. The transport mean free path of the bottom layer is varied to check for the uniqueness of the parameters of the bottom layer.

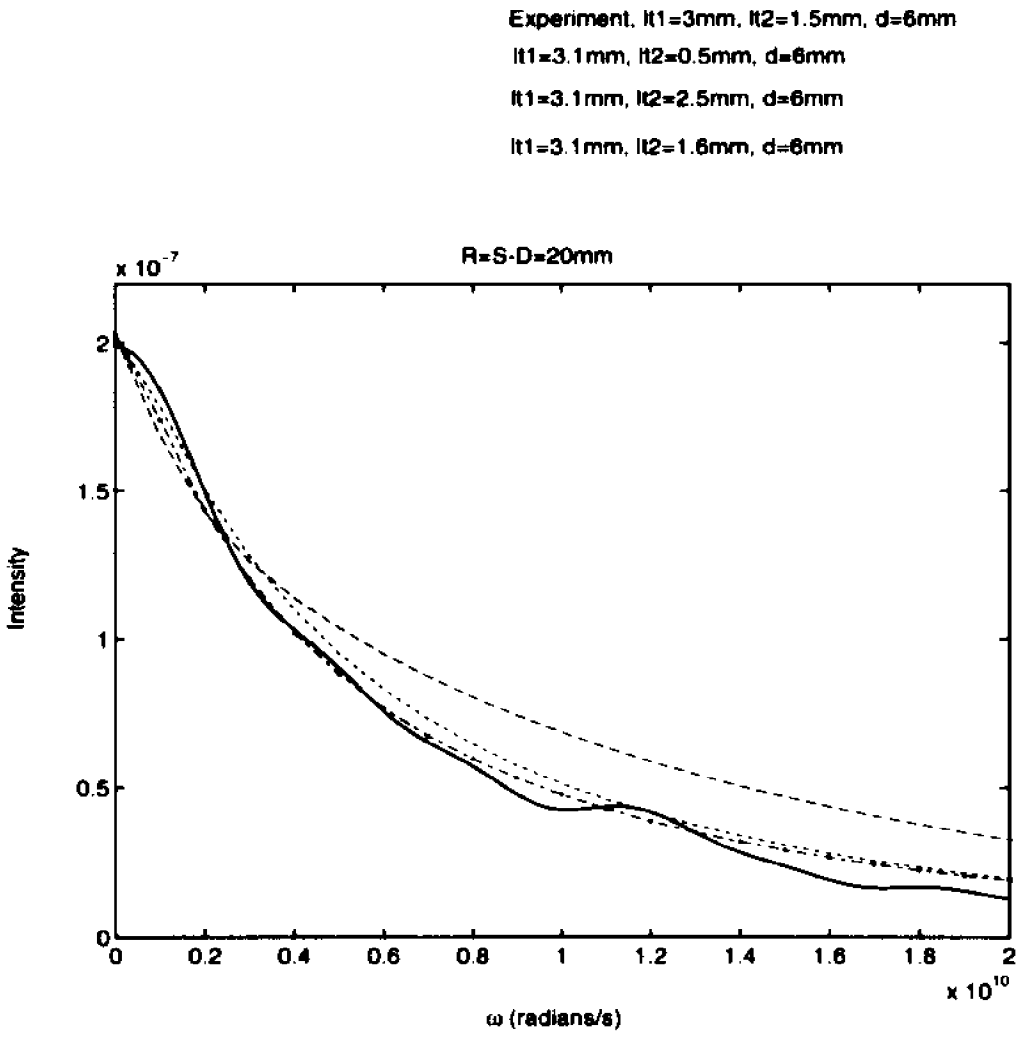

Chapter 5

Photon migration in a rectangular slab

5.1 Introduction

Photon migration in highly scattering media has been used to reconstruct hidden objects inside scattering media [1–5]. Several research groups have used the diffuse light to reconstruct the optical properties of the hidden object. In the reconstruction process, the weight function for each volume element is usually obtained using Monte Carlo simulations to calculate the collision densities. Different algorithms have been used. These algorithms include projection onto convex sets (POCS), conjugate gradient descent (CGD), and simultaneous algebraic reconstruction technique (SART). These simulations and algorithms require substantial amount of computer time[4–5]. For real life situations, these methods may not be of practical importance. In this chapter, we present a simple way to quickly evaluate the optical properties of the hidden object with respect to the reference medium. It will be shown that the intensities at a point for a detector oriented perpendicular to the medium surface decrease at all positions around a scattering medium as the medium becomes more and more scattering. This way, one can just look at the scattered intensity profiles and quickly estimate the properties of the object hidden inside the scattering medium with respect to those of the reference medium without using sophisticated mathematical equations and computer algorithms.

In this chapter, we will further show that the risetime and the peak intensity of the scattered pulse profile are all that are needed to obtain the actual parameters of the scattering medium.

To acquire a 3–dimensional reconstruction map of the hidden object using multiple detectors and a source of photons, one needs a reference data where the object is out of the scattering medium for each detector position. In real life, it is not possible to take the object out the medium and take data. It is possible, however, that one detector may be placed at such a position that the object has no influence on that particular detector reading. That reading is the reference data for that detector. Using one reference data and a suitable theory such as diffusion, we will show, in this chapter, that the reference data at any position around the scattering medium can be "measured".

5.2 Theory

The diffusion equation to be solved for slab of length, L and width, w is given by:

$$\frac{\partial n(\vec{r},t)}{\partial t} = D\nabla^2 n(\vec{r},t) - \frac{v}{l_a} n(\vec{r},t) + \delta(\vec{r})\delta(t) \tag{5.1}$$

where $n(\vec{r},t)$ is the photon number density at position $\vec{r} = (x,y,z)$ and time t; $D = \frac{vl_t}{3}$, is the diffusion coefficient; v, the speed of light in the medium; l_t, the transport mean free path of the medium at the operating laser wavelength; l_a, the absorption length; $\delta(\vec{r})\delta(t)$, the impulse source function at position 0 and time t=0.

In the diffusion approximation, the boundary condition used is that the photon density must vanish at the extrapolated boundaries z=0, $z=L+2z_0=d$, y=0, and $y=w+2y_0=h$ which are the medium length and thickness extended by twice the extrapolation lengths z_0 and y_0, respectively. The actual medium occupies the region of space from $z=z_0$ to $z=L+z_0$, $y=y_0$ to $y=w+y_0$. It will be assumed that z_0 and y_0 are both equal to $0.7104l_t$. The method of images is used to set the photon number density to zero at the extrapolated boundary.

The solution of eq. 5.1 for an infinite medium is given by [6–8]:

$$n(r,t) = \frac{1}{(4\pi Dt)^{3/2}} exp\left(-\frac{r^2}{4Dt}\right) exp\left(-\frac{vt}{l_a}\right). \tag{5.2}$$

To make the photon density zero at the extrapolated boundary z=0, a negative or image source is added to the infinite medium problem at z=-z'. The zero photon density condition at z=d can be met by adding two sources near z=2d, but then the boundary condition at z=0 is violated for time t more than or equal to 2d/c. To resatisfy the condition at z=0, two sources are placed near z=-2d. But now, the condition at z=d is violated. These boundary conditions and those in the y-direction can be met at all times by adding an infinite number of dipole sources all over the y-z plane as shown in Fig. 5–1. The medium is assumed to be infinite in the x-direction.

The photon number density for a slab of length L and width w, at a point (x,y,z) and time t with the impulse source located at (0,y',z') at time t=0 is given by the method of images (Fig. 5–1) as:

$$n(x,y,z,t) = \frac{S}{(4\pi Dt)^{3/2}} exp\left(-\frac{x^2}{4Dt}\right) exp\left(-\frac{vt}{l_a}\right) \tag{5.3}$$

where S is given by:

$$S = \sum_{n=-\infty}^{n=\infty} \left\{ exp\left[-(2nd + z' - z)^2/4Dt\right] - exp\left[-(2nd - z' - z)^2/4Dt\right] \right\} \cdot N$$
$$\sum_{m=-\infty}^{m=\infty} \left\{ exp\left[-(2mh + y' - y)^2/4Dt\right] - exp\left[-(2mh - y' - y)^2/4Dt\right] \right\} \tag{5.4}$$

Using the Poisson sum formula S may be written as:

$$S = 4\frac{\pi Dt}{d \times h} \sum_{n=-\infty}^{n=\infty} sin\frac{n\pi z'}{d} sin\frac{n\pi z}{d} exp(-\pi^2 Dtn^2/d^2) X \sum_{m=-\infty}^{m=\infty} sin\frac{m\pi y'}{h} sin\frac{m\pi y}{h} exp(-\pi^2 Dtm^2/h^2). \tag{5.5}$$

The photon flux is given by:

$$\vec{J} = -D\nabla n. \tag{5.6}$$

The photon fluxes for different directions around a slab of scattering medium as shown in Fig. 5–2 are given by:

a) Backscattering

For a detected oriented so as to pick up the backscattered light at the surface of the slab, the flux is given by:

$$J_z(x, y, z_0, t) = \left|\vec{J}(x, y, z_0, t)\right| = \left|-D\frac{\partial n}{\partial z}\right|_{z=z_0} \tag{5.7}$$

which evaluates to:

$$J_z(x, y, z_0, t) = \left|\frac{S_1}{(4\pi Dt)^{3/2}} exp\left(-\frac{x^2}{4Dt}\right) exp\left(-\frac{vt}{l_a}\right)\right|, \tag{5.8}$$

where

$$S_1 = \frac{1}{2t}\sum_{n=-\infty}^{n=\infty}\left\{f_1 exp\left[-(f_1)^2/4Dt\right] - (f_2) exp\left[-(f_2)^2/4Dt\right]\right\}X$$
$$\sum_{m=-\infty}^{m=\infty}\left\{exp\left[-(f_3)^2/4Dt\right] - exp\left[-(f_4)^2/4Dt\right]\right\}$$
$$where\ f_1 = (2nd + z' - z_0)$$
$$f_2 = 2nd - z' - z_0 \qquad (5.9)$$
$$f_3 = 2mh + y' - y$$
$$f_4 = 2mh - y' - y.$$

b) Transmission

The transmitted intensity, given by replacing the z_0 term in the flux expression in the back-scattered direction by d-z_0, is written as:

$$J_z(x, y, d - z_0, t) = \left|\vec{J}(x, y, d - z_0, t)\right| = \left|-D\frac{\partial n}{\partial z}\right|_{z=d-z_0} \qquad (5.10)$$

or

$$J_z(x, y, d - z_0, t) = \left|\frac{S_1}{(4\pi Dt)^{3/2}} exp\left(-\frac{x^2}{4Dt}\right) exp\left(-\frac{vt}{l_a}\right)\right|. \qquad (5.11)$$

where

$$S_1 = \frac{1}{2t}\sum_{n=-\infty}^{n=\infty}\left\{f_1 exp\left[-(f_1)^2/4Dt\right] - (f_2) exp\left[-(f_2)^2/4Dt\right]\right\} X$$
$$\sum_{m=-\infty}^{m=\infty}\left\{exp\left[-(f_3)^2/4Dt\right] - exp\left[-(f_4)^2/4Dt\right]\right\}$$
$$where\ f_1 = (2nd + z' - (d - z_0))$$
$$f_2 = 2nd - z' - (d - z_0),$$
$$f_3 = 2mh + y' - y,$$
$$and\ f_4 = 2mh - y' - y. \qquad (5.12)$$

c) Side Scattering

When the detector is oriented to collect the side scattering light in the y-direction, the expression for the flux is:

$$J_y(x, y, y_0, t) = \left|\vec{J}(x, y_0, z, t)\right| = \left|-D\frac{\partial n}{\partial y}\right|_{y_0}. \qquad (5.13)$$

The flux in the y-direction is given by:

$$J_y(x, y_0, z, t) = \left|\frac{S_2}{(1\pi Dt)^{3/2}} exp\left(-\frac{x^2}{4Dt}\right) exp\left(-\frac{vt}{l_a}\right)\right| \qquad (5.14)$$

with

$$S_2 = \frac{1}{2t}\sum_{n=-\infty}^{n=\infty}\left\{exp\left[-(f_{11})^2/4Dt\right] - exp\left[-(f_{22})^2/4Dt\right]\right\}X$$
$$\sum_{m=-\infty}^{m=\infty}\left\{f_{33}exp\left[-(f_{33})^2/4Dt\right] - f_{44}exp\left[-(f_{44})^2/4Dt\right]\right\} \quad (5.15)$$

where

$$f_{11} = 2nd + z' - z,$$
$$f_{22} = 2nd - z' - z,$$
$$f_{33} = 2mh + y' - y_0, \quad (5.16)$$
$$f_{44} = 2mh - y' - y_0.$$

The detection at the side y=h-y_0 is obtained by replacing y_0 by h-y_0 in eq. 5.14 above for the flux J.

The expressions for the flux given in this section will be used to fit the experimental data to obtain the optical parameters of the scattering medium. The theoretical profiles and integrated areas in this chapter will be multiplied by the collection solid angle of the optical fiber detector described below. The absolute intensity values of the theoretical profiles and integrated areas are given as a fraction of the input energy.

The expression for J is used to compute profiles for different transport mean free paths of a scattering medium and a fixed absorption length l_a=400mm. The size of the slab is L=60mm, w=60mm. The source and detector axes lie on the same y-z plane. The source location is y=30mm+y_0 and z=z_0.

Fig. 5-3 shows the computed transmitted intensity profiles for different transport mean free paths; a) is for l_t=3mm, b) is for l_t=2mm, and c) is for l_t=1mm. The source to

detector distance is 60mm in the z direction (S-D(z)=60mm) and 0 in the y-direction (S-D(y)=0mm). The areas under the scattered pulse profiles are 17.1×10^{-7}, 8.61×10^{-7}, and 1.82×10^{-7}, respectively. The peaks and the areas of the profiles computed from low scattering medium to higher scattering medium decrease.

Fig. 5–4 shows the side-scattering profiles computed for source detection distance S-D(y)=30mm and S-D(z)=30mm a) l_t=3mm, b) l_t=2mm, and c) l_t=1mm. The areas under these respective curves are 5.53×10^{-6}, 3.13×10^{-6}, and 0.91×10^{-6}. The peak intensities and the integrated intensities both decrease as the transport mean free paths decrease.

Fig. 5–5 shows the backscattered intensity profile at a source detector separation of 25mm in the y-direction and S-D(z)=0 for a) l_t=3mm, b) l_t=2mm, and c) l_t=1mm. The areas under the profiles are respectively, 11×10^{-6}, 6.37×10^{-6}, 2.19×10^{-6}.

The peak intensities and the areas under the profiles decrease as the medium becomes more and more scattering. It was expected that the intensity peaks and/or the areas would increase for a more scattering medium in the back-scattered direction at least . Such is clearly not the case. The intensity values for the more scattering medium are slightly higher than the values for the less scattering medium for later times. The same observation is made for forward and side scattering profiles.

5.3 Experimental Methods

The experimental set-up is showed in Fig. 5–6. To study the scattering profiles around a rectangular slab, a colliding pulse mode-locked laser generating ultrashort laser pulses of 100fs duration is used as the source operating at 625nm at a frequency of 82MHz is used as the source. The average power of the laser pulses is 10mW. The light is divided in three parts by a thin glass slide; one part goes to the photodiode that

triggers the streak camera. Another part goes to an optical fiber of 400μm diameter that is used as a reference to monitor the stability of the laser and to mark the zero arrival time. As the laser intensity fluctuates, this reference pulse is used to bring the incident light to the same level so that the detected intensities can be compared with each other. The detected intensities will be given as a fraction of the input intensity. The main part of the divided beam is focused onto an optical fiber of 400μm diameter by a lens of focal length, f=7.5cm. The other side of the optical fiber is screwed onto a plastic cell 60mm x 60mm by a SMA connector at the middle of the input side of the slab. The cell is filled with intralipid scattering suspensions. The original 10% stock of Intralipid is diluted with water to form three samples of different concentrations. The concentrations used are 2.4% (2.4% of the original 10%), 3.6%, and 4.7%. The height of the scattering medium is 12cm: The bottom boundary is 5cm from the source detector plane.

The scattered pulses are detected by four optical detector fibers of 400μm core diameter. These optical fibers are assumed to collect light at all angles. The detector fibers are positioned around the cell slab. One is placed in the backscattered direction (fiber d) 25mm away from the source. The other two (b, c) facing each other are placed each at the middle of the two sides perpendicular to and 30mm from the input side of the slab. The two axes are collinear but perpendicular to the axes of the source and back scattered fibers. The optical fibers b and c are separated by the slab thickness of 60mm. Another optical fiber detector (a) facing the source is positioned in the middle of the exit side of the slab to collect transmitted signals.

Calibration of the detected intensity is performed to make sure that for any fixed level of intensity incident upon the optical fibers, under the same conditions, each yields

the same output. This is performed by putting alternatively each of these optical fiber detectors at the exit surface of a highly scattering medium at exactly the same location and oriented in the same direction to detect the transmitted intensity. Given that all the conditions are the same, the same intensity should be obtained. To account for the missing intensity, a calibration factor is added to the appropriate fibers.

The output sides of the four fiber detectors and the reference one are connected in a bundle and screwed onto the streak camera. The surfaces of the fibers are all on the same plane on the input slit of the streak camera. The streak camera time resolves the signal that falls unto it with a resolution of 10ps. A gain of 3 and the slow speed 4 are used.

5.4 Results

The absolute detected intensity values and integrated areas are given as a fraction of the input energy. Fig. 5–7 shows the experimental curves together with their fittings (broken lines) for the transmitted intensity profiles: 5–7a is for l_t=3mm, l_a=480mm and area=1.0×10^{-6}; 5–7b is for l_t=2.1mm, l_a=492mm, and area=0.58×10^{-6}; and 5–7c for l_t=1.7mm, l_a=559mm, and area=0.35×10^{-6}. The fittings are performed using the diffusion model described in the theory section. Excellent agreement is observed between experiment and theoretical model. The peak intensities and the areas under the profiles decrease as the medium becomes more scattering. To assess the errors in the fitting parameters l_t=3mm and l_a=480mm, intensity profiles using transport mean free paths of 2.8mm, 3.1mm, and 3.2mm and fixed l_a=480mm are plotted on the same graph(Fig. 5–8a). The profiles plotted with l_t=2.8mm and 3.2mm are largely different from the fitting profile. The error in l_t can then be safely taken as 0.2mm. This error will be even less as the medium becomes more scattering. The error in the absorption length

is obtained by proceeding in a similar fashion for l_a=430mm, 480mm, and 530mm and fixed l_t=3mm(Fig. 5–8b). The profiles for l_a=430mm and 530mm are clearly different from the fitting profile which has l_a=480mm. The error in the absorption length is then about 50mm.

Fig. 5–9 shows the intensity profiles in time and fittings for the side scattering light. The intensity profiles collected by the optical fibers #b and #c on the side of the cell slab are symmetric. For this reason, only the intensity captured by #c is presented. The areas under the pulse profiles are 3×10^{-6}, 2.3×10^{-6}, and 1.75×10^{-6} for a, b, and c, respectively. The optical parameters are found to be about the same as for Figs. 5-7a, b,c. Fig. 5–10 represents the backscattered intensity with areas 4.96×10^{-6}, 4.4×10^{-6}, and 3.5×10^{-6}. The optical parameters given in Fig. 5–10 are the parameters obtained from fitting the transmitted profiles.

In all the cases, forward scattering, side scattering, and back scattering there is a consistent decrease in the peak intensities and the integrated areas under the profiles. At late times (Figs. 5–7, 5–9, and 5–10), the intensity of the higher scattering medium increases slightly over that of the less scattering medium but that increase is not enough to significantly influence the total area under the profiles. These observations are consistent with those made from the theoretical curves plotted for times as long as 6 ns.

5.5 Discussion

The decrease observed in transmitted and side scattering intensity profile for decreasing l_t is not surprising. However, the decrease in the backscattered signal was not expected. If all intensity profiles decrease, then where does the energy go? An answer to this question is addressed in this section.

Without loss of generality, consider the same slab as before but with infinite width w. For the transmitted intensity, it is estimated that the total scattered light is approximated by [9-11] $\frac{z_0}{l}$.

The solution to the diffusion equation for the back-scattered signal, using Poisson integral formula, is:

$$n(R,t) = \frac{exp\left(\frac{-R^2}{4Dt}\right)}{4\pi Dtd} \sum_{m=-\infty}^{m=+\infty} sin\frac{m\pi z'}{d} sin\frac{m\pi z}{d} exp\left(-Dt\left(\frac{m\pi}{d}\right)^2\right) exp\left(-\frac{vt}{l_a}\right). \quad (5.17)$$

The flux in the back-scattered direction is given by Fick's law of diffusion as:

$$\vec{J}(R,t) = -\hat{z}\frac{exp\left(-\frac{R^2}{4Dt}\right)}{4t} \sum_{m=1}^{m=\infty} \frac{m}{d^2} sin\frac{2m\pi z_0}{d} exp\left(-Dt\left(\frac{m\pi}{d}\right)^2\right) exp\left(-\frac{vt}{l_a}\right). \quad (5.18)$$

Integrating the flux magnitude over the whole backscattered surface

$$I_{sur}(t) = 2\pi \int_{R=0}^{R=\infty} J(R,t) R dR \quad (5.19)$$

gives

$$I_{sur}(t) = D \sum_{m=1}^{m=\infty} \frac{m\pi}{d^2} sin\frac{2m\pi z_0}{d} exp\left(-Dt\left(\frac{m\pi}{d}\right)^2\right) exp\left(-\frac{vt}{l_a}\right). \quad (5.20)$$

The total intensity in the back-scattered direction is obtained by integrating over all time the intensity on the back-scattered surface and is given by:

$$I_{total} = \int I_{sur}(t)dt. \tag{5.21}$$

It is equal to:

$$I_{total} = \frac{D}{\pi}\sum_{m=1}^{m=\infty} m\left(\frac{\pi}{d}\right)^2 \sin\frac{2m\pi z_0}{d} \times \frac{1}{D\left(\frac{m\pi}{d}\right)^2 + \frac{c}{l_a}}. \tag{5.22}$$

For media of low absorption ($l_a -> \infty$), this intensity is approximately:

$$I_{total} \approx \frac{1}{2}\left(1 - \frac{2z_0}{d}\right) = \frac{1}{2}\frac{L}{L + 2z_0}. \tag{5.23}$$

This 1/2 factor is due to the fact that the photon source is assumed to be diffuse at the slab boundary z'=z_0. If it is assumed that the photon source becomes diffuse at z'=$2z_0$[10–11] i.e. at a distance z_0 after the physical boundary, the total intensity in the back-scattered direction is:

$$I_{total} = \frac{L}{L + 2z_0} = \frac{L}{L + 1.4208l_t}. \tag{5.24}$$

where z_0=0.7104l_t. We remark that this expression for the total back-scattered intensity is consistent with the calculations of Genack et al.[10–11] if it is assumed that the penetration depth that is the depth after the physical boundary of the slab where the collimated source of photons is effectively randomized(referred to as z_p in [10–11]) is z_0. The total intensity in the transmitted direction becomes $\frac{2z_0}{L+2z_0}$.

This expression shows that over the whole back-scattered surface, for thickness of the slab, L of the order of $2z_0$, the intensity increases as the medium becomes more and more

scattering. For L=60mm, l_t=7mm, the total back-scattered is I_{total}=0.86; For L=60mm, l_t=3mm, I_{total}=0.93 which is an increase of about 8% compared to the total intensity given before for l_t=7mm. It can be seen then that as the transport mean free path of the medium decreases, the transmitted intensity decreases and the backscattered intensity increases slightly for whole surface collection. The increase in the whole surface collection of the back-scattered intensity is mainly due to the light detected close to the source that is not yet in the diffusion region. For point collection of the detected intensity in the diffusion region i.e. S-D>7l_t, both transmitted and back-scattered intensities decrease. The decrease in the point collection in the back-scattered direction is due to the absorption of the medium. As the scattering increases, photon travels longer distances to reach the detector and therefore is absorbed more. Therefore there is no contradiction with energy conservation laws. This derivation shows also that for very large thickness of the slab, the total backscattered intensity is always the same, independent of the transport mean free-path. For completely non-absorbing media, the backscattered intensity is 1 for semi-infinite geometry.

In the diffusion region, two other parameters that can be used to obtain the optical parameters, l_t and l_a, of a random medium are the peak intensity and the risetime defined as the difference between the time at which the intensity reaches 90% of the peak value and the time at which the intensity reaches 10% of the peak value. Figs. 5–11 shows plots of the risetime against the peak intensity for different l_t and different l_a. The theoretical points are obtained from eq. 5.11; the experimental data points are obtained from Fig. 5–7. As the transport mean free path increases, the peak intensity increases and the risetime decreases. For large l_t, the curves of the risetime vs the peak intensity start to

converge meaning that in the non-diffusion region, the risetime and the peak intensity can not uniquely give the optical parameters of the scattering medium. This was to be expected since the diffusion approximation is valid for source-detector separation more than about $7l_t$. If the pulse profile is given, all that one is to do is to find the peak intensity and the risetime and go to these two plots to find uniquely lt and la. For example, from the experimental curve profile in Fig. 5–7a, the peak intensity and the risetime are, Ipeak=0.84×10^{-9} and trise=407ps. Placing this point in the plot, one finds the optical parameters as l_t=2.9mm and l_a=500mm which are pretty close to the reconstructed parameters from diffusion theory of l_t=3mm and l_a=480mm, which is a discrepancy of about 3%. This is a simple way so far to obtain the parameters of a medium. All that is needed is the risetime and the maximum intensity that can be easily found from the profile in question. As stated before, the error in the optical parameters increases as the source-detector separation is decreased below $7l_t$.

This multi-fiber collection system can be used to obtain pulse profiles for a reference medium for possible three-dimensional imaging using only one detector. Only an appropriate theory to calculate the intensity profiles at other positions is needed. Fig. 5–12 shows the transmitted intensities divided by the side-scattered intensities at different times for the three different transport mean free paths from theoretical and experimental data. The ratios are exactly the same for the different scattering media. The equality may be written as follows:

$$\frac{I_{exp}^{trans}(r',t)}{I_{exp}^{side}(r,t)}\Big|_{l_t} = \frac{I_{th}^{trans}(r',t)}{I_{th}^{side}(r,t)}\Big|_{l_t} \tag{5.25}$$

where the subscripts exp and th stand for experimental and theoretical values, respectively.

Fig. 5–13 is the ratio of the forward-scattered to the back-scattered intensity profiles for the different transport mean free paths . The ratios for theory and experiment are the same for early times but different for later times. The fitting looks better as lt becomes smaller. The discrepancy might be due to the fact that the detector in the backscattered direction is close to the corner of the slab. The smallest distance to the corner of the slab is about 4lt. The corner might affect photons arriving at late times, which may be why there is a substantial discrepancy in the ratios at late times. The equality of the ratios may be written as:

$$\frac{I_{exp}^{trans}(r',t)}{I_{exp}^{back}(r,t)}|_{l_t} = \frac{I_{th}^{trans}(r',t)}{I_{th}^{back}(r,t)}|_{l_t} , \tag{5.26}$$

where $\frac{I_{exp}^{trans}(r',t)}{I_{exp}^{back}(r,t)}|_{l_t}$ is the ratio of the forward-scattered to the back-scattered experimental curves in time for a particular scattering medium, and $\frac{I_{th}^{trans}(r',t)}{I_{th}^{back}(r,t)}|_{l_t}$ is the ratio of the forward-scattered to the back-scattered theoretical curves in time for the same scattering medium.

The proportion being valid for any direction, one can generalize by omitting the superscript side, back, or trans in eqs. 5.25 and 5.26 as follows:

$$\frac{I_{exp}(r',t)}{I_{exp}(r,t)}|_{l_t} = \frac{I_{th}(r',t)}{I_{th}(r,t)}|_{l_t} , \tag{5.27}$$

which is equivalent to:

$$I_{exp}(r',t)|_{l_t} = I_{exp}(r,t)\frac{I_{th}(r',t)}{I_{th}(r,t)}|_{l_t} , \tag{5.28}$$

that can be used to "measure" an experimental curve in any direction given one experimental profile in one direction and theoretical algorithms to calculate profiles in any direction. The terms of this equation(eq. 5.28) are interpreted as follows:

$I_{exp}(r', t)$ is the desired experimental value at time t and position r'; $I_{exp}(r, t)$ is an actual experimental measurement value at time t and position r; and

$$\frac{I_{th}(r', t)}{I_{th}(r, t)} \tag{5.29}$$

is the ratio of the theoretical intensities at position r' to those at position r at time t.

5.6 Conclusion

Experimental data and theoretical model confirm that forward-, side-, and back-scattered light exhibit a decrease in peak intensity and the areas under the profiles. It has been expected that when a medium becomes more scattering, the backscattered light intensity would become higher and the transmitted intensity would become lower. This has been now shown not to be correct for the back-scattered signal. Only at certain late arrival times, the backscattered intensity is higher. It has been shown, however that for whole surface collection in the back-scattered direction, the intensity increases as the transport mean free path decreases.

A new method to obtain the transport mean free path of a medium is by finding the risetime and the peak intensity of the scattered pulse profile. There are many transport mean free paths and absorption lengths that correspond to a particular risetime or peak intensity. For a given profile of scattered intensity in the diffusion region, however, there is a common point that corresponds to the risetime and the peak intensity. That point represents the optical parameters of the scattering medium. A large error in the optical parameters in the non-diffusive region is expected.

It has also been showed that any experimental profile can be "measured" by using only one detector at one direction with a suitable theoretical model. This is important

in medical imaging where a reference profile is needed for every detector position. If one detector can be placed at such a position that the hidden object does not influence the collected data, then reference profile can be "measured" for any other detector at any position.

5.7 References

1. See OSA Proceedings on Advances in Optical Imaging and Photon Migration, edited by R. R. Alfano (Optical Society of America, Washington, DC 1994) Vol. 21.

2. See SPIE Proceedings on Photon Migration and Imaging in Random Media and Tissues, edited by B. Chance, R. R. Alfano (SPIE, Washington, DC, 1993) Vol. 1888.

3. See SPIE series on Medical Optical Tomography: Functional Imaging and Monitoring, edited by G. J. Muller (SPIE, Washington, DC, 1993) Vol. IS11.

4. J. J. Dolne, M. Klibanov, F. Liu, S. Gutman, and R. R. Alfano, "Detection of a scattering layer inside a three-layered scattering medium," edited by R. R. Alfano, B. Chance (SPIE, Washington, DC, 1995) Vol. 2389.

5. See ch. 4

6. M. Lax, V. Nayaramamurti, and R. C. Fulton, "Classical diffusive Photon transport in a slab," in Proc. of the Symposium on Laser Optics Of Condensed Matter edited by J. L. Birman, H. Z. Cummings, and A. A. Kaplyanskii (Plenum, New York, 1987), pp. 229–235.

7. M. S. Patterson, B. Chance, and B. C. Wilson, "Time resolved reflectance and transmittance for the non- invasive measurement of tissue optical properties," Appl. Opt. **28**, 2331–2336, 1989.

8. M. S. Patterson, S. Anderson-Engels, B. C. Wilson, and E. K. Osei, "Absorption spectroscopy in tissue-simulating materials: a theoretical and experimental study of photon paths," Appl. Opt. **34**, 22–30, 1995.

9. F. Liu, Ph. D. Thesis, The City University of New York, 1993.

10. J. H. Li, A. A. Lisyansky, T. D. Cheung, D. Livdan, and A. Z. Genack, "Transmission and surface intensity profiles in random media," Europhysics Letters **22**, 675–680, 1993.

11. A. Z. Genack, "Optical transmission in disordered media," Phys. Rev. Lett. **58**, 2043–2046, 1987.

5.8 Figures

Figure 5.1 Diagram of the dipole sources to satisfy the boundary conditions at all times.

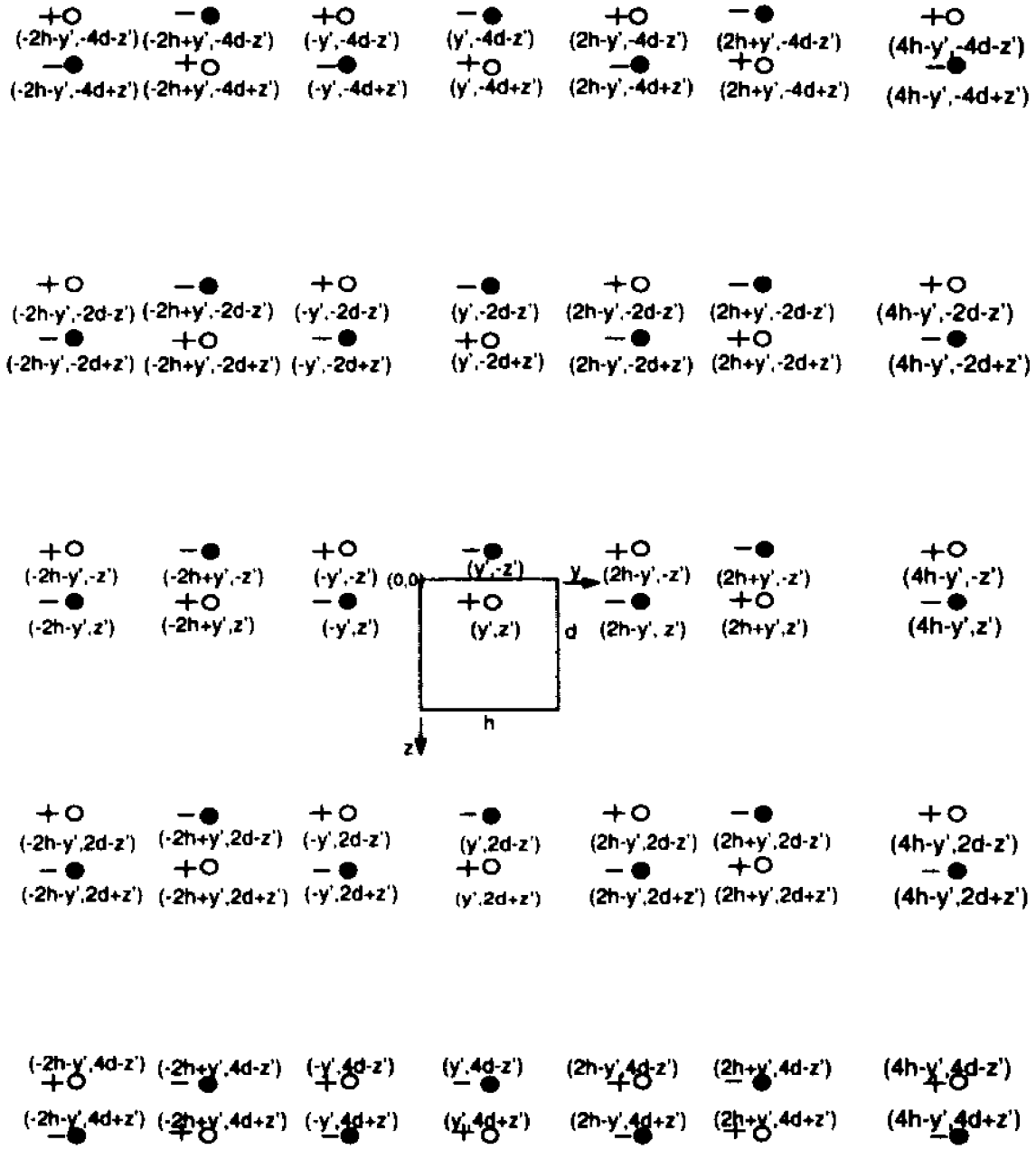

Figure 5.2 A rectangular slab containing scattering particles. The positions of the forward, backward and side detectors are shown.

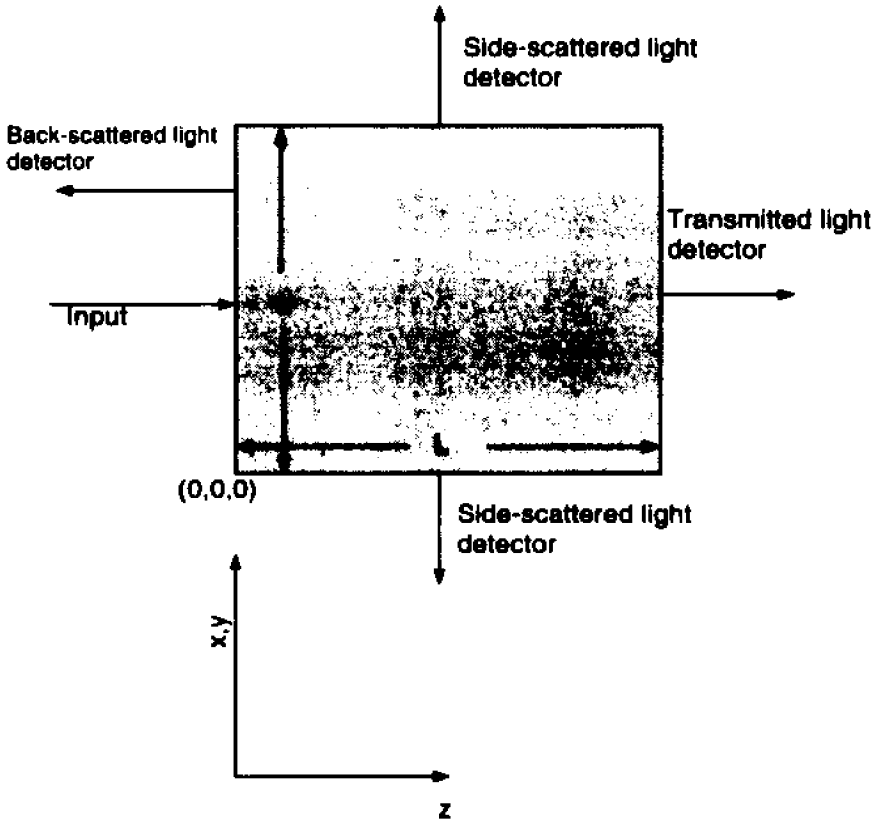

Figure 5.3 Forward scattering light profile computed from diffusion theory for a) lt=3mm, la=400mm, area=17.1 $\times 10^{-7}$ b) lt=2mm, la=400, area=8.6$\times 10^{-7}$ and c) lt=1mm, la=400mm, area=1.82$\times 10^{-7}$ for S-D(y)= 0mm, S-D(z)= 60mm.

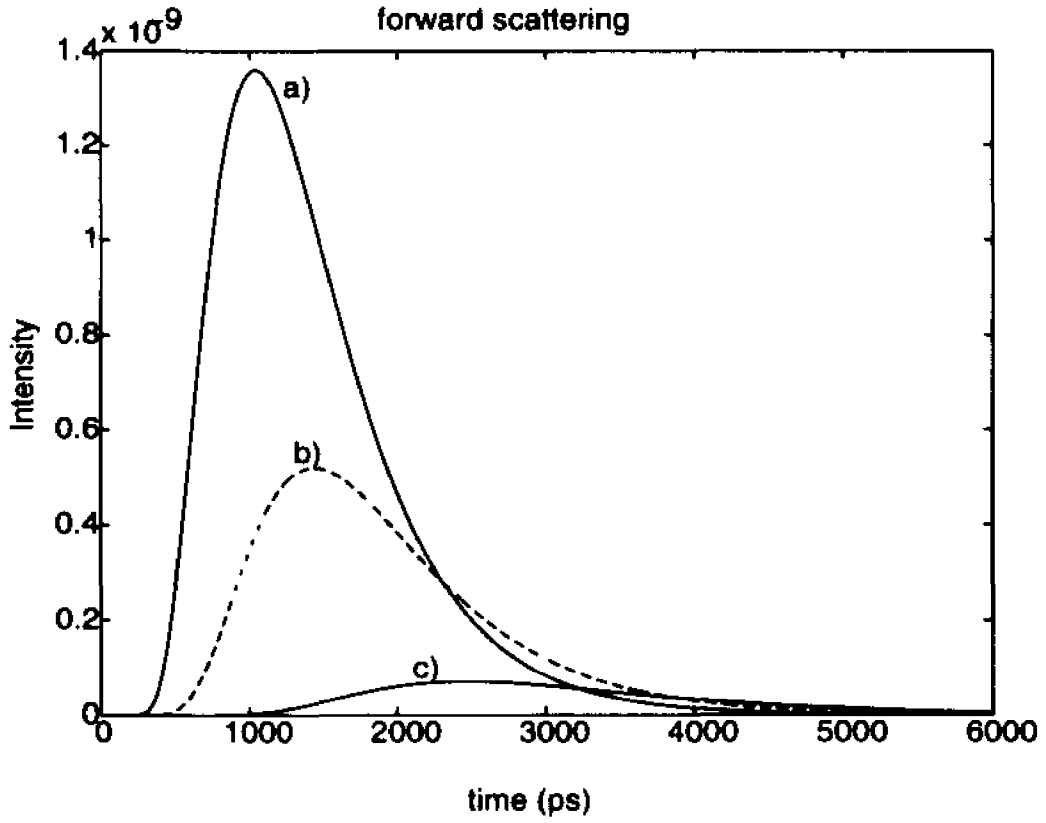

Figure 5.4 Side-scattering intensity profile computed from diffusion theory for a) lt=3mm, la=400mm, area=5.53×10^{-6} b) lt=2mm, la=400mm, area=3.13×10^{-6}, and c) lt=1mm, la=400mm, area=0.91×10^{-6} for S-D(y)=30mm and S-D(z)=30mm.

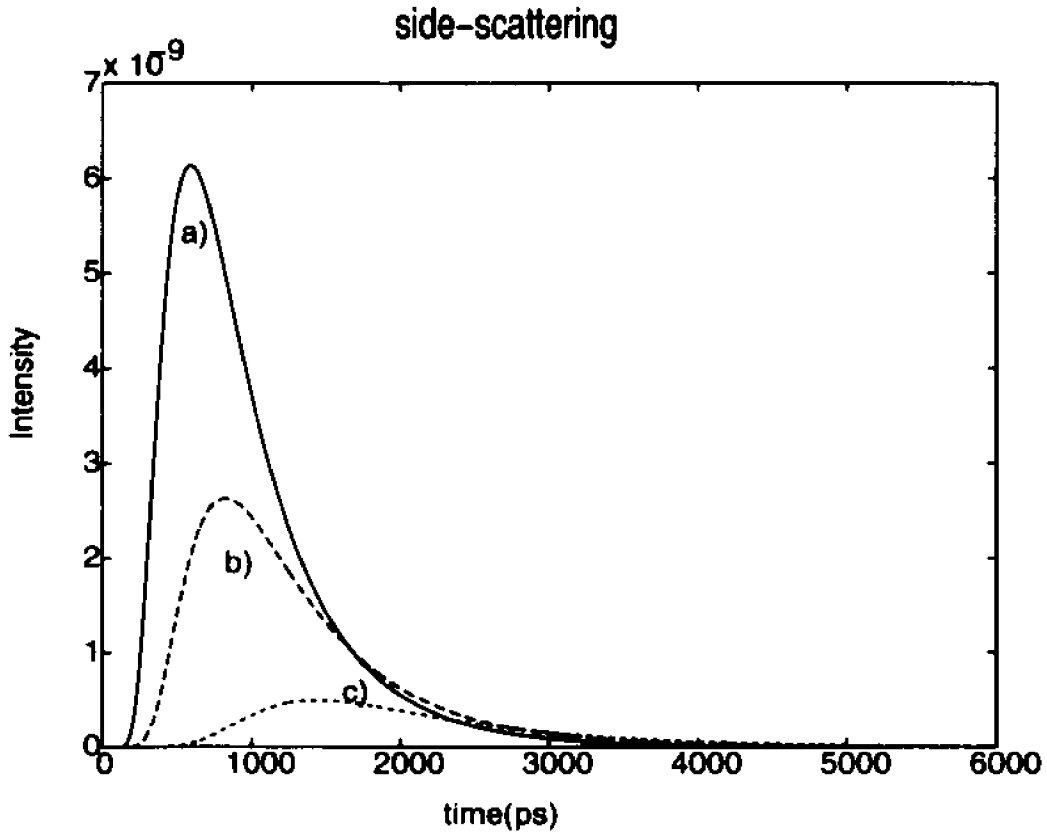

Figure 5.5 Back-scattered intensity profile computed from diffusion theory for a) l_t=3mm, la=400mm, area=11×10^{-6} b) l_t=2mm, la=400mm, area=6.37×10^{-6} and c) l_t=1mm, la=400mm, area=2.19×10^{-6} for S-D(y)=25mm and S-D(z)=0mm.

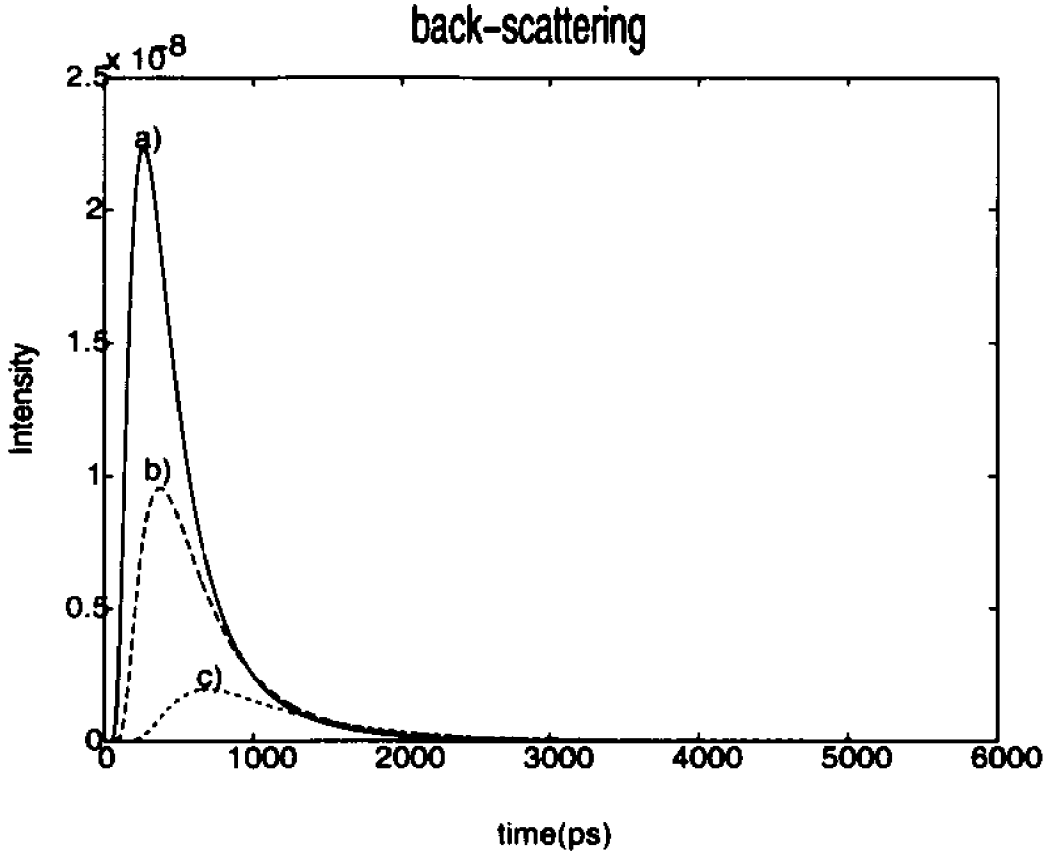

Figure 5.6 Experimental set-up. Multiple detection system uses four optical fibers of the same length. C. F. : Collection fiber

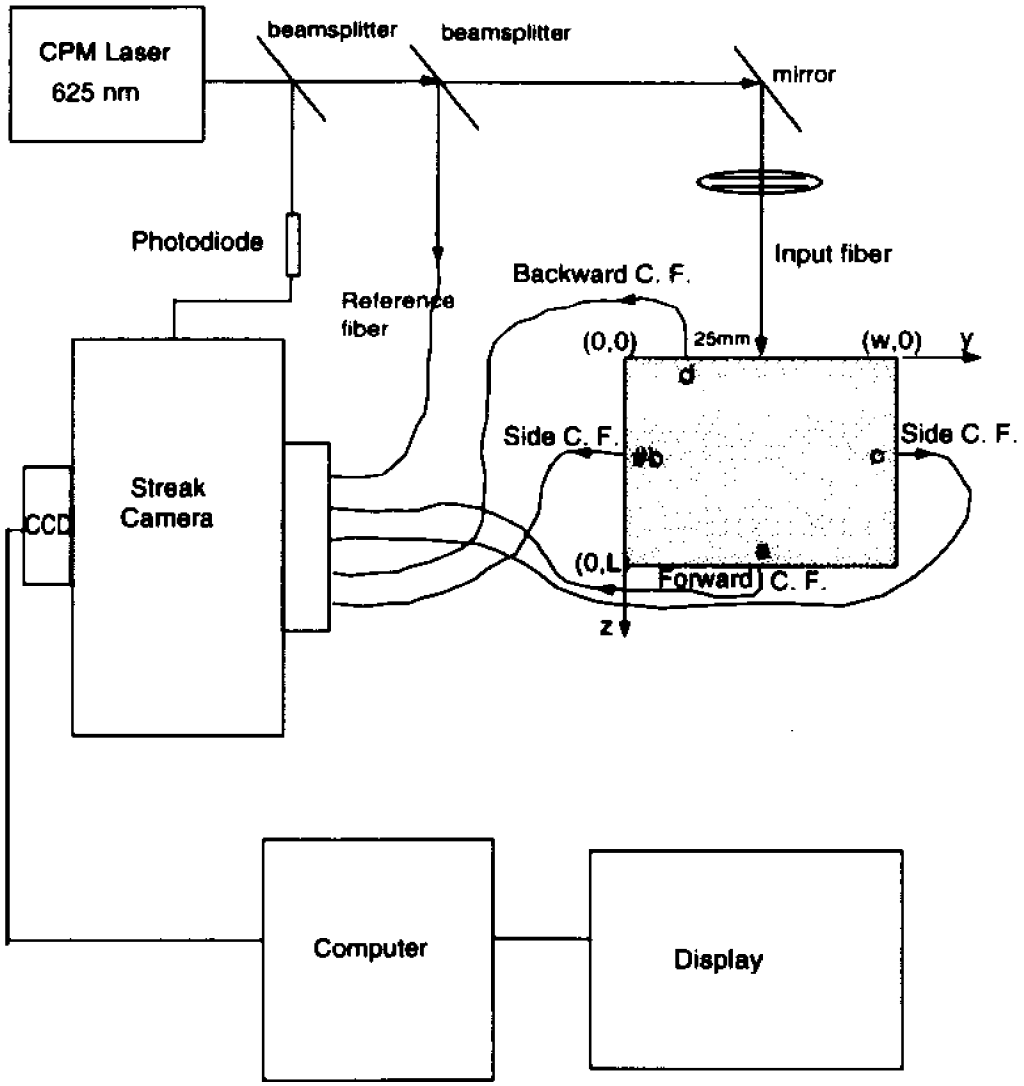

Figure 5.7 Transmitted experimental profiles and diffusion model fittings for a) 2.4% intralipid concentration, lt=3mm, la=480mm, area=1×10^{-6} b) 3.6%, lt=2.1mm, la=492mm, area=0.58×10^{-6} and c) 4.7%, lt=1.7mm, la=559mm, area=0.35×10^{-6} for S-D(y)=0mm and S-D(z)=60mm.

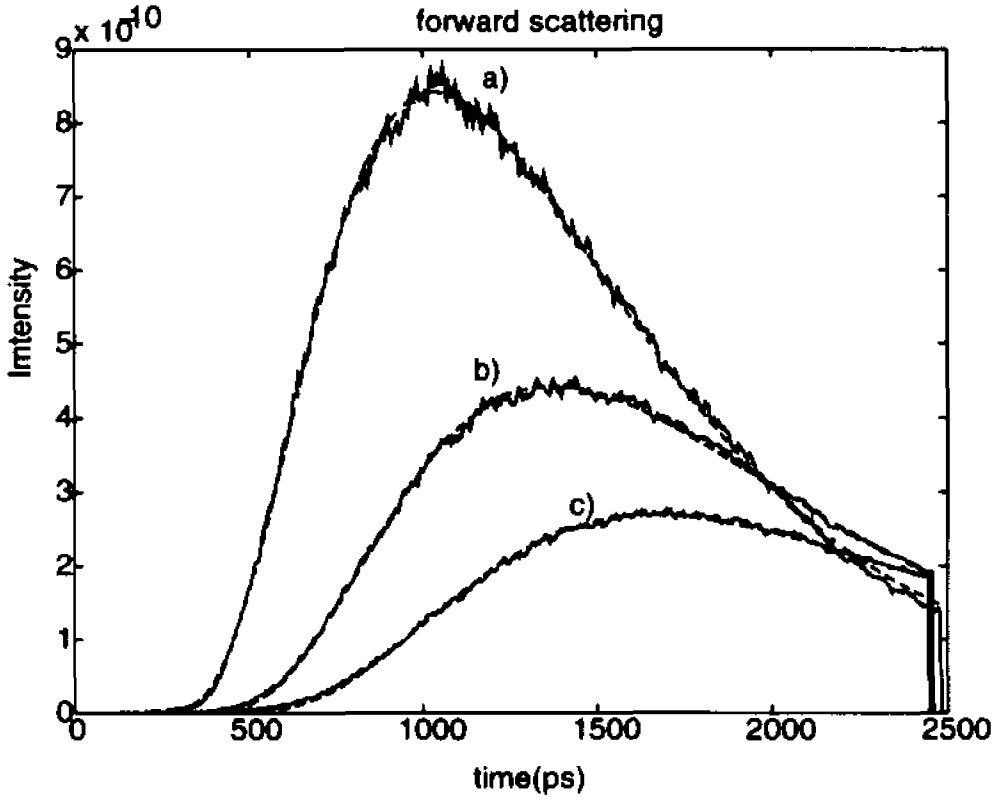

Figure 5.8 Fitting of the transmitted experimental profile given in Fig. 5–7a with the diffusion theory model; a) various transport mean free paths l_t=2.8, 3.1, and 3.2mm besides the best fit of l_t=3mm and a fixed absorption length l_a=480mm are used to fit the experimental data to estimate the error in l_t; b) the error in l_a is estimated by fitting the experimental profile with the diffusion theory computed for l_a=430 and 530mm besides the best fit parameter l_a=480mm and fixed l_t=3mm.

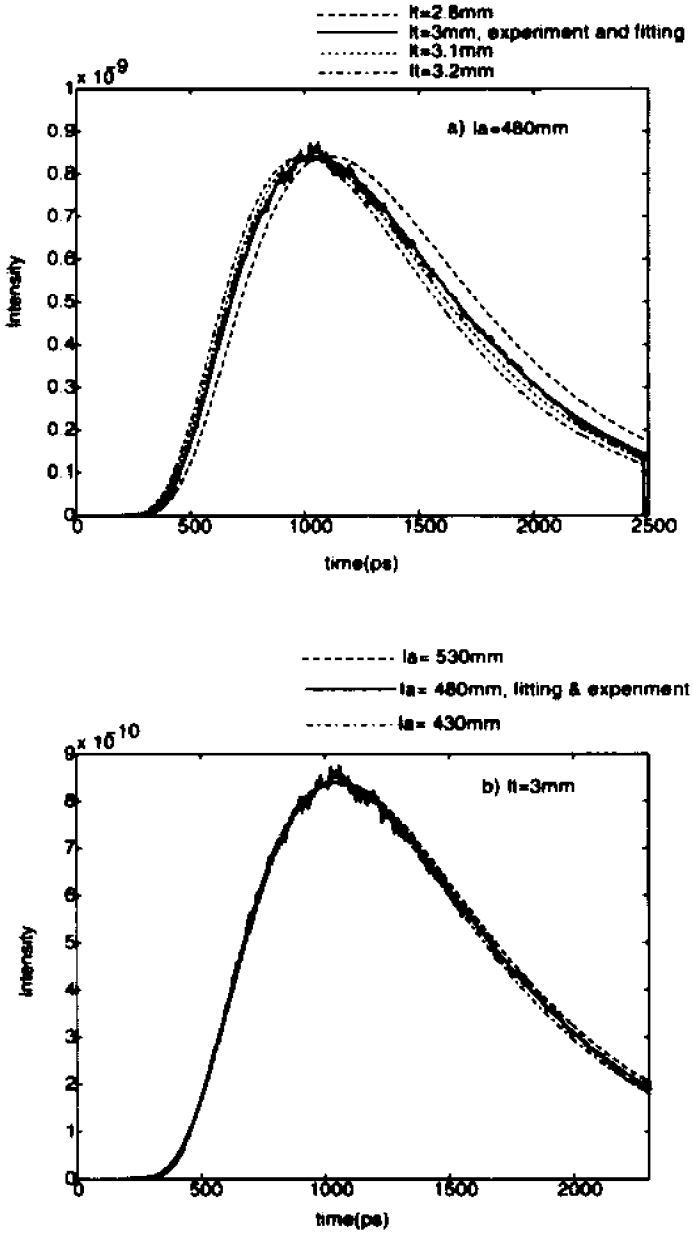

Figure 5.9 Side Scattering experimental profiles and diffusion model fittings for a) 2.4%, lt=2.7mm, la=533mm, area=3×10^{-6} b) 3.6% intralipid concentration, lt=1.9mm, la=479mm, area=2.3×10^{-6} and c) 4.7%, lt=1.5mm, la=487mm, area=1.75×10^{-6} for S-D(y)=30mm and S-D(z)=30mm.

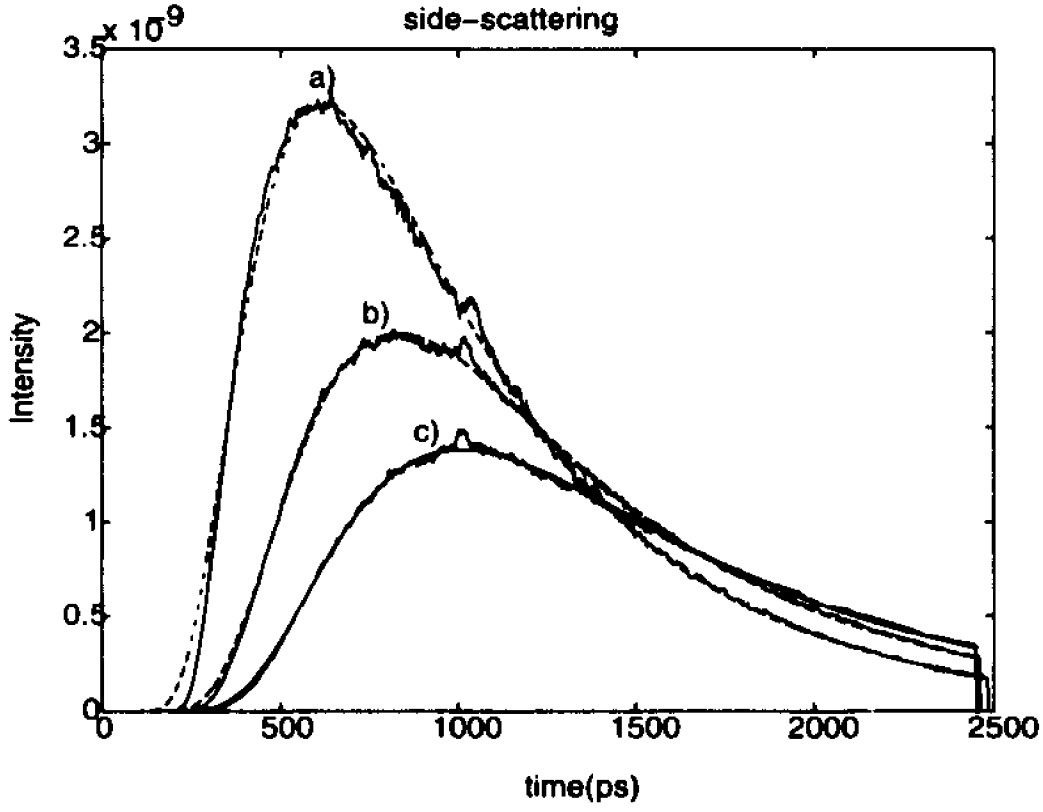

Figure 5.10 Back-scattered intensity profile for a) 2.4% intralipid concentration, lt=3mm, la=480mm, area=4.96×10^{-6} b) 3.6%, lt=2.1mm, la=492mm, area=4.4×10^{-6} and c) 4.7%, lt=1.7mm, la=559mm, area=3.5×10^{-6} for S-D(y)=25mm and S-D(z)=0mm.

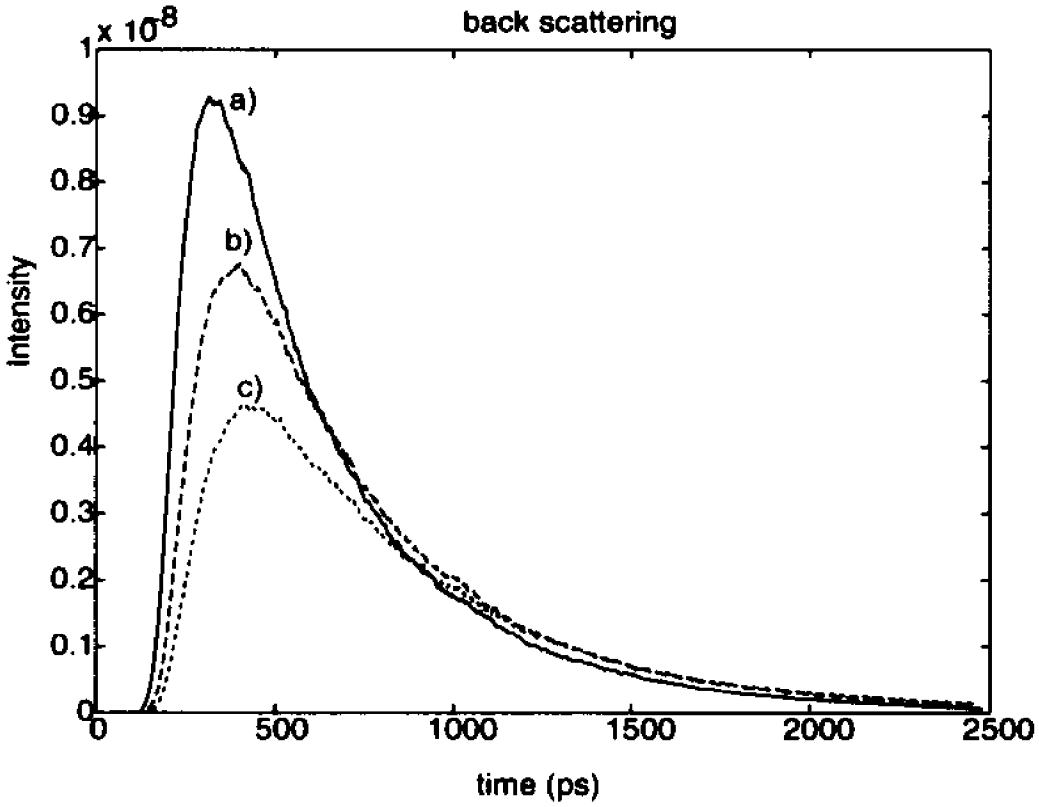

Figure 5.11 Risetime against the peak intensity for the transmitted profiles for different transport mean free paths l_t and absorption lengths l_a. Solid line: theory; Points: experiment.

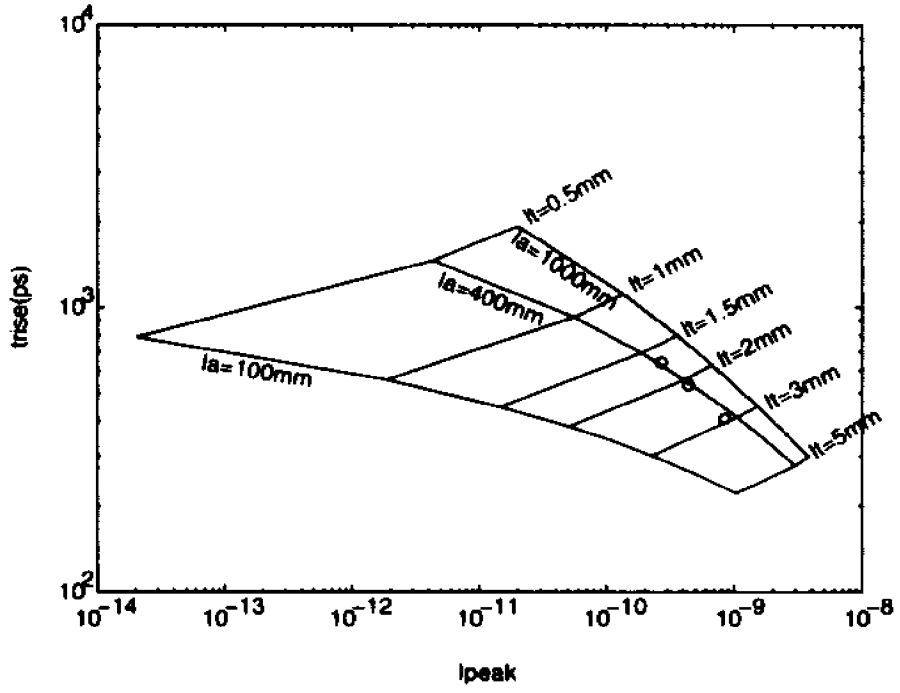

Figure 5.12 Ratio of transmitted to side scattered intensities in time from diffusion(solid) and experiment(broken) for different transport mean free paths.

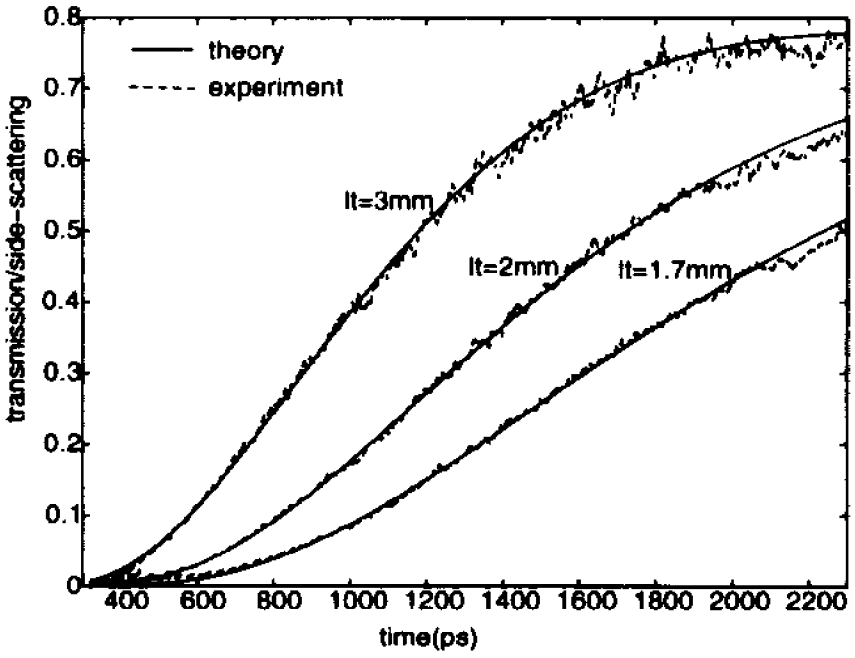

Figure 5.13 Ratio of forward- to back- scattered intensities in time from diffusion(solid) and experiment(broken) for different transport mean free paths.

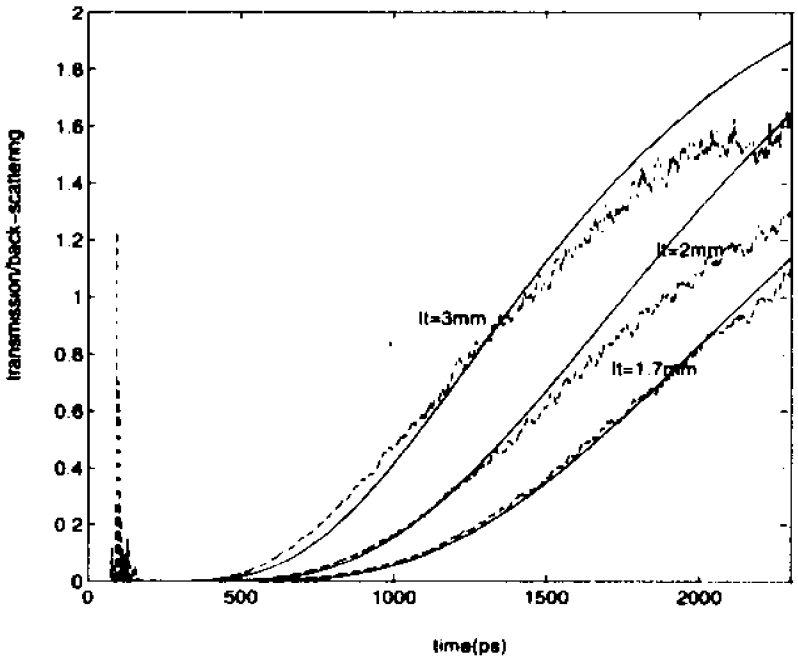

Chapter 6

The angular dependence of backscattered light intensity profile

6.1 Introduction

Over the past decade, diverse research projects have been oriented toward studying the light back-scattered from a random medium[1–6]. The application of light back-scattered has been extended from a determination of the optical properties such as the transport mean free path and the absorption length to the imaging of hidden objects inside the scattering medium. In 1975, Reynolds et al.[1] used back-scattered light to determine the oxygen content in blood. In 1979, Shimizu et al.[2] used the back-scattered light to determine the optical properties of scattering media such as tissue. Recently, Welch et al.[3–4] used reflectance measurements to obtain the difference in the optical properties of normal egg white and coagulated egg white. Das et al.[5] and Yoo et al.[6] determined the transport mean free path and the absorption length of cancerous and benign breast tissues using the back-scattered light. Feng et al.[7]used theoretical back-scattered data to reconstruct an absorber imbedded inside a scattering medium. Light back-scattered from a random medium has the advantage of non-invasively probing the interior of the medium[8] such as the breast. Unlike the transmitted signal, the back-scattered detected signal is not limited by how much the breast can be compressed; some signal can always be obtained in the back-scattering direction by adjusting the detector. While a substantial amount of work has been accomplished using the reflectance geometry, these works have been performed by placing the detector perpendicularly to the surface of the scattering medium. In a recent study[9–10], it has been shown, using the back-scattered signal, that

there may exist most favorable photon paths along and near by which most of photons propagate. These photon paths have been shown to be time and angle dependent.

In this chapter, we will show that there is a strong angular dependence to the temporal behavior of the back-scattered light in the non-diffusive region. The profiles were measured using an ultrashort laser system and picosecond resolution streak camera system. This angular dependence of the back-scattered light indicates that there may be well defined photon paths between the source and the detector. By substracting the effect of the diffuse photons, we will determine the fraction of photons that travel along well defined paths.

6.2 Experimental methods

The experimental geometry to demonstrate the angular dependence of the back-scattered intensity profile is shown in Fig. 6–1. A colliding pulse mode-locked (CPM) laser is used to produce ultrashort pulses of 100fs FWHM at a repetition rate of 82MHz and a wavelength of 625nm. The average power of the laser beam is 10mW. The pulses from the mode-locked laser are divided in three parts: one small part goes into a fast photodiode that triggers the streak camera, another part goes into the streak camera and is used as a reference to mark the arrival time of the pulse, and the main part of the beam is coupled through a lens to the input side of an optical fiber used as the source. This fiber has a core diameter of 200 μm and a divergence angle of 5degrees (FWHM). This small divergence of the optical fiber is designed by placing a small self-focusing lens at the end of the delivery fiber. The tip of this optical fiber is inserted 1mm below the surface of an intralipid suspension. The intralipid is contained inside a rectangular plastic cell (10cm width x 10cm length x 13cm height). The intralipid reaches a height of 11cm.

Two different concentrations are used in this experiment; the first one is obtained by adding 7.6ml of the stock (the stock is 10%) to 1100ml of distilled water. The transport mean free path for this concentration is l_t=9.3mm. The other concentration is obtained by adding 30.6ml of the stock to 1100ml of water for a transport mean free path l_t=2.3mm. An optical fiber detector of 400μm core diameter with collection angle of about 10degrees is placed 40mm (R=S-D=40mm) from the source fiber in the back scattered direction. This fiber is mounted on a rotational stage so that the angular dependence of the scattered light can be measured. When the fiber detector is oriented parallel to the source fiber and perpendicular to the medium surface, the angle of collection is referred to as 0 degree. When the orientation of the fiber detector is tilted away from the source, the angle of collection is positive and when the orientation is tilted toward the source, the angle of collection is negative as shown in Fig. 6–1. It should be noted that the tip of the fiber detector is always at the same point. The streak camera and CCD systems time resolve and display the signal on the video monitor.

6.3 Results

Experiments have been performed to determine the angular dependence of scattered light profile in the backward direction. The absolute intensities represent the fraction of photons detected for one photon incident on the scattering medium. Fig. 6–2 shows the absolute detected intensity profiles in time for l_t=9.3mm for three different orientations of the fiber detector: 0, –25, and 45 degrees. The dependence of the detected scattered signal on angle is clear. The more the detector fiber is oriented away from the source, the more the detected signal and the earlier the intensity peak arrives. The later portions of all the curves, beyond 750ps, are about the same. These late arriving photons represent

the diffuse signal for this source detector separation. The early part of the signal has some diffuse signal but this diffuse signal which can arrive only after travelling $7l_t$ however, is superimposed on some amount of snake signal that has travelled about the same distance with less scattering. In this geometry, the source to detector distance is about $4.3l_t$ which is not yet in the diffusion region for the early arriving photons. One can observe the broadening in the pulse profile as the detector is turned from 45 to –25 degrees. Such broadening is a direct consequence of the low amount of snake light and more diffuse like light(the photons are randomized) that enter the detector at –25 degrees. Also at that orientation of the detector, the signal is more evenly distributed in time.

Fig. 6–3a displays the detected intensities for l_t=2.3mm for detection angles of 0, –25, and 60 degrees. There is a small difference between the detected intensities at angles 0 and –25 degrees around the peak time 750ps. The scattered signal intensities detected at angles 0 and 60 degrees are about the same. This source to detector distance is about $17l_t$ which is in the diffusion region even for early photons . In other words for this configuration, diffuse photons can (but do not have to) arrive early. The early photons that are snake-like are few. The majority of photons detected are diffuse. Therefore, the orientation of the detector does not make much difference in the detected signal. The profiles for detector orientations of 0 and –25 degrees fitted with the same version of the diffusion theory are shown in Fig. 6–3b. The transport mean free paths are found to be 2.38mm and 2.32 for 0 and –25 degrees, respectively. These parameters match closely the experimental value of the transport mean free path of 2.32mm.

6.4 Discussion

Fig. 6–2 has shown an increase in the absolute detected intensity as the fiber detector

is oriented away from the source. The early part of the detected signals up to about 750ps at 45 degrees is larger than that at 0 and –25 degrees. The difference in the detected intensities due to the orientation of the fiber detector is showed in Fig. 6–4a where the intensity profile for the fiber detector oriented at –25degrees is substracted from the intensity profiles for the fiber detector at –15, 0, and 45degrees for l_t=9.3mm. The peak of the intensity difference reaches about 3.4×10^{-8} for the fiber detector oriented at ang=45degrees, drops to about 1.1×10^{-8} for ang=0degrees, and to about 0.3×10^{-8} for ang =-15degrees. The larger value of the intensity difference is due to snake photons entering the detector as it is turned towards positive orientations. For the higher concentration l_t=2.3mm(R=S-D=17l_t), however, the difference between the detected intensities is very low as shown in Fig. 6–4b drawn to the same scale as Fig. 6–4a for comparison. This small difference means that the orientation of the detector does not make a lot of difference in the diffusion region.

The maximum detected intensities are explicitly plotted in Fig. 6–5a for l_t=9.3mm for the different orientations of the fiber detector. The peak intensities are the same from –25 to –15 degrees detector orientations meaning that the snake light does not influence the detector reading when the detector has a negative orientation. As soon as the detector is turned to 0 degree, the peak intensity increases by about 35%. From 0 to 15 degrees fiber orientation, the peak intensity increases by about 26%. The peak intensity keeps increasing at the same rate as the detector is turned toward 45 degrees. The peak intensities for l_t=2.32mm remain basically the same for the different angles of orientation of the detector as shown in Fig. 6–5b indicating that the scattered intensity profile has little angular dependence in the diffusion region.

The difference that the snake photons make can be studied further by plotting the risetime against the angles of orientation of the optical fiber detector (Fig. 6–6). For the fiber oriented at –25 and –15 degrees, the risetime is about the same. There is a steep decrease of the risetime as the angle is varied from –15 to +15 degrees. The risetime keeps decreasing as the detector orientation is increased to 45 degrees. The region from –15 to 45 degrees is where the snake photons make the most difference.

Fig. 6–7 represents the plot of the time where the intensity is maximum against the angle of detection. The peak time moves earlier as the angle of detection becomes more and more positive. Such is again a direct consequence of the non–diffusive photons that become more and more intense close to the surface of the medium for this geometry.

These observations show that for l_t=9.3mm the snake signal contribution to the detected signal is negligible when the detector has negative orientation. Only a small amount of snake light turns around to enter the detector when oriented at a negative angle. The reason is that is very unlikely for a photon to leave the source, scatter only a few times, pass the detector location, and scatter back to enter the detector oriented at a negative angle as shown in Fig. 6–1 and not be diffuse. To enter the detector, the last scattering of the photon must be such that the angle the direction of the last scattering makes with the normal to the detector is within the acceptance angle of the detector.

The fraction(relative difference) of the snake photons that travel along well-defined paths can be obtained by substracting and dividing by the effect of the diffuse photons. The relative difference gives a better understanding about the photons that are not diffuse compared to the simple difference. The relative difference compares the difference at a time to the number of photons detected at that time. For l_t=9.3mm, the detector oriented at

angle=-25degrees collects mostly diffuse photons. Fig. 6–8a shows the relative difference of the snake photons for l_t=9.3mm. The peak is about 4 for angle=45degrees meaning that the non-diffuse photons is about 5 times as much as the photons that are for the most part randomized. The peak falls to about 1 for angle=0degrees and to 0.3 for angle=-15degrees. The large value of the peak of the relative difference at angle=45degrees indicates that the paths of photons are very intense below the surface of the scattering medium for this geometry. As the orientation of the detector turns to 0 and to −15 degrees, the paths of photons become more and more randomized as indicated by the decrease in the peak of the relative difference. Fig. 6–8b shows the relative difference of the snake photons for l_t=2.32mm. The relative difference is almost zero for the various orientations of the fiber detector indicating that there is no particular group of photons that travel well-defined paths for this concentration of the scattering medium.

6.5 Conclusion

It has been shown that there exist some well-defined angular dependence of photons in the non-diffuse region. The orientation of the detector in detecting the paths is shown to matter mostly in non-diffusive region. This shows that some photons may travel along well-defined paths(Fermat paths). These paths have been shown to be very intense for photons that are the least randomized. But, in the diffusive region($R>7l_t$), the detected intensities are about the same independent of detector direction which can mean that the paths are not as well defined. The detected intensity is completely randomized in the diffusion region. This is why there is no clearly well-defined photon path by varying the angle of detection in the diffusion region. This is important for imaging with different angles. If one desires the intensity profile for a certain solid angle about a certain point,

one can just multiply the detected intensity at that point by that solid angle. Knowing that the intensity has no angle dependence, one can assume that the weight functions used in several inverse reconstruction algorithms are the same regardless of angles.

6.6 References

1. L. Reynolds, "Optical diffuse reflectance and transmittance from an anisotropically scattering finite blood medium," Ph. D. Dissertation, Seattle, 1975.

2. K. Shimizu, A. Ishimaru, L. Reynolds, and A. P. Bruckner, "Backscattering of a picosecond pulse from densely distributed scatterers," Appl. Opt. **18**, pp3484, 1979.

3. M. R. Jerath, D. Kaisig, H. G. Rylander III, and A. J. Welch, "Reflectance feedback control of photocoagulation in vivo," Arch. Ophthalmol., **111**, pp. 531–534, 1993.

4. M. R. Jerath, D. Kaisig, H. G. Rylander III, and A. J. Welch, "Calibrated real time control of lesion size based on reflectance images," Appl. Opt. **32**, pp. 1200–1209, 1993.

5. B. B. Das, Ph. D. Thesis, The City Univ. of New York, 1993.

6. K. M. Yoo, Ph. D. Thesis, The City Univ. of New York, 1990.

7. S. Feng, F. Zeng, and B. Chance, "Perturbation theory of photon migration in the presence of a single defect," OSA Proceedings in Optical Imaging and Photon Migration, R. R. Alfano, ed. (Optical Society of America, Washington, DC, 1994) Vol. 21, pp. 217–228.

8. See SPIE series on Medical Optical Tomography: Functional Imaging and Monitoring, edited by G. J. Muller (SPIE, Washington, DC, 1993) Vol. IS11.

9. A. Ya. Polishchuk and R. R. Alfano, "Fermat photons in turbid media: An exact analytic solution for most favorable paths- a step towards optical tomography," submitted to Phys. Rev. Lett.

6.7 Figures

Figure 6.1 Geometry for the scattering light experiment at different angles of orientation of the detector. R=S-D=40mm.

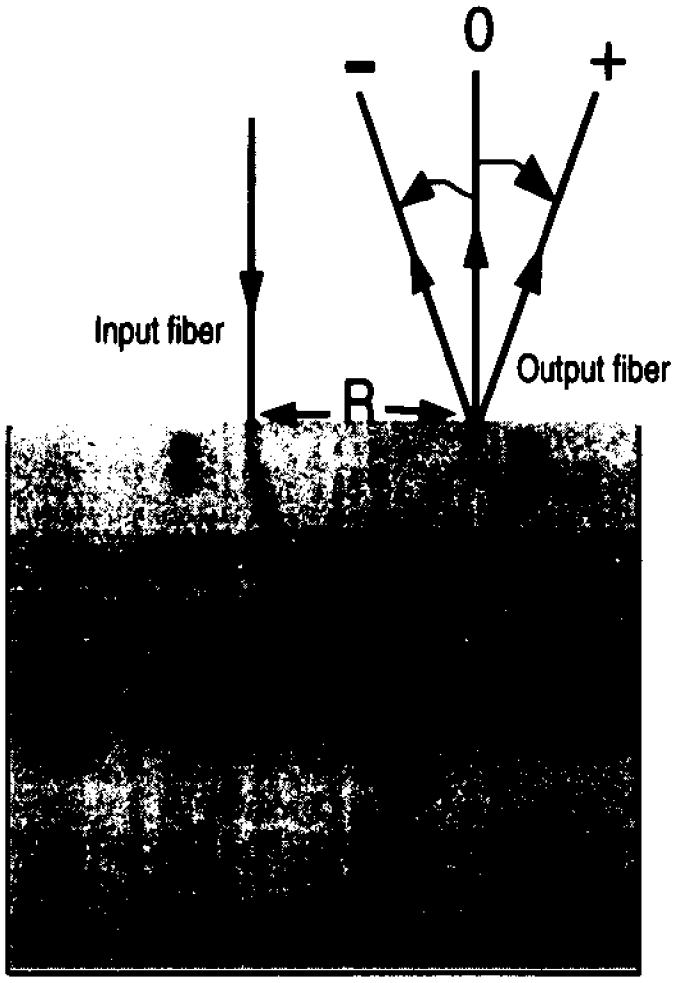

Figure 6.2 Back-scattered intensity profiles from intralipid suspensions for different orientations of the fiber detector for a source detector separation of 40mm. R=S-D=4.3l_t.

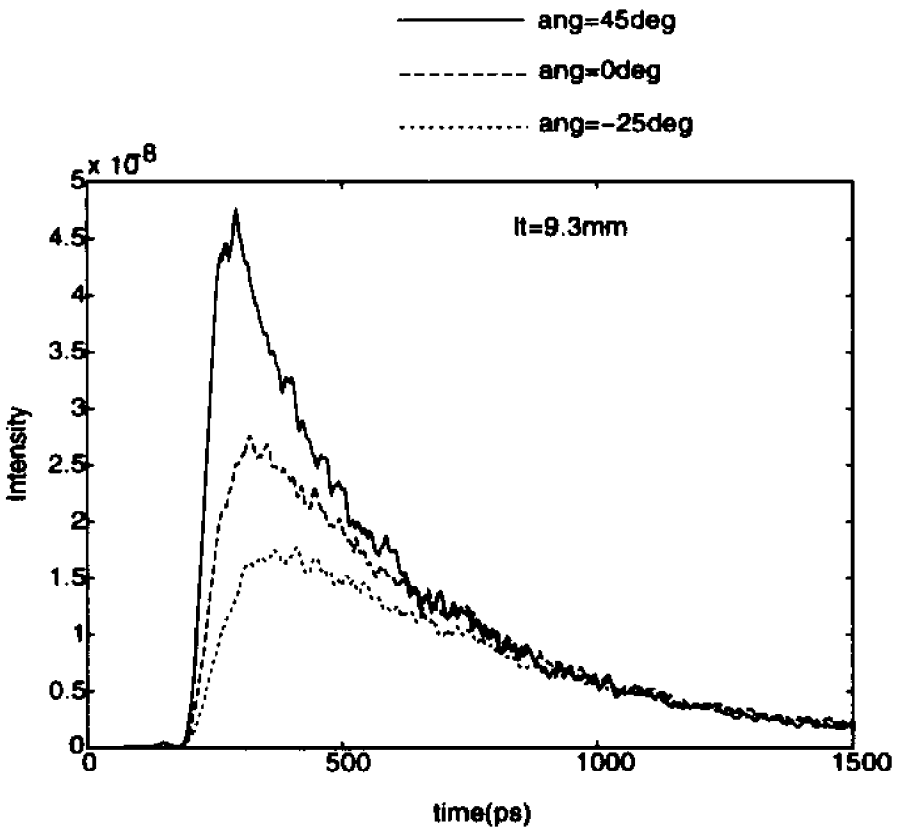

Figure 6.3 a)Back-scattered intensity profiles from intralipid suspensions for different orientations of the fiber detector; b) Fitting of a) with diffusion theory. The source detector separation is 40mm. R=S-D=17.2l$_t$

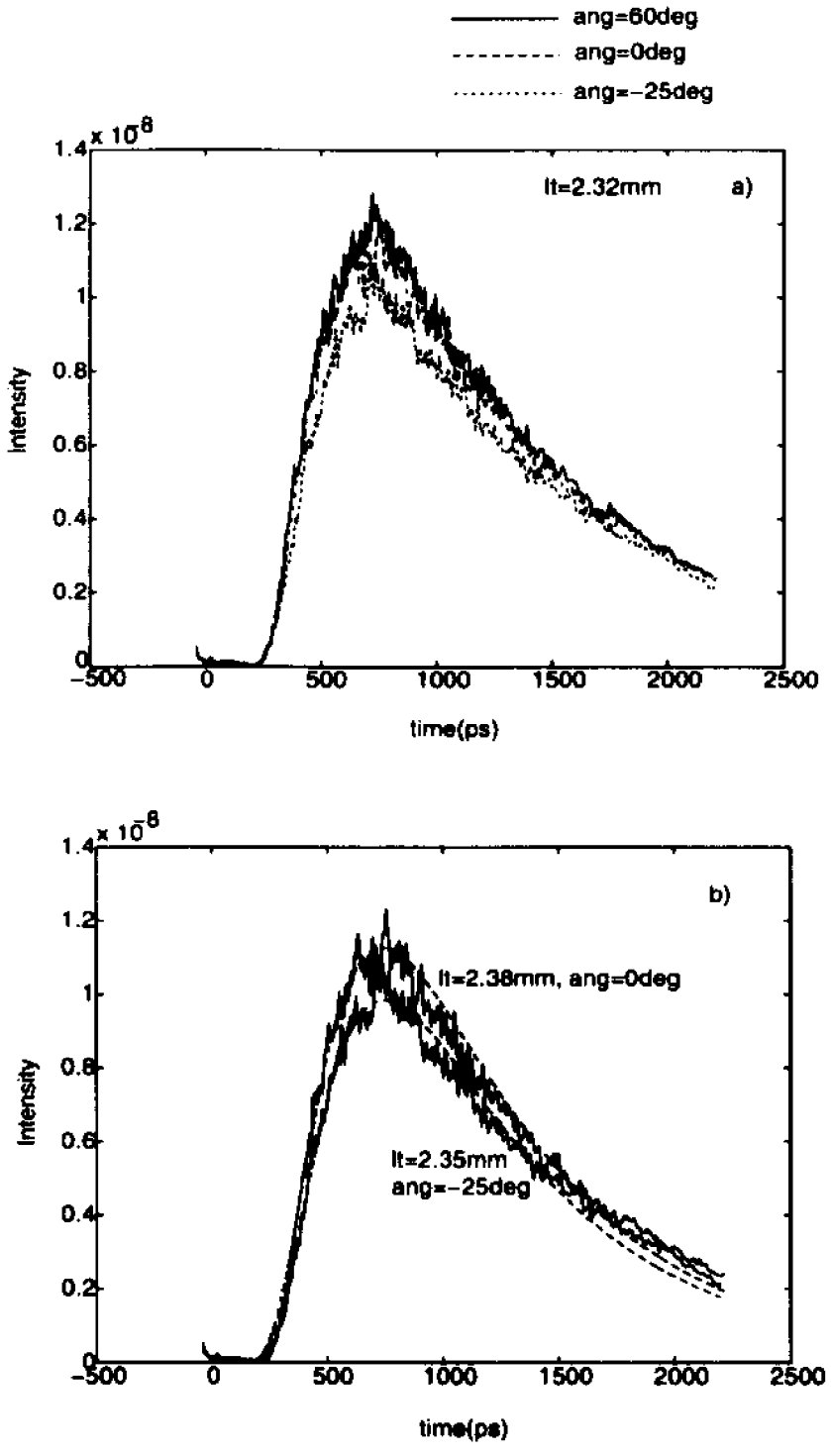

Figure 6.4 The difference of photons detected at a certain angle with respect to the detected photons at detector orientation of ang=-25degrees for a) l_t=9.3mm and b) l_t=2.32mm. The two figures are drawn to the same scale for comparison. The source detector separation is 40mm.

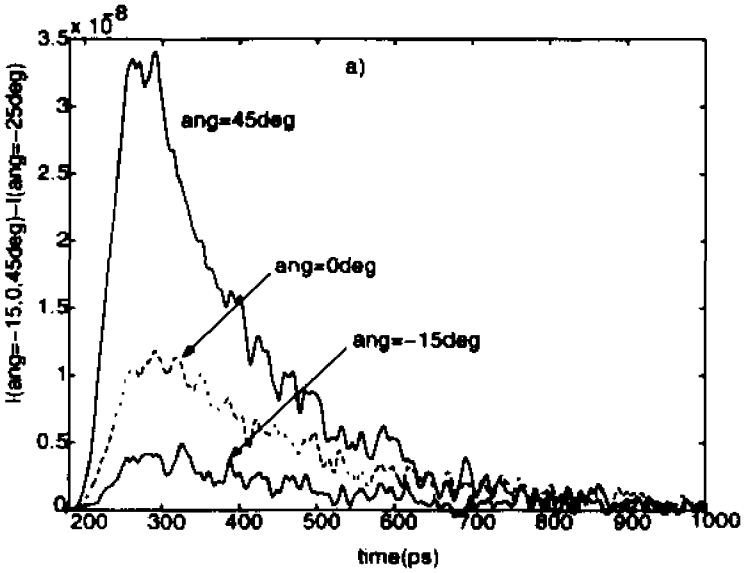

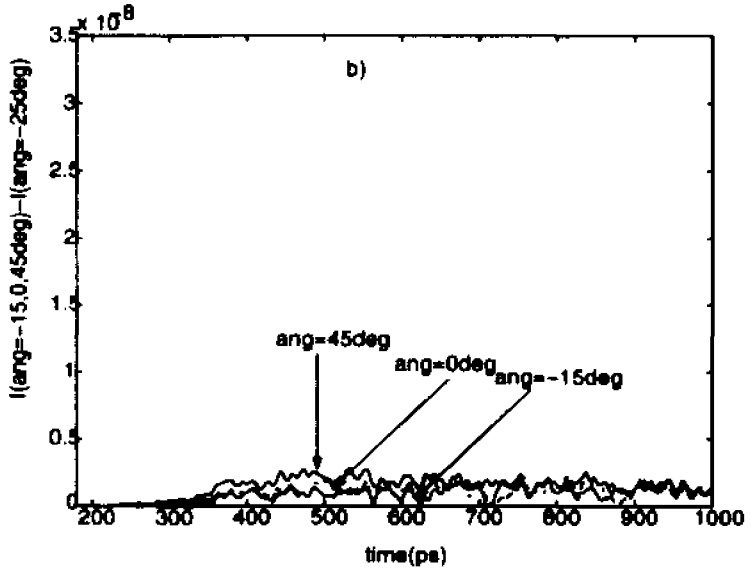

Figure 6.5 The peak intensity for different angles of orientation of the detector for a) l_t=9.3mm, b) lt=2.32mm and S-D=R=40mm.

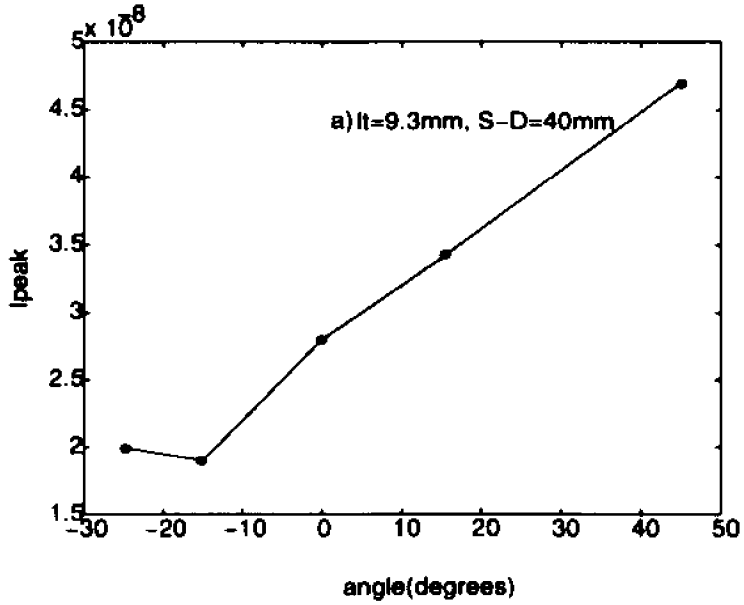

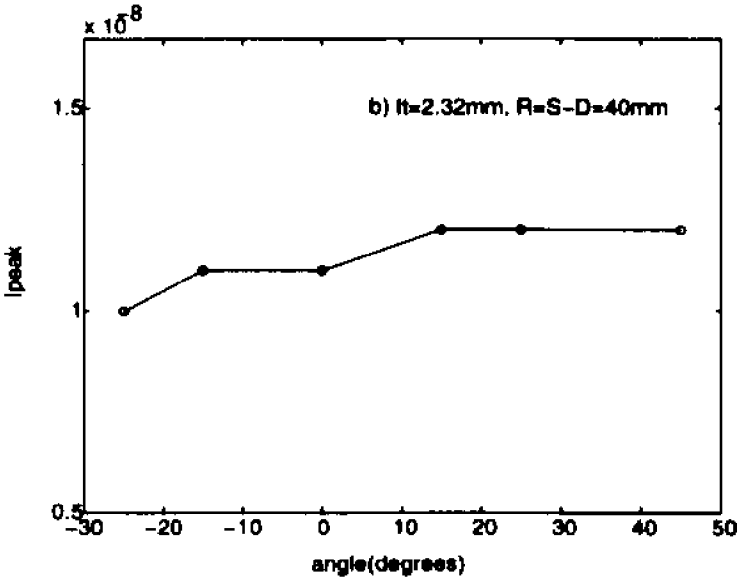

Figure 6.6 The risetime for different angles of orientation of the detector for l_t=9.3mm and S-D=R=40mm.

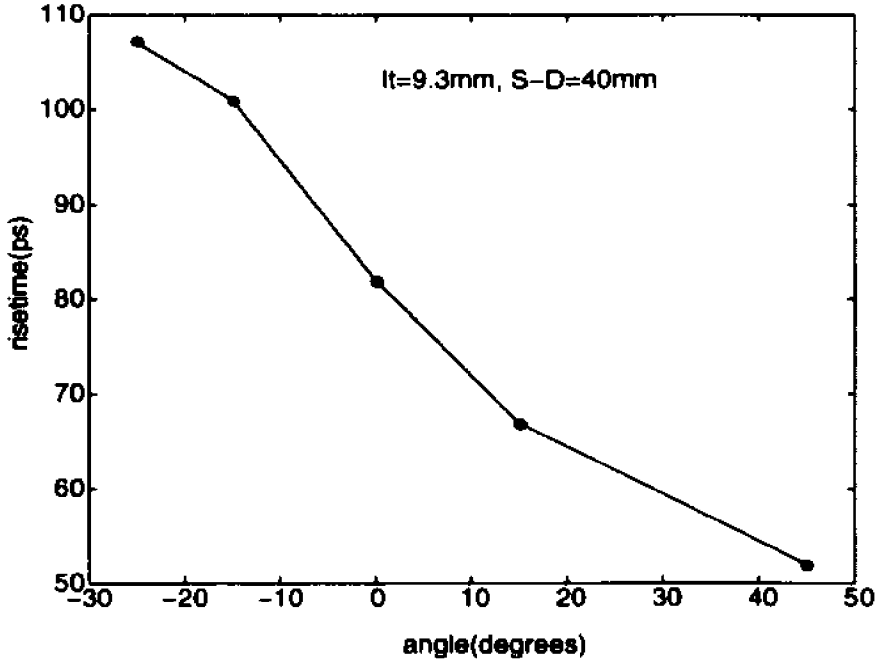

Figure 6.7 The peak time against the different angles of orientation of the detector for l_t=9.3mm and S-D=R=40mm.

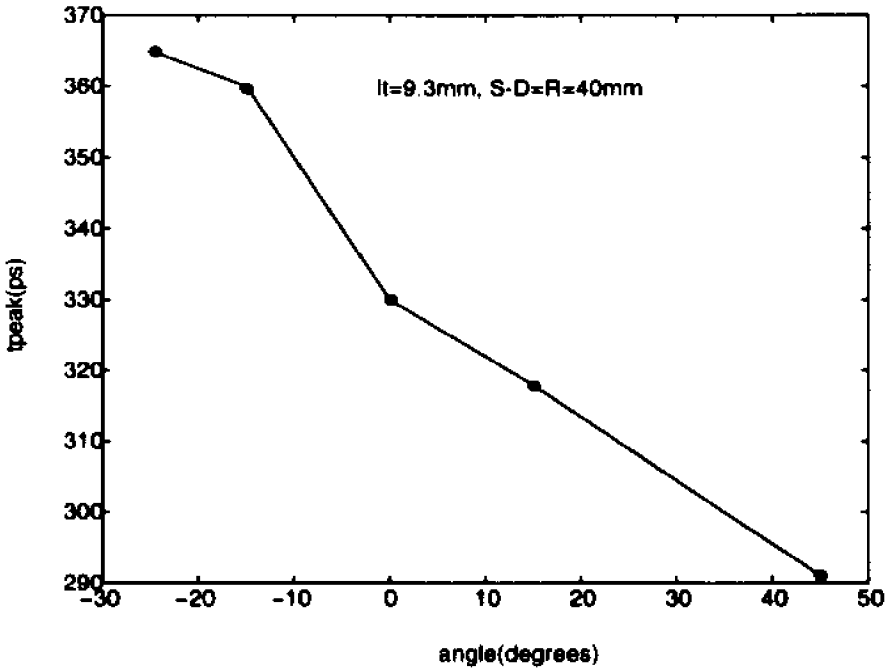

Figure 6.8 The relative difference of photons detected at a certain angle with respect to the detected photons at detector orientation of ang=-25degrees for a) l_t=9.3mm and b) l_t=2.32mm. The source detector separation is 40mm.

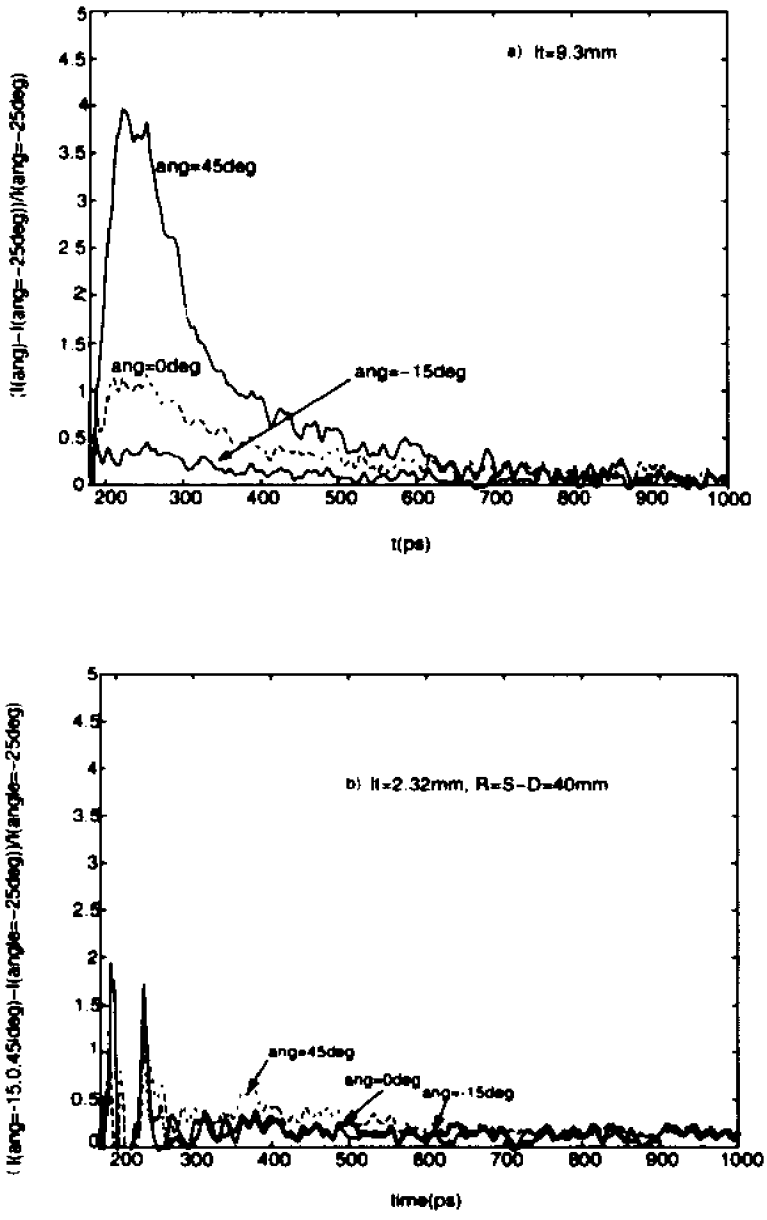

Chapter 7

Photon paths in highly forward scattering media

7.1 Introduction

In the previous chapter on angular dependence of intensity profile, the strong angular dependence of the back-scattered light suggests the existence of special photon paths. Studies on photon paths have been undertaken by several research groups[1-5]. In 1991, Cui et al.[1] used a light shielding plate with a hole inside to study the probability distribution of photons emitted from a surface. In 1993, Grandjbakhche et al.[2] used Monte Carlo simulations to study the photon path-length distributions through optically turbid media. Recently, Perelman et al.[3] have used the path integral approach to show that photons travelling in random scattering media follow well-defined paths. Polishchuk and Alfano[4-5] calculated the most favorable photon paths on the basis of Generalized Fermat Principle for highly forward scattering media. They showed that the Fermat paths have the largest probability even though some other paths may have the same lengths and tangents at the source and detector points.

Each detected photon follows a trajectory starting at the source and ending at the detector. There are groups of photons that travel along unique trajectories. One group of photons follows the ballistic path. The ballistic path is determined by the straight line joining the source and the detector and is given by $I_b = I_{0\ell}^{-(\frac{1}{l_s}+\frac{1}{l_a})L}$, where I_0 is the input energy, l_s, the scattering length, and l_a, the absorption length. This group of photons has been used intensely by different research groups to project a shadow of the target object on the detector[6-7]. For highly scattering media, the ballistic signal is extremely

low or non-existent. To use as much of the detected signal as possible, researchers at various groups have developed reconstruction algorithms for the diffuse signal [8-11] that goes all over the medium. Although plenty of signal is available using this method, the best resolution that one can achieve is about $5l_t$. An alternative way of imaging is to use the snake photons that are detected after the ballistic signal. The snake photon region is between the ballistic and diffuse regions. The snake component for media whose transport length is much less than the absorption length ($l_t << l_a$) is given by[11] $I_s = I_0 A(\Delta t) e^{-b(\Delta t) L / l_t}$. This non-diffusion region where the photons are not totally randomized has the resolution advantage of the ballistic region and the signal advantage of the diffuse region. In this region, some photons travel along well defined trajectories. In the previous chapter, we have showed that snake photons make a lot of difference depending on the orientation of the fiber detector. This region can not be described, however, by neither Beer's law that is used for the ballistic signal, nor by the diffusion equation that is used for the diffuse signal. A theoretical model that can describe this region is not yet available.

In this chapter, we will show the existence of certain photons that travel along well-defined trajectories and that arrive at specific times at the detector. These photons referred to as "Fermat photons" by Polishchuk and Alfano[4-5] visit different depths inside the scattering medium and can be probed by analyzing the detected signal at different times and at different angles This work shows that the Fermat photons may be able to pinpoint the location of a foreign object inside the scattering medium by using the non-diffuse portion of the detected radiation.

This chapter presents the work performed to determine whether well-defined Fermat

photon paths exist by using an ultrashort colliding pulse mode-locked laser and an ultrafast synchroscan streak camera. The angular dependence of photon paths and the dependence of the scattered light from media of different anisotropy factors will be studied. The scattering medium used closely simulates the anisotropy factor g, about 0.9, of real human tissues.

7.2 Experimental Methods

The experimental set-up is shown in Fig. 7–1. A colliding pulse mode-locked (CPM) laser is used to produce ultrashort pulses of 100fs FWHM at a repetition rate of 82MHz and a wavelength of 625nm. The average power is 10mW. The laser pulses are divided in three parts: one small part goes into a fast photodiode that triggers the streak camera, another part goes into the streak camera and is used as a reference to mark the arrival time of the pulse, and the main part of the beam is coupled through a lens to the input side of an optical fiber used as the source. This fiber has a core diameter of 200 μm and a divergence angle of 5degrees (FWHM). This small divergence of the optical fiber is possible because of a small self-focusing lens placed at the end of the delivery fiber. Typical angular divergence of optical fibers is about 25degrees. The output side of the delivery fiber is inserted inside a suspension of polystyrene spheres of diameter $1.11\mu m$ contained in a cylindrical tank of 15cm height by 24 cm diameter. The tip of the delivery fiber is 3cm below the liquid surface and 7cm from the bottom boundary of the container.

The original 10% concentration of the polystyrene spheres is diluted with distilled water to different concentrations. The first concentration is obtained by adding 10ml of $1.11\mu m$ polystyrene spheres to 4500ml of water. The second and third concentrations are obtained by adding 15ml and 34.65ml of $1.11\mu m$ polystyrene spheres to 4500ml of

water, respectively. The anisotropy factor is g=0.93. An optical fiber detector of 600μm core diameter is placed at 22mm from and same height as the delivery fiber inside the scattering medium. The collection angle is about 5degrees (FWHM) so that only light exiting the medium at a specific angle or orientation is collected. This small collection angle is possible by inserting a ferrule tube over the optical fiber in the collection side. This tubing is 5cm length of which 3.5cm serves as an extension to the fiber. This length of the tubing is used to eliminate the light outside the desired collection angle. Inside the tubing, different spacers are used to clip out the higher modes. The fiber detector is mounted on a rotational stage so that light scattered at different angles can be measured. The signal from the collection fiber is imaged on the input slit of the streak camera by a lens of focal length f=3cm.

7.3 Results

To determine whether some photons travel well-defined paths, an experiment is designed using a spherical ball painted black of about 5mm diameter placed in the midplane between source and detector. This ball is assumed to absorb any light incident on it. The ball is suspended by an invisible string of about 100μm diameter. There is minimum effect from the invisible string on the detected signal. The ball(referred to as object) is heavy enough to keep the string straight. The string is attached to a translation stage that moves the ball up and down on the midplane so that different depths(paths) of the scattering medium can be probed. The height of the object(H) is the distance from the center of the object to the line joining the source and detector tips as shown in Fig. 7–2. When the object is below the line, H is positive and when the object is above the line , H is negative. As shown in the figure, the object affects some very specific photon

paths. The photon paths that intersect the object are blocked; those that do not intersect the object are not disturbed by the presence of the object.

The absolute intensities represent the fraction of photons incident(1 incident photon) on the scattering medium detected by the fiber detector. Typical intensity profiles of the back-scattered light from polystyrene suspensions of transport mean free path l_t=15.45mm(R=S-D=1.4l_t) are shown in Fig. 7-3a. The profiles were measured when there was no object inside the medium and when the height(H) of the object was at H=0, 6, and 11mm. The scattered intensity profile for the object at height H=0mm starts to deviate from the intensity profile of the reference medium from the ballistic time of about 100ps. The intensity profile for object at H=6mm starts to differ enormously from the intensity profile for the reference medium(no object) at about t=120ps. This time is close to the computed time, 111ps, where one is supposed to start seeing a difference in the intensity profiles(the plots of the differences of the intensity profiles will be discussed in the next section). The time is computed by assuming that the least path a detected photon that hits the object can travel is a path formed by a straight line joining the source to the center of the object and from the center of the object to the detector. There is an enormous (about 80%) decrease of the detected peak intensity with respect to the peak intensity of the profile for the reference medium. These two intensity profiles become equal at about t=300ps. The intensity profiles for object at H=11mm and for the reference medium start to differ at about 160ps which is pretty close to the computed time of 140ps(path from source to object to detector). The peak intensity of the intensity profile for H=11mm shifts to early times by about 20ps as compared to the peak intensity of the profile for no object. These two intensity profiles become equal at about t=400ps.

These curves show that as the object is moved deeper and deeper inside the scattering medium, the time the detector first feels the effect becomes greater and greater because the detected photons that hit the object must travel longer distances. The effect starts earlier for H=6mm(t=120ps) than for H=11mm(t=160ps).

The intensity profiles of the back-scattered light from the polystyrene suspensions of transport mean free path l_t=4.47mm(R=S–D=5l_t) are shown in Fig. 7–3b. The intensity profiles for the reference medium and when the object is at height H=0mm start to differ from the ballistic time of about 100ps. This is to be expected because the photons that can reach the detector the earliest are the photons that travel the straight line joining the source to the detector. When the object is at height H=0mm, the center of the object falls exactly on that line and blocks the early arriving photons. The intensity profiles for the reference medium and when the object is at height H=6mm start to differ at time about t=120ps which is the same time as the case of l_t=15.45mm. The difference between the two profiles persists for long times. The peak intensity drops by about 35%. As the object is moved down to H=9mm, the difference with the profile of the reference medium becomes very small indicating that it might be difficult to detect an object inside a highly scattering medium. The profiles for the object located at H=9mm and 11mm look pretty much the same. For this reason only the intensity profile for H=9mm is presented.

7.4 Discussion

7.4.1 Photon paths for different concentrations of polystyrene spheres

The intensity profiles measured for different phantom media of different concentrations may be analyzed in two ways to obtain information about photon paths: 1) The difference, $\Delta I(t) = I_{no}(t) - I_H(t)$, between the intensity profiles in time for no object

inside the scattering medium, $I_{no}(t)$ and the object at a certain height H, $I_H(t)$ inside the scattering medium and 2) the relative difference $\frac{\Delta I(t)}{I_{no}(t)} = \frac{I_{no}(t)-I_H(t)}{I_{no}(t)}$ given by the ratio of the intensity difference to the intensity when there is no object inside the scattering medium. This difference gives the number of photons travelling along a particular path absorbed by the object for one incident photon on the scattering medium; The second way, the relative difference, gives the percentage of photons travelling a particular path absorbed by the object.

In this section, both difference and relative difference are used to discuss the photon paths.

Fig. 7–4 shows the difference of detected intensities at various times for no object inside the scattering medium and the ball object at a certain height (H) inside the scattering medium of transport mean free path l_t=15.45mm. A large difference at a certain time means that a large number of photons following a particular path from the source to the detector intersecting the object has been absorbed by the object. A small difference means that the object barely affects the photon paths that reach the detector at that particular time. Four different heights (H=0mm, H=6mm, H=9mm, and H=11mm) of the object are displayed. The effect is clear when the ball is placed at H=0 with maximum effect at about time t=145ps. As the object is moved to H=6mm, the peak of the intensity difference increases by about 60% and moves to t=175ps. The increase in the peak of the intensity difference is attributed to the fact that in the absence of an absorbing object a great number of detected photons travels the path from the source to H=6mm and to the detector. When the object is placed there(H=6mm), it just blocks many of these photon paths and that makes a large difference in the peak intensity. The curve profile of the

intensity difference is shifted by about 12ps with respect to the previous one meaning that the effect of the object ball at H=6mm is seen later by the detector than the effect of the object at H=0mm. In other words, the photons that travel the straight path from the source to the detector arrive at the detector earlier than those that travel the curve path from the source to H=6mm and to the detector. The difference approaches 0 for times greater than 300ps implying that the object at H=6mm does not affect any paths of photons that reach the detector after the time t=300ps for this geometry. When the object is placed at H=9mm, the peak of the intensity difference decreases by about 37.5% and shifts to t=200ps. For the case of the object at H=11mm, the peak of the difference falls at t=220ps and decreases by 12% as compared to the intensity difference when the object is at H=9mm. The difference is zero for times greater than 400ps. There is a broadening of the intensity difference as the object is moved deeper and deeper inside the scattering medium. This means that for objects deep inside the scattering medium, the object affects a wide range of photon paths. That may make it difficult to precisely specify the location of an object deep inside a scattering medium.

As said before, the analysis using the difference of the profiles does not yield a complete picture about the effect of the hidden object. The difference just gives the number of photons following a particular path affected by the presence of the absorbing object. From that difference, one can not really see how big or small that number of affected photons is when compared to the number of photons that would normally reach the detector in the absence of the absorbing object. To have a better idea about the effect of the object, one must understand also the "weight" of the difference which is given by the relative intensity difference. Fig. 7–5 shows the relative intensity difference

which is the ratio of the difference of the intensity profiles for no object and the object at a certain height inside the scattering medium to the intensity profile for no object inside the scattering medium. The relative intensity difference represents the fraction of photons following a particular trajectory affected by the presence of the object. For instance, in this figure, when the object is at H=0mm, the maximum of the relative intensity difference is 0.71 at t=112ps. This maximum means that of the photons that would normally travel(where there is no object inside the scattering medium) the path from the source through the object position and detected at time t=112ps, about 71% have been absorbed by the object. When the object is moved to H=6mm, the fraction of the photons absorbed is about 48% at t=157ps. The maximum percentage of photons absorbed by the object decreases as the object is moved deeper inside the scattering medium; it is 33% and 31% for the paths arriving at t=200ps and t=226ps at the detector, respectively. The effect of the object consistently decreases as it is placed deeper inside the scattering medium.

One can remark that the time of the peak of the intensity difference is greater than the time of the peak of the relative intensity difference for H=0mm and H=6mm. The reason is that when the object is placed at these positions, the effect is maximum at early times. However, at early times, the intensity is very low. Therefore even when the intensity difference is maximum at a certain time, by dividing this difference by small numbers the peak of the relative intensity difference can move to other times.

Fig. 7–6 shows the intensity difference for higher scattering medium of l_t=10.3mm and for H=0, 6, 9, and H=11mm. The peak of the intensity difference is about the same for H=0 and H=6mm. A shift in the peak of about 40ps is observed from H=0mm to

H=6mm. From H=6mm to H=9 mm the peak drops by 50% and moves by 35ps. The intensity difference for H=11mm is very low and broad. The peak falls at t=220ps.

Figs. 7–7 shows the intensity difference for l_t=4.47mm and for H=0, 6, 9, and 11mm. The effect of the object is felt for H=0mm and H=6mm. Contrary to the case of l_t=15.45mm where the peak of the intensity difference increased by about 60% from H=0mm to H=6mm, this time the peak of the intensity difference decreases by about 40% and shifts from t=175ps to t=260ps from H=0mm to H=6mm. The effect of the ball extends to times as long as 1000ps . The extent of this difference indicates that in highly scattering media photons that travel paths close to the line joining the source and detector are very intense. Once disturbed, these photons will affect most of the intensity profile. The intensity differences between the profiles for no object and the object at heights H=9 and 11mm are almost flat. There is no clear maximum. This means that for highly scattering media, the effect of a hidden object on the photons that travel paths that intersect the object is not localized. This is why it may be difficult to exactly locate an object deep inside a very dense scattering medium.

From these data plots(Figs. 7–4, 7–5, 7–6, and 7–7), two different factors are seen to affect the photon paths: the depth of the object inside the scattering medium and the scattering properties of the medium. When the object is deep inside the medium, its effect is almost negligible on the detector. That is why the effect of the object placed at H=20mm inside the scattering medium of l_t=15.45mm is barely noticeable. The depth of effect of the object becomes less and less as the medium becomes more and more scattering. For the medium of transport mean free path l_t=4.47mm , the effect of the object at depth as low as 11mm is almost zero.

As the object moves deep inside the medium, its effect can reach the detector only at late times. Groups of photons arriving at late times have no well defined paths because they have travelled all over the scattering medium. These photons are completely randomized and follow a diffusion-like behavior. Therefore, those few late photons that have hit the target object do not affect the detected intensity at any particular time so as to see clearly the photon path deep inside the medium. In other words, one can say that for objects located at approximately more than half the source detector(S–D) distance, the width of the photon path is too broad to determine the object location accurately. The maximum depth at which an object can be detected is further reduced when the medium is highly scattering.

When the medium does not strongly scatter light, the snake light can go deep inside the medium and return to the detector. This is why the object is seen so clearly for S-D=$1.4l_t$, and $2.1l_t$ for depths almost equal to half the source-detector separation. There is a group of photons following well defined paths in the time range from 100ps to 250ps. When the object moves, a localized group of photons is affected. As the medium becomes more and more scattering (S-D=$5l_t$), the snake region moves closer and closer to the line joining the source and the detector and deep structures can not be resolved because photons reaching those structures are randomized and follow diffusion-like behavior.

The determination of the location of an object inside scattering media offers great promise for imaging sub-millimiter structures. One problem in using the backscattered geometry for the anisotropy factor $g \approx 1$ is the small amount of signal that goes back to the detector in the non-diffuse region. This signal must be integrated over a long time to have a reasonable signal to noise ratio. With a good signal to noise ratio, it is possible

to locate the position of the target object by slicing the intensity profile in time.

Fig. 7–8 shows plots of the intensity difference against the position of the object at different time slice for a source-detector separation of 22mm and l_t=15.45mm. Fig. 7–8a shows the intensity difference between the intensity profiles from the reference medium and when the object is placed at different depths inside the scattering medium at time slice t=146ps. It can be easily seen that the position of the object is around 3mm. Fig. 7–8b shows the intensity difference at time t=175ps. The peak has moved to H=7mm. The peak has moved to around H=12mm for the intensity difference at time t=222ps(Fig. 7–8c). These three curves show that it may be possible to pinpoint the position of a hidden object from the back-scattered intensity profile. Different portions of the intensity profile carry informations from different parts of the scattering medium. For instance at t=146ps an object located at H=12mm has almost no effect on the detected intensity. At that location of the object(H=12mm), the detector feels the effect of the object at t=222ps. Slicing the time can yield the object position.

The position of the object can be located by considering the fraction of photons absorbed by the object. This is done by slicing in time the relative intensity difference as shown in Fig. 7–9. The position of the object is about the same as slicing the intensity difference as described in the preceding paragraph. The major difference is that the relative number of photons absorbed decreases as the object moves deeper inside the medium. This means that when compared to the number of photons that would have been detected without the presence of the absorbing object, the difference in detected intensity has more and more effect as the object is moved closer and closer to the line joining the source and detector for this geometry.

Contrary to the case in Figs. 7–8 and 7–9 where the object can be located by slicing the intensity in time, the object seems to be always at the same position when slicing in time the intensity difference profile for l_t=4.47mm and R=S-D=5l_t. Fig. 7–10 shows that the peak of the difference does not move as the profile is sliced for different times. This is because the more intense paths are located close to the line joining the source to the detector. When the object is placed close to that line most of intense paths are absorbed. That affects strongly the detected intensity profile which implies that the intensity difference is high. When the object is moved deeper inside the scattering medium, the paths become less intense meaning that the object barely affects the detected intensity profile implying that the intensity difference is very low. The intensity difference, then, is the largest for the various time slices when the object is between H=0 and 3mm. For highly scattering media then, it may be very difficult to locate correctly an object deep inside. The object position may seem to be always near the surface.

7.4.2 Angular dependence of photon paths

In the previous section we have shown that the detected intensity is sensitive to the height of the object. In real life, however, one can not move a tumor object up and down inside human body to study the effect of the tumor on the detector. However, one can vary the position and orientation of the detector to study the effect of the object. By varying the detector orientation, we will show, in this section, using the same experimental conditions as before, that the photon paths have an angular dependence. This angular dependence can make it possible to locate an object inside a scattering medium.

Fig. 7–11 shows the intensity difference for no object and object located at H=6mm

inside the scattering medium for two different orientations, 0 and 15 degrees of the fiber detector . The peaks of the paths clearly move from t≈150ps for the detector oriented at 15degrees to the medium to t≈=175ps for the detector oriented at 0 degree to the medium. The effect of the object to the detector oriented at angle=15degrees is more(about 30%) than that for the detector at angle=0degree. This clearly shows that some paths of photons are angle sensitive and that one can probe different depths of a scattering medium by just changing the orientation of the detector.

To verify this possible angular dependence, the object is placed in a suspension of intralipid scatterers of transport mean free path l_t=4mm. The source to detector distance (S-D) is 14.5mm. The object is placed at H=6mm and in the plane 10.3mm from the source between the source and the detector. The intensity difference for no object and H=6mm inside the medium is shown in Fig. 7–12. There is absolutely a shift in the peaks. The shift is about 40ps. Furthermore, the peak of the intensity difference of the object for the detector oriented at angle=30degrees is about 3 times that for the detector at angle=0degree. This angular dependence of some photon paths can be useful for imaging hidden objects inside scattering media.

7.4.3 The dependence of detected intensity on the anisotropy factor g

Many researchers have been investigating intralipid suspensions with anisotropy factor of about 0.7. Optical imaging will be applied in human tissues of anisotropy factor about 0.9. The question to be addressed is: Is it possible to expect the same conclusions in intralipid as in tissue or in general any other particles in the diffusion region?. In this section, we will investigate two suspensions with polystyrene spheres of completely different anisotropy factors(g) and determine whether the pulse profiles are

different or the same for same source-detector separation in transport mean free paths.

Transmitted pulse measurements were performed using the femtosecond laser and a streak camera. The light was incident to the sample through an optical fiber. The tip of the fiber touched the sample container. The container was a 50mm diameter cylindrical glass cell of pathlength 20mm. The container was respectively filled with polystyrene spheres of diameters d=1.07μm and d=0.107μm. The concentrations of the polystyrene spheres were 7.7% of stock (stock was 10%)(l_s=0.91mm) and 3.3% of stock(l_s=0.076mm) for d=0.107μm and d=1.07μm, respectively so that the distance in l_t could be the same. The anisotropy factors of these two particle sizes are, respectively, g=0.094 and g=0.93. For the two different concentrations, the transport mean free path of both particle sizes is 1mm. An optical fiber placed on the transmitted side of the sample container collects and delivers the scattered light to the ultrafast streak camera system. The source to detector separation is $20l_t$ which is well in the diffusion region.

The detected profiles normalized are showed in Fig. 7–13. As can be seen, except for the ballistic part for the small particles, the profiles are essentially the same for both sizes of particles. Therefore, in the diffusion region, the detected signal profile is independent of the sizes of the particles. The profiles depend only on l_t, but not separately on l_s and g. If l_s and g are varied to yield the same l_t($l_t = \frac{l_s}{1-g}$), the profiles of the scattered detected intensities should be the same.

7.5 Conclusion

It has been showed that there is a possibility that photons may travel along well-defined paths inside the scattering medium. This fact can make it possible to detect objects with sub-millimiter resolution in the near diffusive limit. In the non diffusive

region, an object located inside the scattering medium affects a specific group of photons. This group of photons arrives on the detector at a specific time. The time of arrival of the group of photons affected by the object changes as the position of the object changes. Such change in the arrival of the photons shows that it is possible to pinpoint the location of a hidden object. The change in the arrival time of the most probable group of photons has been accomplished also by changing the orientation of the detector. The technique of varying the angle of detection can make it possible to locate a hidden tumor inside human tissues. In the diffusion limit, however, the well defined paths arrive very early which is why the effect of the object can be seen more or less clearly when placed close to the straight line joining the source to the detector.

It has been showed that in the diffusion region, the scattered pulse profiles depend only on the transport mean free path but not on l_s and g separately. As long as l_t is the same and the source-detector separation is $>>7l_t$, no matter how much l_s and g change, the pulse profile is the same.

7.6 References

1. W Cui, N. Wang, and B. Chance, "Study of photon migration depths with time-resolved spectroscopy," Opt. Lett. **16**, pp. 1632–1634, 1991.

2. A. H. Grandjbakhche, G. H. Weiss, R. F. Bonner, and R. Nossal, "Photon path-length distributions for transmission through optically turbid slabs," Phys. Rev. E **48**, pp. 810–818, 1993.

3. L. T. Perelman, J. Wu, I. Itzkan, Y. Wang, R. Dasari, and M. S. Feld, "Photon paths in turbid media: Theory and Experimental observation," OSA Proceedings on Advances in Optical Imaging and Photon Migration, edited by R. R. Alfano (Optical Society of America, Washington, DC, 1994), Vol. **21**, pp. 153–155.

4. A. Ya. Polishchuk and R. R. Alfano, "Fermat photons in turbid media: An exact analytic solution for most favorable paths- a step towards optical tomography," submitted to Phys. Rev. Lett.

5. A. Ya. Polishchuk and R. R. Alfano, " "Fermat" photons in random media: Diffusion on the velocity sphere and principle of the least mean-square curvature," submitted to Phys. Rev. Lett.

6. F. Liu, K. M. Yoo, and R. R. Alfano, "Transmitted photon intensity through biological tissues within various time windows," Optics Lett., **19**, pp. 740–742, 1994.

7. K. M. Yoo and R. R. Alfano, "Time-resolved coherent and incoherent components of forward light scattering in random media," Opt. Lett. **15**, pp. 320–322 1990.

8. J. A. Moon and J. Reintjes, "Achievable Image Resolution using non-diffuse multiply scattered light," OSA Proceedings on Advances in Optical Imaging and Photon

Migration, edited by R. R. Alfano (Optical Society of America, Washington, DC, 1994), Vol. **21**, pp. 149–152.

9. J. Chang, Y. Wang, R. Aronson, H. L. Graber, R. L. Barbour, B. B. Das, J. Dolne, K. M. Yoo, and R. R. Alfano, "Time-resolved imaging in dense scattering media", SPIE Vol. 1887, 1993.

10. J. R. Singer, F. A. Grunbaum, P. Kohn, and J. P. Zubelli, "Image reconstruction of the interior of bodies that diffuse radiation," Science **248**, 990–993, 1990.

11. M. S. Patterson, B. W. Pogue, and B. C. Wilson, "Computer simulation and experimental studies of optical imaging with photon density waves," SPIE Vol IS11, Medical Optical Tomography: Functional Imaging and Monitoring, pp. 513–533, 1993.

7.7 Figures

Figure 7.1 Experimental arrangement to study photon paths in forward scattering media.

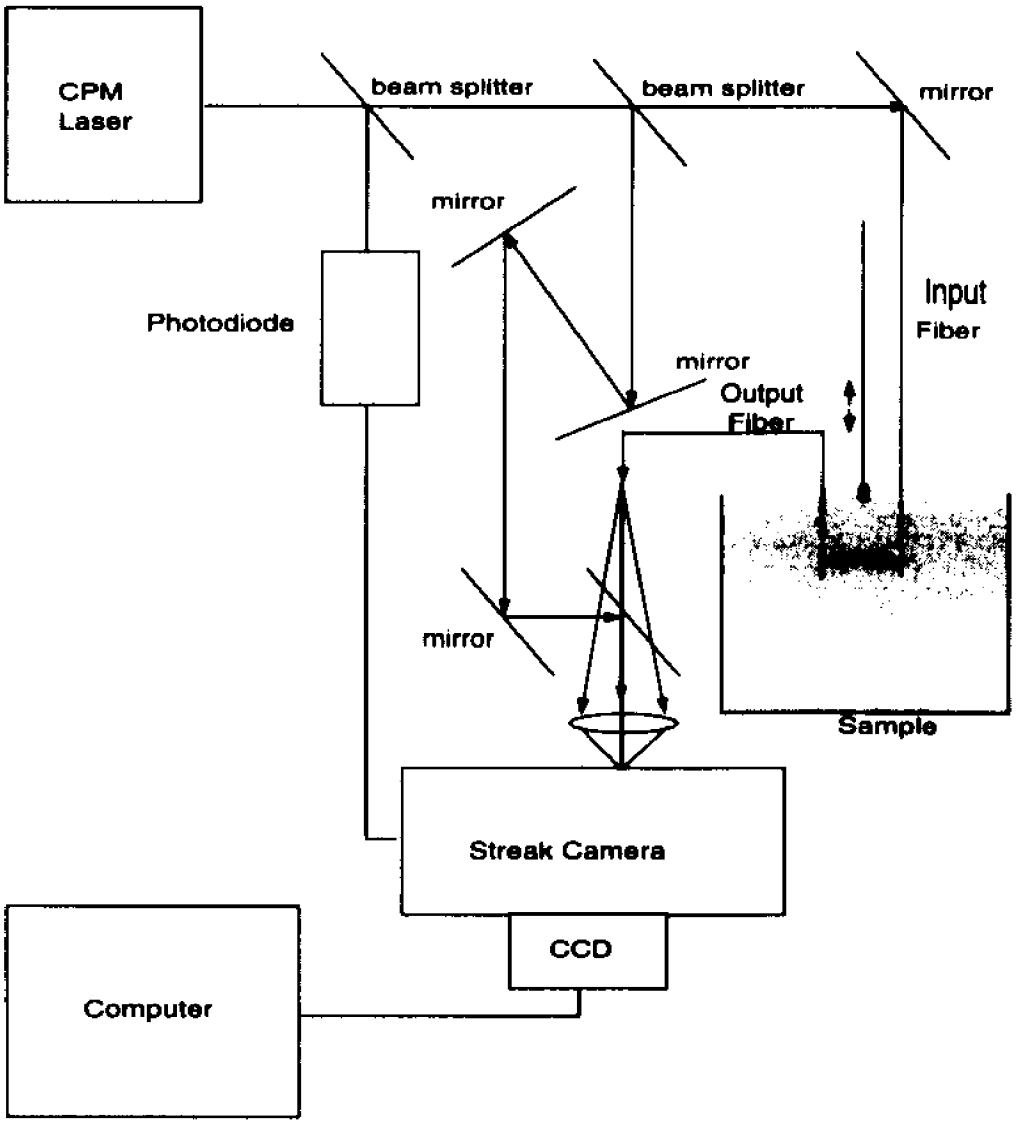

Figure 7.2 The geometry showing the object inside the scattering medium. When the center of the object is below the line joining the source and detector tips, H is positive When the center of the object is above the line joining the source and detector tips, H is negative.

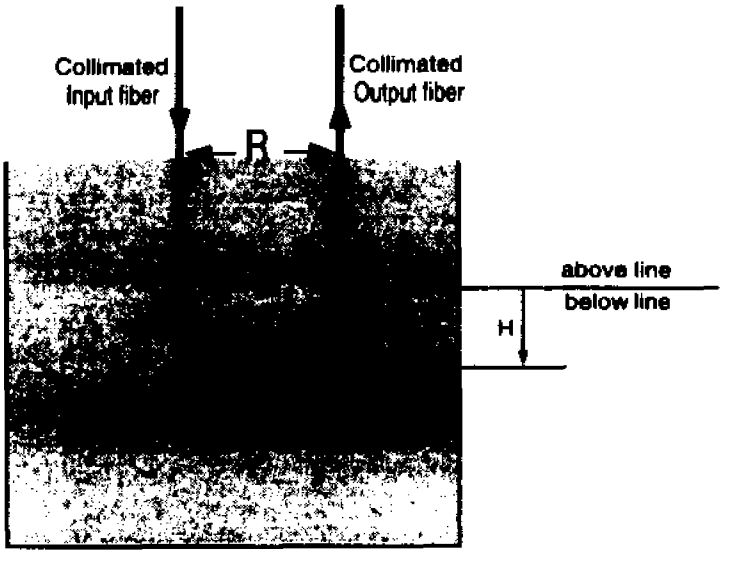

Figure 7.3 The temporal profile of the back-scattered intensity for no object and object placed at H inside the scattering medium of a) l_t=15.45mm b) l_t=4.47mm; the profiles for H=9mm and H=11mm are pretty much similar. R=S-D=22mm.

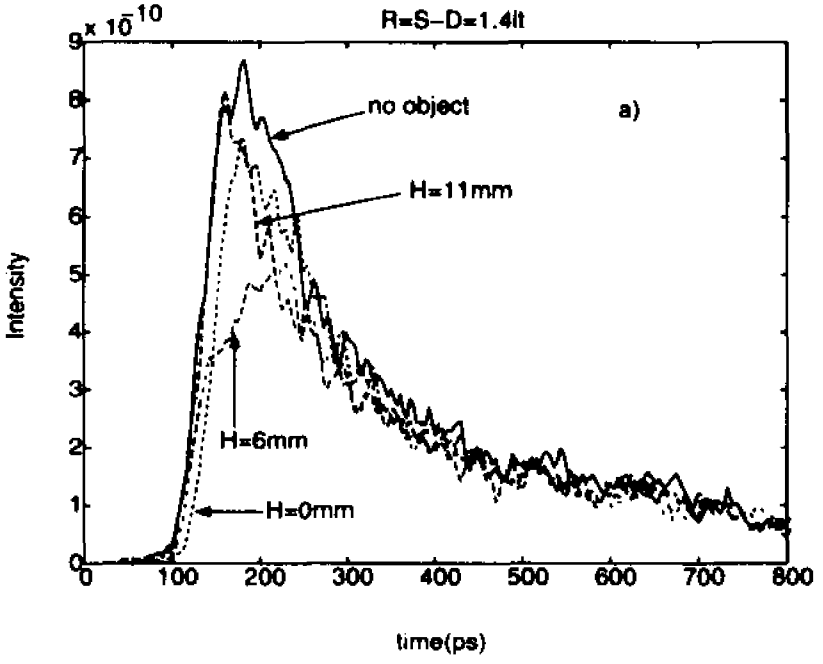

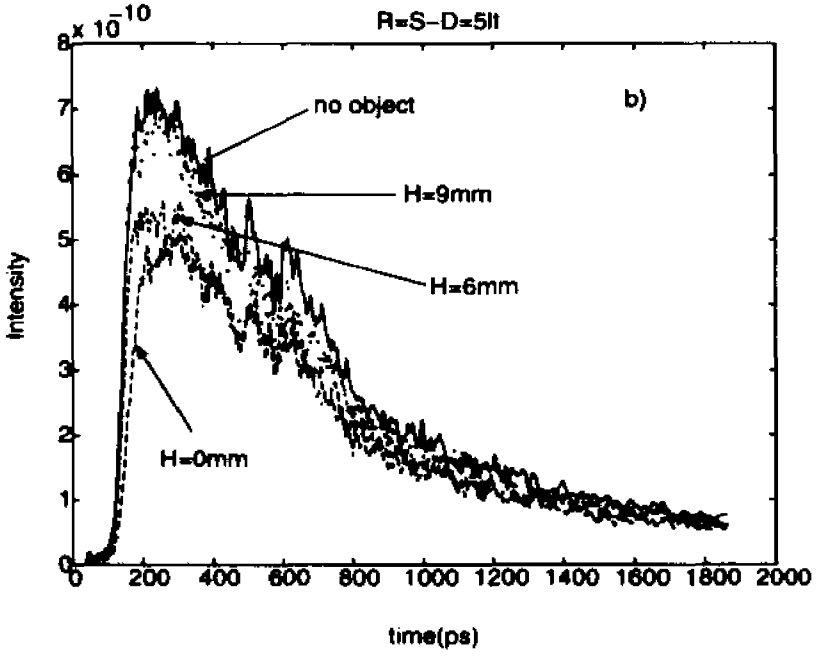

Figure 7.4 Difference of intensity profiles between no object and object placed at height(H) inside the scattering medium of l_t=15.45mm. R=S-D=22mm.

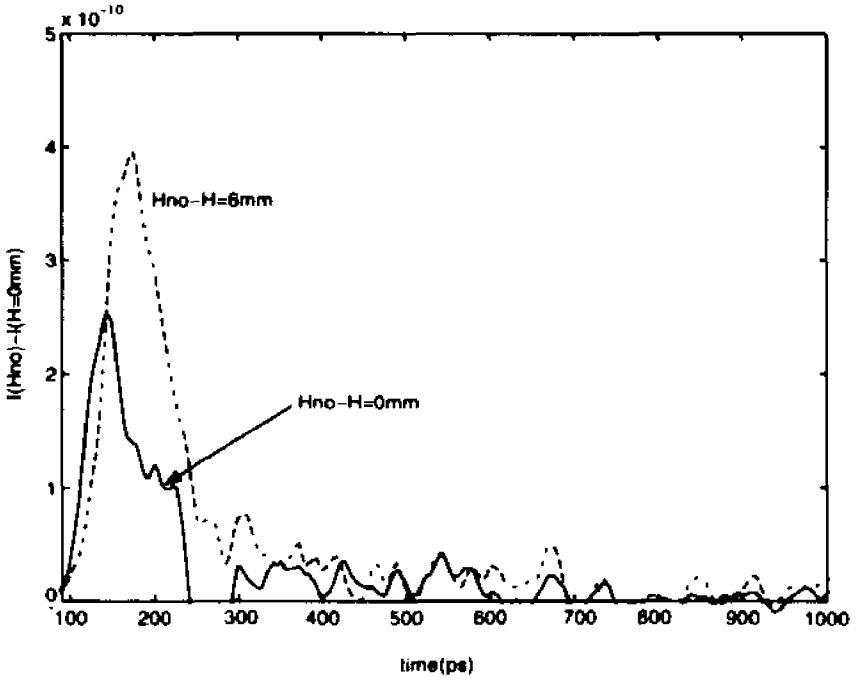

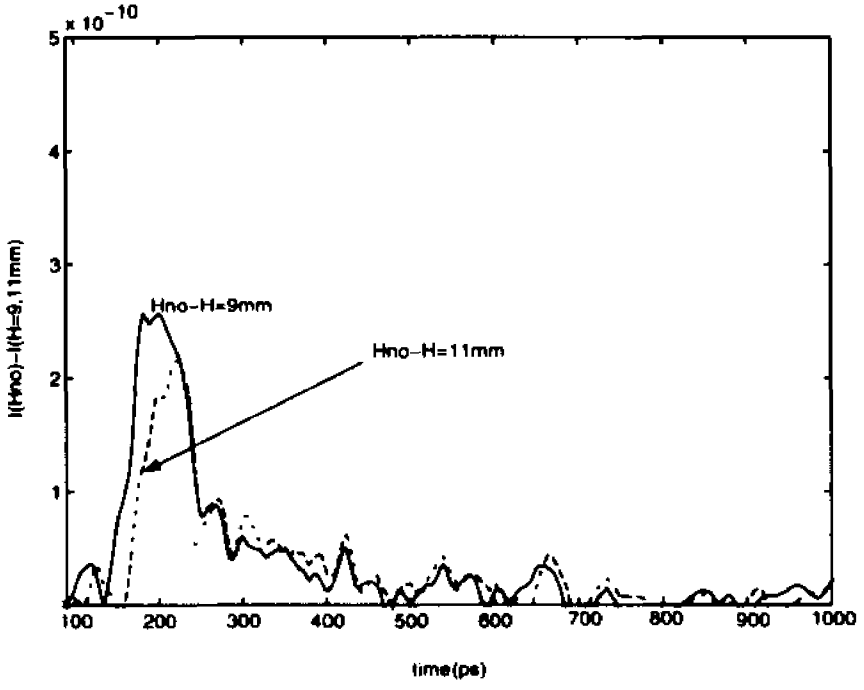

Figure 7.5 Relative intensity difference profiles between no object and object placed at height(H) inside the scattering medium of l_t=15.45mm. R=S-D=22mm.

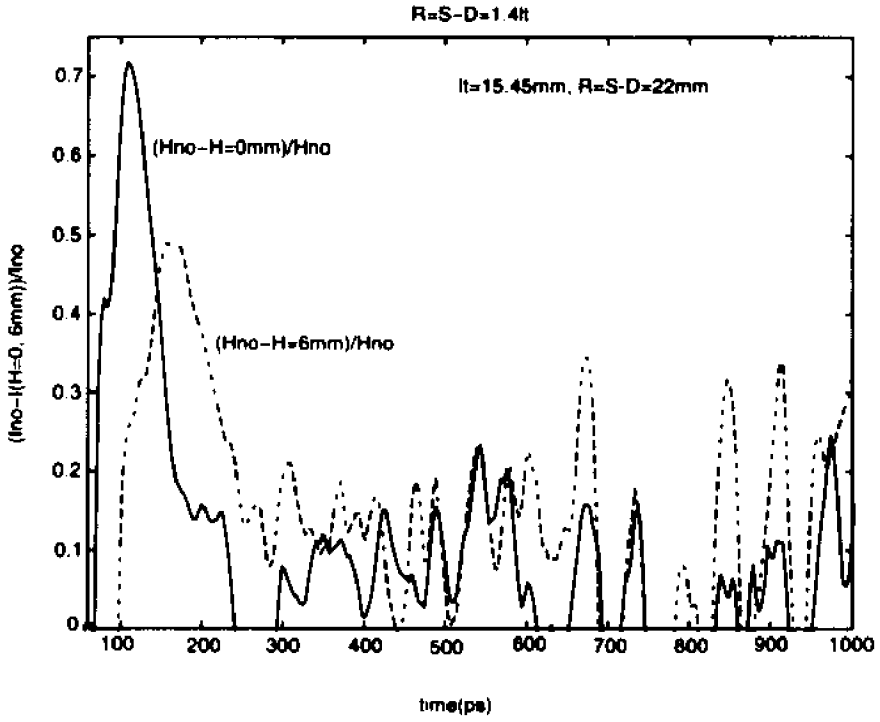

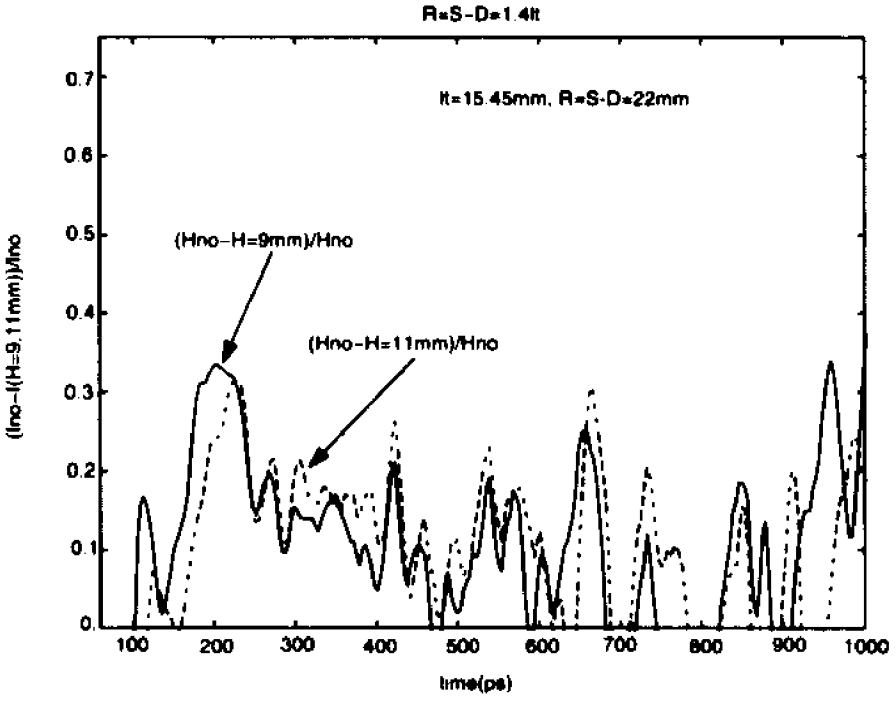

Figure 7.6 Difference of intensity profiles between no object and object placed at height(H) inside the scattering medium of l_t=10.3mm and R=S-D=22mm for different time.

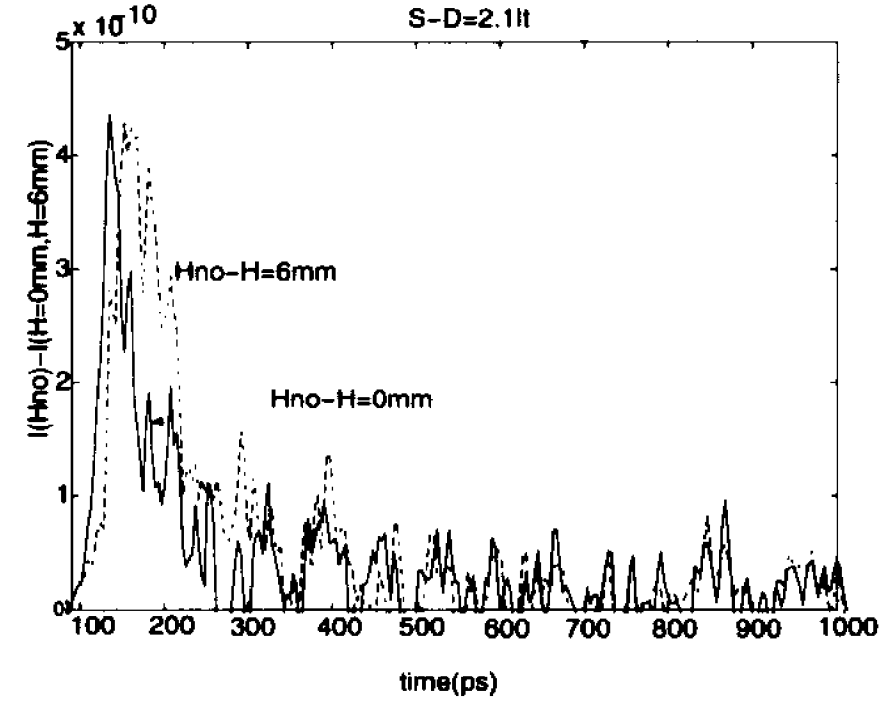

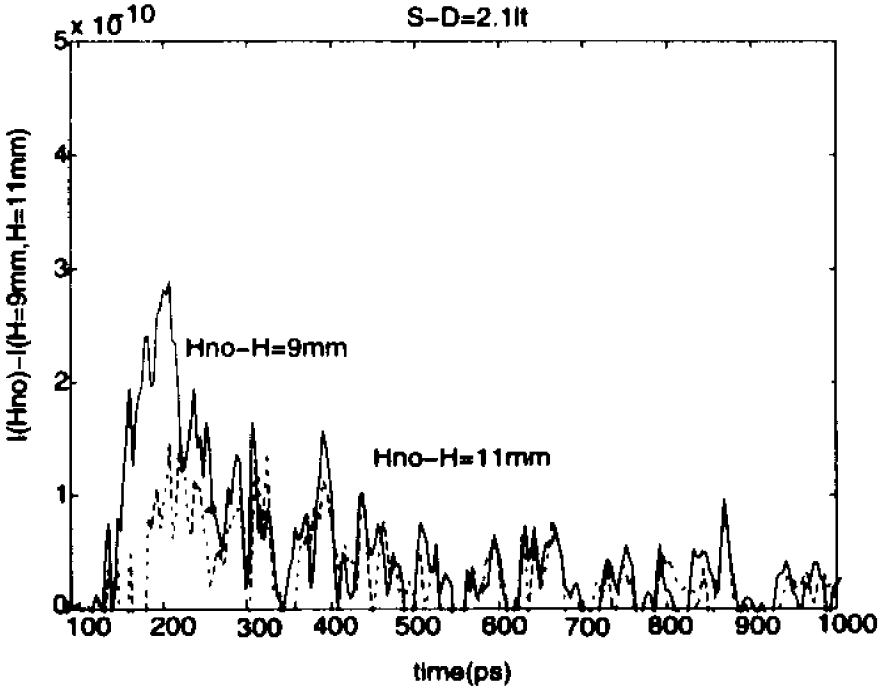

Figure 7.7 Difference of intensity profiles between no object and object placed at height(H) inside the scattering medium for lt=4.47mm and R=S-D=22mm=5lt.

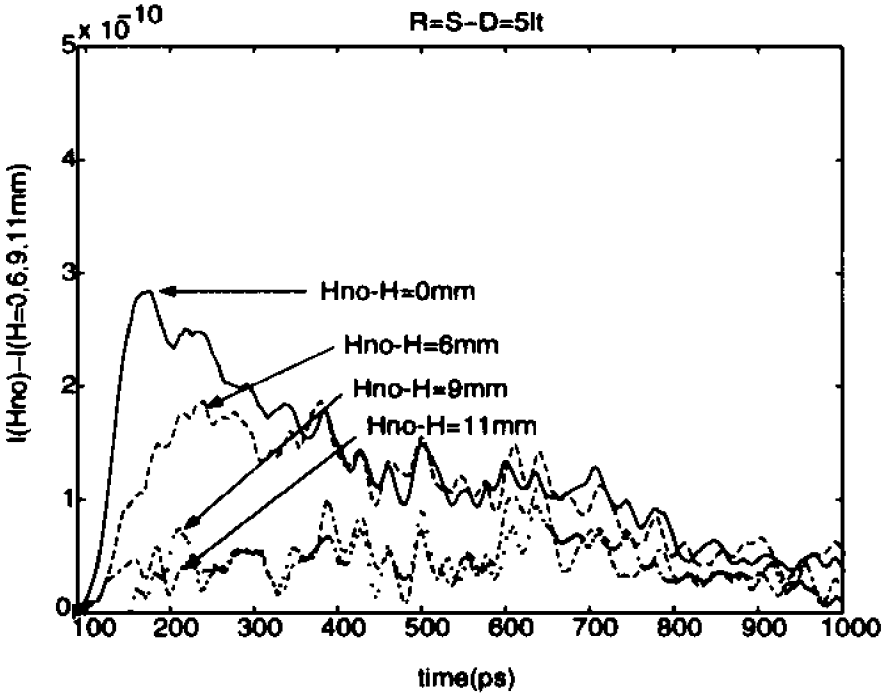

Figure 7.8 Intensity profile difference vs different heights of the object at specific times a)t=146ps b)t=175ps, and c) t=222ps; l_t=15.45mm, R=S-D=22mm=1.4l_t.

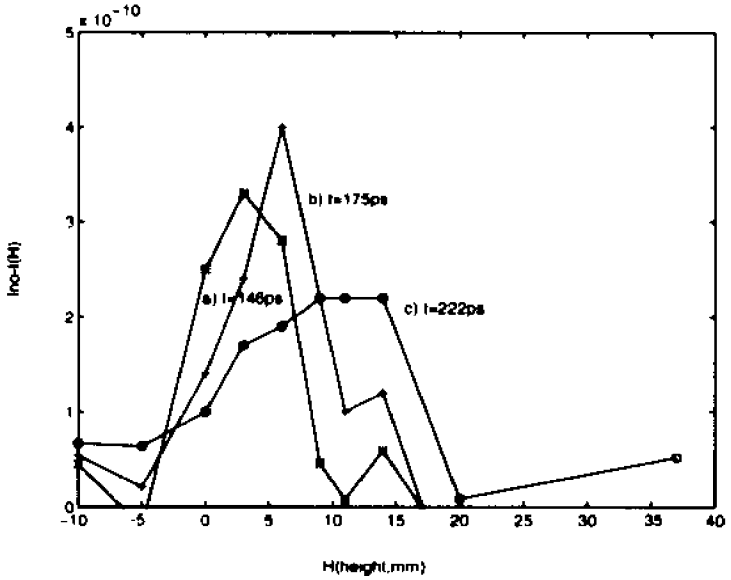

Figure 7.9 Relative intensity difference against H for different time slices a)t=146ps b)t=175ps, and c)t=222ps for polystyrene spheres of l_t=15.5mm. R=S-D=22mm=1.4l_t.

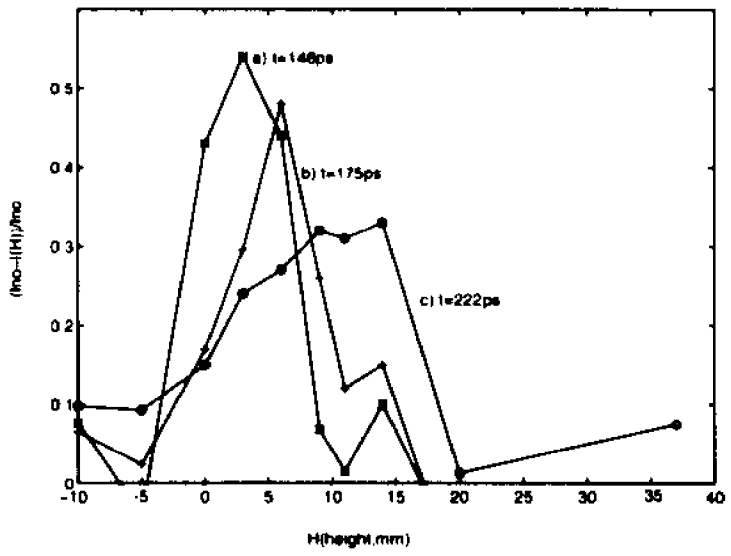

Figure 7.10 Intensity profile difference vs different heights of the object at specific times a)t=146ps b)t=175ps, and c) t=222ps; l_t=4.47mm, R=S-D=22mm=5l_t.

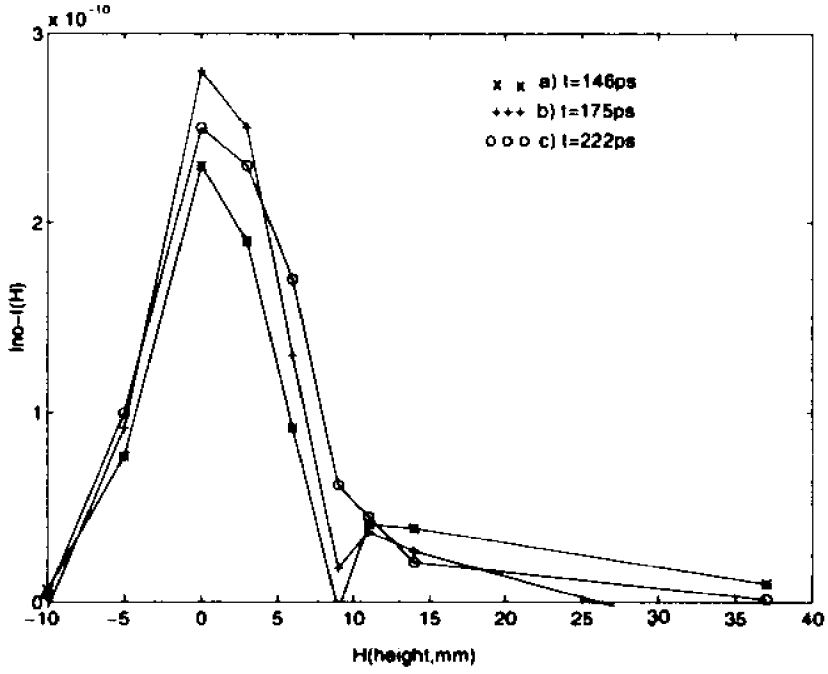

Figure 7.11 Intensity difference for two different orientations of the fiber detector for l_t=15.45mm, R=S-D=22mm=1.4l_t.

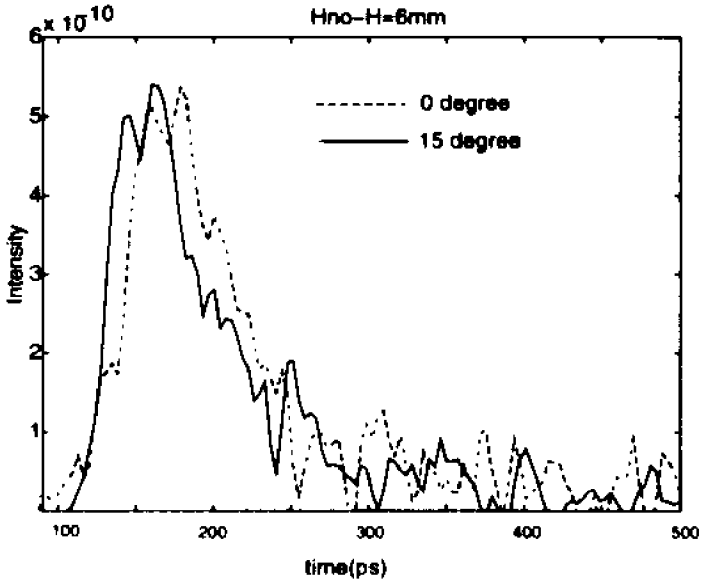

Figure 7.12 Intensity difference for two different orientations of the fiber detector. Object is placed at H=6mm and on the plane 10.3mm from the source between the source and the detector.

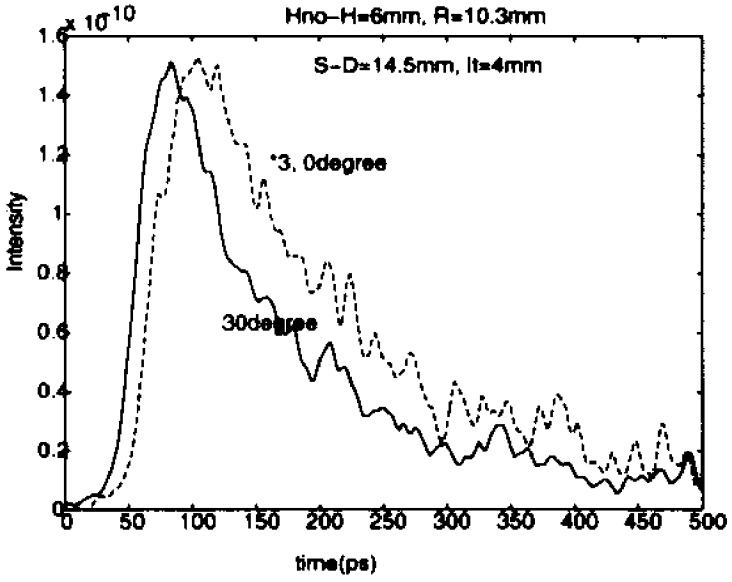

Figure 7.13 Normalized intensity profile for two suspensions of polystyrene microspheres of g=0.093(d=0.107microns) and g=0.93(d=1.07microns).

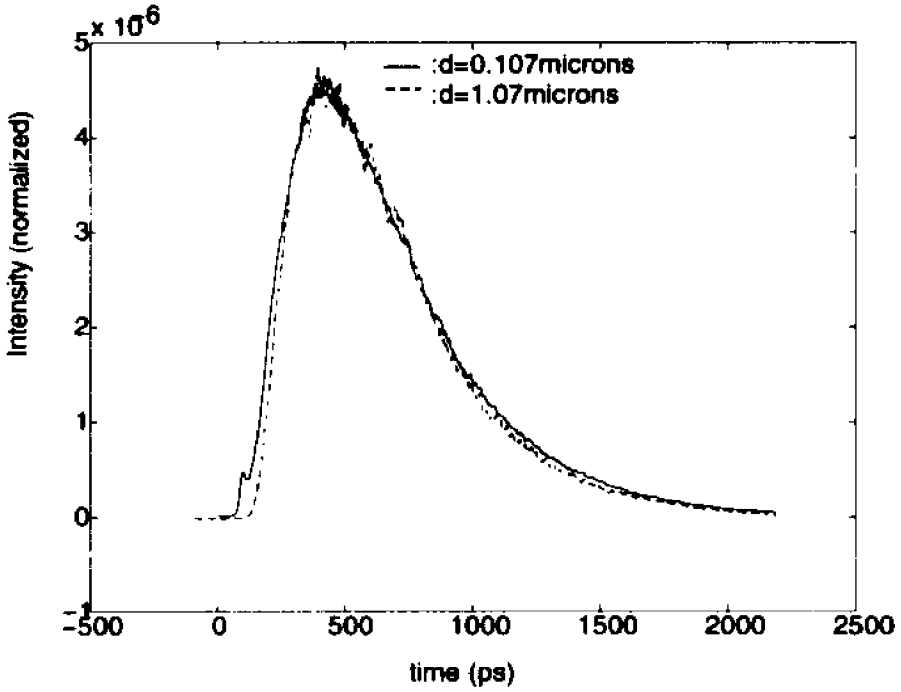

Chapter 8

Summary

CW light and a spatial filter have been used to image an object hidden behind random scattering particles. It has been found that when the spatial filter diameter is d, only the spatial frequencies below the cut-off spatial frequency $\frac{d}{2\lambda f}$ can pass through. The higher frequency components representing the highly scattered light are cut off by the spatial filter. Some of the highly scattered light that would come out collinear with the ballistic light is absorbed by the host medium because the scattered light travels a longer distance than the ballistic light. This way, one can obtain an image of the object with approximately ballistic light quality by closing down the spatial filter diameter to cut off as much scattering light as possible. It has been shown that the scattering cross-sections are lower for NIR light about $1.3\mu m$ than for visible light around $6.70\mu m$. We have shown that the best image of a hidden object is obtained when the spatial aperture diameter is closed to the minimum and the longest wavelength($1.3\mu m$) of light in the therapeutic window is used.

Light back-scattered from a two-layered medium has been studied. We have shown that a layer of intralipid scattering medium placed on top of a semi-infinite piece of wax can be reconstructed using the Fourier transform solution to the diffusion equation. When the top layer thickness is more than the source-detector separation, the signal detected has not propagated deep enough to reach the bottom layer and that makes the inverse parameters of the bottom layer not unique. The layers are reconstructed uniquely when the source-detector separation is more than the depth of the top layer.

Scattered pulses around intralipid scattering medium have been measured. We have found that the intensity profiles around the scattering medium decrease as the medium becomes more scattering. The experimental observations are confirmed by the diffusion model. We have shown a novel way of obtaining the transport mean free path and the absorption of a scattering medium by using only the peak intensity and the risetime of the pulse profile. We have shown that it is possible to obtain multiple experimental pulse profiles for the reference medium by using only one detector at a single position and an appropriate theoretical model. This result is very important for inverse reconstruction algorithms using real human tissues where the reference data are often needed and one can not take the hidden object out to take a reference data.

Laser pulses back-scattered from a homogeneous semi-infinite suspension of intralipid scatterers have been measured at different orientations of the detector. We have found that below the diffusion region(S-D < $7l_t$), the detected intensity has an angular dependence. However, in the diffusion region(S-D > $7l_t$), the detected intensity is almost the same regardless of orientation of the detector.

Our measurements show that photons in the non-diffusive limit have well defined paths inside the scattering medium. We have shown that each path reaches the detector at a specific time and the deeper the target object is, the later the arrival time. When slicing the time of arrival of the photons, we have shown that the position of the object can be located. Changing the depth of the target object is equivalent to varying the angle of collection of the detector. This method can be easily used for real breast experiments.

Transmission experiments have been performed on scattering media of different sizes(g=0.093 and g=0.93) but same transport mean free path to determine whether,

in the diffusion region, the pulse profile depends on the size of the scattering particle. We have found that in the diffusion limit, the scattered pulse profiles are the same except for a small difference in the ballistic region.

Chapter 9

Future research directions

The research work that has been conducted in this thesis needs to be continued. More experiments using spatial filter should be carried out to try to optimize the quality of the image obtained. Different shapes of spatial filters should be used to try to eliminate as much as possible of the diffuse light and image the ballistic light. After the image is improved, experiments must be performed to determine exactly what the object is.

Experiments need to be done in the NIR region around 1300nm to take advantage of the absorption of water that can make it easier for light to emerge from human tissues with minimum scattering since the highly scattered light is absorbed by the water. This way, the detected signal will have enormous ballistic information on the hidden object.

Additional experiments must be done using the photon path concept. Theoretical or experimental techniques must be developed to isolate photons that travel very different trajectories but nevertheless reach the detector at the same time and angle. Multiple fiber system needs to be used to determine the multiple photon paths that travel from the source to the detector so that the position and the size of the object can be located. When that is realized, object of sub-millimiter size can be detected.

Experiments need to be preformed on real breast tissues in vivo to determine and see the difference between the optical properties of each breast. The difference in optical parameters of the breast from different persons will also be determined.

Transmitted and back-scattered signals will be compared to check what geometry is more probable to yield better imaging results. The light back-scattered and detected

has to go inside the scattering medium and come back. This means that for some thick scattering medium, the back-scattered light may not penetrate enough to reach the hidden object. The transmitted light, however, always passes through, at least, the volume of scattering medium around the straight line joining the source and the detector. By scanning the source and the detector, the signal from a hidden object will eventually reach the forward detector.

The results found from reconstructing the two-layer problem are encouraging. The failure of the diffusion theory to find uniquely the layer parameters when the thickness of the top layer is about half the source-detector separate brings home the need for a better theory. The new theory must be able to reconstruct large and thin and multiple layers. Theoretical approaches using photon path integral can be used to check whether that can yield better results.

More reconstruction work will be done by using multiple sources and multiple detectors. The sources and detectors will be placed at different orientations. The sources will be turned on and off to avoid interference in the detected signals. Different theoretical models such as the exact transport equation, diffusion, telegraph, and the non-Euclidian diffusion equation will be used to reconstruct the inverse parameters of a hidden object inside a highly scattering medium. Different shapes, size, packing density of the scattering medium will be considered.

Current reconstruction algorithms can take hours of computer time using a fast computer. In real life, one expects results right away. Therefore fast reconstruction algorithms will be developed to perform efficiently the reconstruction. Some methods to estimate an unknown system from the input and output signals used in control theory

will be borrowed to reconstruct a hidden object.

Appendix

In this appendix, some of the computer programs used in this thesis will be presented. The program in A.1 was provided by Dr. A. Ya. Polishchuk. The programs in A.2 and A.3 were provided by Prof. F. Liu.

A.1 Program to fit the two-layer data from chapter 4

```
******main**********************
implicit double precision (a-h,o-z)
character*12,outfile
double complex fr,gxom,f,gxom1,gxom2,coeff1,coeff2,grgxom,grfr,fr1,grgrfr
common /prop/ d1,bl1,d2,bl2,n1,n2
common /pi/pi
common/bound/z0,z1
pi= 4.d0*datan(1.0d0)
write(6,*) 'pipi',pi
v=300.d0
print*, "please, enter the index of refraction for the top layer"
read *, n1
print*,"please, enter index of refraction for the bottom layer"
read *, n2
v1=v/1.33d0
```

```
v2=v/1.43d0

print*,"please, enter the mean free path for the top layer"

read *, al1

print*, "please, enter the mean free path for the bottom layer"

read *, al2

print*," please, enter the absorption length for the top layer"

read *, absl1

print*," please, enter the absorption length for the bottom layer"

read *, absl2

d1=v1*al1/3.d0

d2=v2*al2/3.d0

bl1=dsqrt(al1*absl1/3.d0)

bl2=dsqrt(al2*absl2/3.d0)

z0=0.71045d0*al1

print*, " please, enter the thickness(depth) of the top layer"

read *, z1

print*, " please, enter the source detector separation"

read *, r

c  r=15.0d0

z=z0

print*,"please, enter the name for your output file"

read *,outfile
```

```
open(10,file=outfile)
zz=z-z0
zzz=z+z0
omega = 50.
print*, "omega=",omega
c omega = .0
do 1212 i=1,200
c z1=z0 + 0.1d0*i
omega=0.001+i-1.d0
c write(*,*) "omega=", omega
call gxomega(gxom1,zz,r,omega)
call gradcoeff(coeff1,zz,r,omega)
call gxomega(gxom2,zzz,r,omega)
call gradcoeff (coeff2,zzz,r,omega)
gxom=gxom1-gxom2
grgxom = coeff1*gxom1 - coeff2*gxom2
c call fzomr (fr,omega,z,r)
c dz = .001d0
c zpdz= z+dz
c call fzomr (fr1,omega,zpdz,r)
c grgrfr = (fr1 - fr) /dz
call grfzomr ( grfr,omega,z,r)
```

```
c write (*,*) 'grgrfr',grgrfr,'grfr',grfr
c fr = fr + gxom
grfr = grfr + grgxom
c write (*,*) 'z1',z1,'ratio',grfr
c write (*,*)'omega',omega,'ratio',grfr
grfrmag=cdabs(grfr)
greal=real(grfr)
gimag=imag(grfr)
if (greal .gt. 0.0 .and. gimag .gt. 0.0 ) then
grfphi=atan(gimag/greal)
endif
if (greal .lt. 0.0 .and. gimag .lt. 0.0 ) then
grfphi=3.14 +atan(gimag/greal)
endif
if (greal .lt. 0.0 .and. gimag .gt. 0.0) then
grfphi=3.14+atan(gimag/greal)
endif
if (greal .gt. 0.0 .and. gimag .lt. 0.0) then
grfphi=6.28+atan(gimag/greal)
endif
write (10,101)omega,grfrmag,grfphi
c write (*,*)omega,greal,gimag
```

```
c write (*,*) 'z1',z1,'fr',fr,'gxom',gxom
101 format(1x,1e10.5,1x,1e10.5,1x,1e10.5)
c write (*,*) 'z1',z1,'grfr',grfr,'grgxom',grgxom
111 format (2(e12.4,x))
c write (*,*) t,ft
c write (*,*) t,gxt
1212 continue
stop
end
subroutine gzrt (gt,z, r, t)
implicit double precision (a-h,o-z)
common /pi/pi
common /prop/ d1,bl1,d2,bl2,n1,n2
xx = r*r + z*z
d1t=d1* dabs (t)
expg1=dexp(-xx/4.d0/d1t)
expg2=dexp(-d1t/bl1/bl1)
gt=d1/(4.d0*pi*d1t)**1.5*expg1*expg2
return
end
subroutine GXOMEGA (gxom, zz,r ,omega)
implicit double precision (a-h,o-z)
```

```
double complex cap0,cap1,cc,cc1,gxom
common /prop/ d1,bl1,d2,bl2,n1,n2
common /pi/pi
cap01=1.d0/bl1/bl1
cap02= - omega/d1
cap0=dcmplx(cap01,cap02)
cap1=cdsqrt(cap0)
absx=dsqrt(zz*zz+r*r)
cc= -cap1*absx
cc1= cdexp(cc)
pix=4.d0*pi*absx
gxom=cc1 / pix
return
end
subroutine gradcoeff (coeff,zz,r,omega)
implicit double precision (a-h,o-z)
double complex cap0,cap1,coeff
common /prop/ d1,bl1,d2,bl2,n1,n2
common /pi/pi
cap01=1.d0/bl1/bl1
cap02= - omega/d1
cap0=dcmplx(cap01,cap02)
```

```
cap1=cdsqrt(cap0)

absx=dsqrt (zz*zz + r*r)

coeff = -zz/absx*(cap1 + 1.d0/absx)

return

end

subroutine fzrt(ft,z,r,t)

implicit double precision (a-h,o-z)

double complex fom

common /pi/pi

common /prop/ d1,bl1,d2,bl2,n1,n2

common /bound/z0,z1

weightb=1.d0/3.d0

weight1=4.d0/3.d0

weight2=2.d0/3.d0

ddd=dmax1(d1,d2)

xxxx=dmin1(r,z1,bl1,bl2)

omm=ddd/xxxx/xxxx

omegamin=omm*1.d-8

nt=20

stepomega= 2.d0*pi /t/nt

stepomega = dmin1 (stepomega, omm/nt)

ccccccccccccccccccccccccccccccc
```

```
omegamin0 = stepomega * 1.d-8
ccccccccccccccccccccccccccccc
omegamin=omegamin0
ccccccccccccccccccccccccccccc
n=nt
omegamax0=dfloat (2*n)*stepomega
omegamax = omegamax0
ccccccccccccccccccccccccccccc
sum0 = 0.0d0
10 continue
call fzomr (fom,omegamin,z,r)
c call gxomega (fom,z-z0,r,omegamin)
fom1=dbleq(fom)
fom2=dimag(fom)
foms=fom1*dcos(omegamin*t)+fom2*dsin(omegamin*t)
foms= 2.d0* foms
sum=sum0 + weightb*stepomega*foms
call fzomr (fom,omegamax,z,r)
c call gxomega (fom,z-z0,r,omegamax)
fom1=dbleq(fom)
fom2=dimag(fom)
foms=fom1*dcos(omegamax*t)+fom2*dsin(omegamax*t)
```

```
foms= 2.d0* forns

sum = sum + weightb* stepomega*foms

do 15 i= 1,n

omega = omegamin + stepomega *float(2*i-1)

call fzomr (fom,omega,z,r)

c call gxomega (fom,z-z0,r,omega)

fom1=dbleq(fom)

fom2=dimag(fom)

foms=fom1*dcos(omega*t)+fom2*dsin(omega*t)

foms= 2.d0* foms

sum = sum + weight1* stepomega*foms

c write (*,*)'i',i,'sum',sum

15 continue

do 17 i= 1,n-1

omega = omegamin + stepomega *float(2*i)

call fzomr (fom,omega,z,r)

c call gxomega(fom,z-z0,r,omega)

fom1=dbleq(fom)

fom2=dimag(fom)

foms=fom1*dcos(omega*t)+fom2*dsin(omega*t)

foms= 2.d0* foms

sum = sum + weight2* stepomega*foms
```

```
c write (*,*)'i',i,'sum',sum
17 continue
accur = dabs ((sum0-sum)/sum)
if (accur.le.1.d-3) go to 19
sum0=sum
omegamin = omegamin + omegamax0
omegamax = omegamax + omegamax0
c write (*,*)'sum',sum,'accur',accur,'omegamax',omegamax
go to 10
19 continue
ft = sum /2.d0/pi
return
end
subroutine fzomp (f,z,omega,p)
implicit double precision (a-h,o-z)
double complex c1,c2,c3,c4
double complex dcap1,dcap2,cap1,cap2,f,b,bn,bd
double complex cont1,cont2,cont3
common /prop/ d1,bl1,d2,bl2,n1,n2
common /bound/z0,z1
common/pi/pi
c write (*,*),'come in fzomp',p
```

```
p2=p*p

c11= p2+1.d0/bl1/bl1

c12 = -omega/d1

c1=dcmplx(c11,c12)

c21= p2+ 1.d0/bl2/bl2

c22= -omega/d2

c2= dcmplx (c21,c22)

cap1 = cdsqrt(c1)

cap2= cdsqrt(c2)

*******calculation B

c2= cap1*z0

**************

c1 = cdexp(-c2)

bn = 1.d0-c1*c1

dcap1 = d1 * cap1

c dcap2 = d2 * cap2 modified on 5-9-95

dcap2 = d2 *cap2*((n2/n1)**2)

bn = bn * (dcap1-dcap2)

*****************

c1=dcap1 + dcap2

c2=dcap1 - dcap2

c3= 2.0d0 * z1 *cap1
```

```
c3 = cdexp(-c3)

bd = c2 * c3 + c1

b = bn / bd

******************b***********

*******calc cont1****

c1 = -dabs(z-z0)*cap1

cont1= cdexp( c1)

********cont2*******

c1 = -(z+z0)* cap1

cont2 = cdexp (c1)

********cont3*********

c1 = cap1 * (z - 2.d0*z1 + z0)

c2 = cap1 *(-z - 2.d0*z1 + z0)

c3 = cdexp (c1)

c4 = cdexp (c2)

c1 = c3 - c4

cont3 = b * c1

********************

ccccccccccccccccccccccccccctest cccccccj

cont1=0.d0

cont2=0.d0

c1 = cont1 - cont2
```

```
c2 = c1 + cont3

c3 = 4.d0 * pi * cap1

*************************

f = c2 / c3

************

c write (*,*) 'f',f,'z',z,'omega',omega,'p',p

return

end

***********gradient*************

subroutine grfzomp (grf,z,omega,p)

implicit double precision (a-h,o-z)

double complex c1,c2,c3,c4

double complex dcap1,dcap2,cap1,cap2,grf,b,bn,bd

double complex cont3

common /prop/ d1,bl1,d2,bl2,n1,n2

common /bound/z0,z1

common/pi/pi

c write (*,*),'come in grfzomp',p

p2=p*p

c11= p2+1.d0/bl1/bl1

c12 = -omega/d1

c1=dcmplx(c11,c12)
```

```
c21= p2+ 1.d0/bl2/bl2

c22= -omega/d2

c2= dcmplx (c21,c22)

cap1 = cdsqrt(c1)

cap2= cdsqrt(c2)

*******calculation B

c2= cap1*z0

*************

c1 = cdexp(-c2)

bn = 1.d0-c1*c1

dcap1 = d1 * cap1

c dcap2 = d2 * cap2 modified on 5-9-95

dcap2 = d2 * cap2*((n2/n1)**2)

bn = bn * (dcap1-dcap2)

*****************

c1=dcap1 + dcap2

c2=dcap1 - dcap2

c3= 2.0d0 * z1 *cap1

c3 = cdexp(-c3)

bd = c2 * c3 + c1

b = bn / bd

*****************b***********
```

```
********cont3*********

c1 = cap1 * (z - 2.d0*z1 + z0)

c2 = cap1 *(-z - 2.d0*z1 + z0)

c3 = cdexp (c1)

c4 = cdexp (c2)

***** next line is for density********

c1 = c3 - c4

***** next line is for z-gradient of density******

c1 = cap1 * (c3 + c4)

cont3 = b * c1

*******************

ccccccccccccccccccccccccccctest cccccccj

c2 = cont3

c3 = 4.d0 * pi * cap1

*************************

grf = c2 / c3

************

c write (*,*) 'grf',grf,'z',z,'omega',omega,'p',p

return

end

subroutine fzomr(fr,omega,z,r)

implicit double precision (a-h,o-z)
```

```
      double complex f,fr,sum,sum0
      common/bound/ z0,z1
      common /pi/pi
c     write (*,*),'come in fzomr'
      ne=10
      pmin0=0.d0
c     pmax0=2.3d0*ne/z0
      pmin=pmin0
c     pmax=pmax0
      nb=50.d0
      step= dmin1 (pi/r,1.d0/z1)/nb
c     ng=nint((pmax-pmin)/pstep/2.) + 1
      ng=100
      pmax0=step * ng*2.d0
      pmax=pmax0
c     n = 2* ng
c     step = (pmax-pmin)/float(n)
      sum0=dcmplx (0.d0,0.d0)
110   continue
      weightb=1.d0/3.d0
      weight1=4.d0/3.d0
      weight2=2.d0/3.d0
```

```
***************

call fzomp (f,z,omega,pmin)

besp= pmin*bessj0(pmin*r)

sum = sum0 + f *besp*weightb*step

************

call fzomp (f,z,omega,pmax)

besp=pmax*bessj0(pmax*r)

sum = sum +f *besp*weightb*step

*****************

do 10 i=1,ng

p1= pmin + step*float(2*i-1)

besp=p1*bessj0(p1*r)

call fzomp(f,z,omega,p1)

sum =sum + f *besp*weight1*step

10 continue

do 20 i=1,ng-1

p2= pmin + step*2.d0*float(i)

besp=p2*bessj0(p2*r)

call fzomp(f,z,omega,p2)

sum = sum + f *besp*weight2*step

20 continue

************
```

```
if (sum.eq.0.d0)then
write (*,*)'in fzomr fr=0'
go to 19
else
endif
accur= cdabs((sum-sum0)/sum)
call resterm (rest,r,pmax, dabs(2.d0*z1-z-z0))
accur1= rest/cdabs(sum)
c write (*,*)'pmax',pmax,'sum',sum,'accur',accur,'accur1',accur1
sum0=sum
pmin=pmin + pmax0
pmax=pmax + pmax0
if (accur.le.1.d-3.and.accur1.le.1.d-3) go to 19
go to 110
19 continue
fr=sum
return
end
********** gradient continues**********
subroutine grfzomr(grfr,omega,z,r)
implicit double precision (a-h,o-z)
double complex f,grfr,sum,sum0
```

```
common/bound/ z0,z1
common /pi/pi
c write (*,*),'come in fzomr'
ne=10
pmin0=0.d0
c pmax0=2.3d0*ne/z0
pmin=pmin0
c pmax=pmax0
nb=50.d0
step= dmin1 (pi/r,1.d0/z1)/nb
c ng=nint((pmax-pmin)/pstep/2.) + 1
ng=100
pmax0=step * ng*2.d0
pmax=pmax0
c n = 2* ng
c step = (pmax-pmin)/float(n)
sum0=dcmplx (0.d0,0.d0)
110 continue
weightb=1.d0/3.d0
weight1=4.d0/3.d0
weight2=2.d0/3.d0
***************
```

```
call grfzomp (f,z,omega,pmin)

besp= pmin*bessj0(pmin*r)

sum = sum0 + f *besp*weightb*step

**********

call grfzomp (f,z,omega,pmax)

besp=pmax*bessj0(pmax*r)

sum = sum +f *besp*weightb*step

**********

do 10 i=1,ng

p1= pmin + step*float(2*i-1)

besp=p1*bessj0(p1*r)

call grfzomp(f,z,omega,p1)

sum =sum + f *besp*weight1*step

10 continue

do 20 i=1,ng-1

p2= pmin + step*2.d0*float(i)

besp=p2*bessj0(p2*r)

call grfzomp(f,z,omega,p2)

sum = sum + f *besp*weight2*step

20 continue

**********

if (sum.eq.0.d0)then
```

```
write (*,*)'in grfzomr grfr=0'
go to 19
else
endif
accur= cdabs((sum-sum0)/sum)
call grresterm (rest,r,pmax, dabs(2.d0*z1-z-z0))
accur1= rest/cdabs(sum)
c write (*,*)'pmax',pmax,'sum',sum,'accur',accur,'accur1',accur1
sum0=sum
pmin=pmin + pmax0
pmax=pmax + pmax0
if (accur.le.1.d-3.and.accur1.le.1.d-3) go to 19
go to 110
19 continue
grfr=sum
return
end
double precision function bessj0(x)
c function bessj0(x)
implicit double precision (a-h,o-z)
c real*8 y,p1,p2,p3,p4,p5,q1,q2,q3,q4,q5,r1,r2,r3,r4,r5,r6,
c * s1,s2,s3,s4,s5,s6
```

```
data p1,p2,p3,p4,p5/1.d0,-.1098628627d-2,.2734510407d-4,
* -.2073370639d-5,.2093887211d-6/, q1,q2,q3,q4,q5/-.1562499995d-
*1,
* .1430488765d-3,-.6911147651d-5,.7621095161d-6,-.934945152d-7/
data r1,r2,r3,r4,r5,r6/57568490574.d0,-13362590354.d0,651619640.7d
*0,
* -11214424.18d0,77392.33017d0,-184.9052456d0/,
* s1,s2,s3,s4,s5,s6/57568490411.d0,1029532985.d0,
* 9494680.718d0,59272.64853d0,267.8532712d0,1.d0/
c  write (*,*),'bessj0'
if(abs(x).lt.8.)then
y=x**2
bessj0=(r1+y*(r2+y*(r3+y*(r4+y*(r5+y*r6)))))
* /(s1+y*(s2+y*(s3+y*(s4+y*(s5+y*s6)))))
else
ax=abs(x)
z=8.d0/ax
y=z**2
xx=ax-.785398164d0
bessj0=sqrt(.636619772d0/ax)*(cos(xx)*(p1+y*(p2+y*(p3+y*(p4+y
* *p5))))-z*sin(xx)*(q1+y*(q2+y*(q3+y*(q4+y*q5)))))
endif
```

```
return
end
subroutine resterm (rest, r, p0, alpha)
implicit double precision (a-h,o-z)
common/pi/pi
rest=1.d0/4.d0/pi
rest=rest * dsqrt (2.d0/pi/r/p0)
rest=rest * dexp( - alpha *p0) *(alpha + r)
rest= rest/(alpha*alpha + r*r)
return
end
subroutine grresterm (rest, r, p0, alpha)
implicit double precision (a-h,o-z)
common/pi/pi
rest=1.d0/4.d0/pi
rest=rest * dsqrt (2.d0/pi/r*p0)
rest=rest * dexp( - alpha *p0) *(alpha + r)
rest= rest/(alpha*alpha + r*r)
return
end
```

A.2 Program to calculate the pulse profile for a rectangular slab using photon flux for chapter 5.

```
#ifndef lint
#static char sccsid[] = "@(#)subslab1.r 1.5 95/05/19";
#endif
# program subslab1.r: basic subroutine program to compute
# temporal profile of point input transmitted through
# point to point inside a slab
# ------------------------------
# Modified 26/1/91 to include error standard.
# Diffusion  5/1/90 modified to fix lt, change
# length, absorption considered.
# from Lax Theory
# ------------------------------
# INPUT:
# time:  vv (ps)
# xx1:  lt (um); xx2:  la (um); wd:  thickness (um);
# sor:  source position-z direction (um);
# sord:  source detection distance-z direction(um)
# rad:  source detection distance-radius direction(um);
# dex:  index; uu :  OUTPUT
#------------------------------
```

```
 subroutine gg(vv,xx1,xx2,wd,wdy,sor,sory,sord,sordy,rad,dex,uu)
 implicit double precision (a-h,o-z)
 common /fun1/pi,d,theta,theta1,dif,t,h,thetay,theta1y
 if (vv <= 0.)  { uu=0.
 }
 else {
# ------------------------------
# parameters
ero=1.e-6
z0=0.71*xx1 # for boundary condition
d=wd+2.*z0
h=wdy+2.0*z0
#ddsor=sor+z0 #5/19/95, sor is from real slab boundary, add extra length
ddsor=sor+2.0*z0 #7/16/95
#ddsory=sory+z0
ddsory=sory+2.0*z0 #7/16/95
pi=3.14159654
tsord=sord-z0 #7/16/95
#print*,sord
tsordy=sordy-z0 #7/16/95
theta=tsord
thetay=tsordy
```

```
theta1=2*ddsor+tsord

theta1y=2*ddsory+tsordy

dif=.1*xx1/dex # diffusion coefficient =vl/3 (um**2/fs)

ale=.3/xx2/dex #absorption coefficient

ddia=rad**2*.25/dif

# end parameters

# ---------------------------

t=vv*1000.  # t time (fs)

call sum(ero,cjj,m)

# print*,m

uu=cjj*exp(-t*ale)*exp(-ddia/t)/sqrt((4.*pi*dif*t)**3)/(2.*t)

# print*, "cjj,uu",cjj,uu

 }

 end

####

# function subroutine, func(m)

subroutine func(m, funcm)

implicit double precision (a-h,o-z)

 common /fun1/pi,d,theta,theta1,dif,t,h,thetay,theta1y

 fm=float(m)

 if(m .gt.0) {

 ff1=theta-2.*float(m)*d
```

```
 ffn1=theta+2.*float(m)*d
 ff2=theta1-2.*float(m)*d
 ffn2=theta1+2.*float(m)*d
#
 term=ff1*exp(-ff1**2/4./dif/t)+ffn1*exp(-ffn1**2/4./dif/t)
 term2=ff2*exp(-ff2**2/4./dif/t)+ffn2*exp(-ffn2**2/4./dif/t)
 funcm=term-term2
 }
 else {
 funcm=theta*exp(-theta**2/4./dif/t)-theta1*exp(-theta1**2/4./dif/t)
 }
# print*,"term1,term2",term,term2
#
 end #end of function
# function subroutine, funcb(m)
subroutine funcb(m,funcmb)
implicit double precision (a-h,o-z)
common /fun1/pi,d,theta,theta1,dif,t,h,thetay,theta1y
fm=float(m)
if(m .gt.0) {
ff1=thetay-2.*float(m)*h
ffn1=thetay+2.*float(m)*h
```

```
ff2=theta1y-2.*float(m)*h

ffn2=theta1y+2.*float(m)*h

#

termb=exp(-ff1**2/4./dif/t)+exp(-ffn1**2/4./dif/t)

term2b=exp(-ff2**2/4./dif/t)+exp(-ffn2**2/4./dif/t)

funcmb=termb-term2b

}

else {

funcmb=exp(-thetay**2/4./dif/t)-exp(-theta1y**2/4./dif/t)

}

# print*,"termb,term2b",termb,term2b

end #end of function

####

####

# subroutine to do infinite sum to certain accuracy,

# SUM (from m=0 to m=inf) func(m)

# func(m) is a subroutine.

subroutine sum(err,sumf,m)

implicit double precision (a-h,o-z)

tero=1.

call func(0,sum0)

m=1    #initial condition
```

```
call func(m,sumf) #initial term
 sumf=sumf+sum0
 if ( abs(sumf) .lt.  1.0e-100 ) {
 sumf=0.0
 }
 else {
 while (tero .gt.  err ) {
 nstart=m+1
 nfinish=2*m
 dsum=0. # added part
 do i=nstart, nfinish {
 call func(i,funci)
 dsum=dsum+funci
 }
 sumf=sumf+dsum
 m=nfinish
# print*,"sumf=",sumf
 if (sumf .eq.  0.)  {tero=1
 }
 else {
 tero=abs(dsum/sumf)
 }
```

```
 }
 }
# print*,"tero=",tero
tero=1.
call funcb(0,sum0b)
m=1    #initial condition
call funcb(m,sumfb) #initial term
 sumfb=sumfb+sum0b
 if (abs(sumfb) .lt.  1.0e-100) {
 sumfb=0.0
 }
 else {
 while (tero .gt.  err ) {
 nstart=m+1
 nfinish=2*m
 dsumb=0. # added part
 do i=nstart, nfinish {
 call funcb(i,funci)
 dsumb=dsumb+funci
 }
 sumfb=sumfb+dsumb
 m=nfinish
```

```
# print*,"sumfb",sumfb
 if (sumfb .eq. 0.) {tero=1
 }
 else {
 tero=abs(dsumb/sumfb)
 }
# print*,"tero",tero
 }
 }
# print*, "here"
 sumf=sumf*sumfb
# print*, "sumf,sumfb",sumf,sumfb
 end
```

A.3 A program to fit intensity profile.

```
#ifndef lint
#static char sccsid[] = "@(#)fit2.r 1.3 92/11/26";
#endif
# Program fit2.r
# date 11-30-91,
# for diffusion eq.  fit
# must be linked with taurosv.f
#
# for infinite slab, point to point source
# ------------------------------
# must linked with function subroutine
# sublaxpl4.r, and taurosv.f
# ------------------------------
#
 subroutine fcn(npar, g,f,x,iflag)
 implicit double precision ( a-h, o-z)
 character * 12 anam, outfile
 character * 60 comfle,comfle1
 real*8 y(1024), z(1024),zz(1024), w(1024), x(6), c(1024)
 go to (10,60,60,60,120) iflag
10 print *, "enter infile"
```

```
 read *, anam
 open(1,file=anam)
 print *, "enter outfile"
 read *, outfile
 open(8,file=outfile)
# print *, "index, and pinhole diameter(um)" #activate this line
 # when using this fit prog.  with sublaxpl4.r
# read*, dex,pdia
 print*,"index, and source detector radial separation=0 for box" #
 # activate this when using this fit prog.  with subslabj.j.
 read*,dex,pdia
 print*,"source-detector in the y-direction"
 read*,sordy
 print*, "thickness (um)"
 read*, wd
 print*, "thickness in the transverse direction" #5-27-95
 read*,wdy
 print*, "source position in the z direction(um)" #with subslabj.r
 read*,sor
 print*,"source position in the y-direction"
 read*,sory
 print*, "source-detector z-separation(um)" #with subslabj.r
```

```
 read*,sord
 ymax=0.
 yto=0.
 #read(1,*)comfle,comfle1
 print *, "yes"
 #read(1,*)ddjunk, ddjunk1
 do i=1,1024 {
 read (1,*,end=222)w(i), c(i)
 y(i) = c(i)
 if (y(i).gt.ymax) {ymax=y(i)
 }
# #if (y(i).lt.0)y(i)=0.
}
222 n=i-1
 nn=n-1
 do m=1,nn {
 yto=yto+(y(m)+y(m+1))*(w(m+1)-w(m))/2.
 }
# write(6,*)"area=",yto
# do i=1,1024 { ###
# y(i)=c(i)/ymax ###
# } ###
```

```
# yymax=ymax ###
# ymax=1.0 ###
# print*, "yymax,ymax", yymax,ymax
60 f=0.0
 zmax=0.
 zto=0.
# print*," I am about to call gg"
 do i=1,n {
# call gg(w(i),x(1),x(2),wd,dex,pdia,z(i))
# call gg(w(i),x(1),x(2),wd,sor,sord,pdia,dex,z(i)) # this line
  # is activated only when compiling with subslabj.r. If compiling
  # with sublaxpl4.r or sublaxpl42.r activate the previous call line.
call gg(w(i),x(1),x(2),wd,wdy,sor,sory,sord,sordy,pdia,dex,z(i))S () #5-27-95
# z(i)=z(i)*zz(i) #added 5-27-95
# write(33,*)w(i),z(i)
 if(z(i).lt.0) z(i)=abs(z(i))
 if(z(i).gt.zmax) {zmax=z(i)
 }
 }
# print*, "I have called gg",zmax,ymax
 do i=1,n {
 z(i)=z(i)/zmax*ymax*x(3) #equal total intensity
```

```
 #f=f+(z(i)-y(i))*(z(i)-y(i))/sqrt(y(i)*y(i))
 f=f+(z(i)-y(i))*(z(i)-y(i))
# print*,"f ",f
}
 f=f/ymax**2 #add this line when exp. data are small(e-8,e-10,etc. range)
# print*,"2nd f",f
 if (iflag.ne.3) return
120 print *,x(1),x(2),wd
 write(8,*)"%lt=",x(1)
 write(8,*)"%la=",x(2)
 write(8,*)"%thickness=",wd,"norm factor=",x(3)
 write(8,*)"%fcn=",f,"theory max=",zmax
 write(8,*)"%dia=",pdia,"index=",dex
 do m=1,nn {
 zto=zto+(z(m)+z(m+1))*(w(m+1)-w(m))/2.
 }
 rat=yto/zto
 write(8,*)"%total count exp.=",yto
 write(8,*)"%total count theo=", zto,"ratio=exp/theo",rat
 write(8,*)"fitda=["
 do i=1,n {
 com=(z(i)-y(i))/y(i)
```

```
# print*, "z(i)=",z(i)
# z(i)=z(i)*yymax ###
# print*,"z(i),yymax",z(i),yymax
 write(8,111)w(i), z(i)
# write(18,*)w(i),com
}
111 format(1e10.5,1x,1e10.5)
 write(8,*)"];"
 close (8)
# print *, "chi** =",xx
 end
```

Bibliography

Applications of Optical Fourier Transforms edited by H. Stark (Academic Press, New York, 1982).

G. I. Bell and S. Glasstone, *Nuclear reactor theory*, (D. Van Nostrand Company, New Jersey, 1970).

K.M. Case, F. D. Hoffman, and G. Placzek, *Introduction to the theory of neutron diffusion*, (Los Alamos Scientific Lab., New Mexico, 1953).

K. M. Case, P. F. Zweifel, *Linear transport theory*, (Addison-Wesley, Massachusetts, 1969).

Ch. 4

S. Chandrasekhar, *Radiative transfer*, (Oxford University Press, London, 1950).

J. Chang, Y. Wang, R. Aronson, H. L. Graber, R. L. Barbour, B. B. Das, J. Dolne, K. M. Yoo, and R. R. Alfano, "Time-resolved imaging in dense scattering media", SPIE Vol. 1887, 1993.

H. Cheng, Y. Chen, D. Dilworth, E. Leith, J. Lopez, and J. Valdmanis, "Two-dimensional imaging through diffusing media using 150–fs gated electronic holographic techniques," Opt. Lett. **16**, pp. 487–, 1991.

W. Cui and L. E. Ostrander, "The relationship of surface reflectance measurements to optical properties of layered biological media," IEEE Trans. on Biomed. Eng. **39**, pp. 194–201, 1993.

W Cui, N. Wang, and B. Chance, "Study of photon migration depths with time-resolved spectroscopy," Opt. Lett. **16**, pp. 1632–1634, 1991.

M. Cutler, "Transillumination as an aid in the diagnosis of breast lesions," Surg. Gynecol. Obstet., **48**, 721, 1929.

B. B. Das, K. M. Yoo, and R. R. Alfano, "Ultrafast time-gated imaging in thick tissues: a step toward optical mammography," Opt. Lett. **18**, pp. 1092–1094, 1993.

B. B. Das, Ph. D. Thesis, The City Univ. of New York, 1993.

B. Davison, *Neutron transport theory*, (Oxford University Press, London, 1958).

J. J. Dolne, K. M. Yoo, F. Liu, and R. R. Alfano, "IR Fourier Space Gate and Absorption Imaging through random media," Lasers in Life Sciences **6**, pp. 1–11.

J. J. Dolne, M. Klibanov, F. Liu, S. Gutman, and R. R. Alfano, "Detection of a scattering layer inside a three-layered scattering medium," edited by R. R. Alfano, B. Chance (SPIE, Washington, DC, 1995) Vol. 2389.

J. J. Duderstadt and L. J. Hamilton, *Nuclear reactor analysis*, (Wiley, New York, 1976).

R. L. Egan, Breast Imaging: Diagnosis and Morphology of Breast Diseases, (W. B. Saunders Company, Pa, 1988).

S. Feng, F. Zeng, and B. Chance, "Perturbation theory of photon migration in the presence of a single defect," OSA Proceedings in Optical Imaging and Photon Migration, R. R. Alfano, ed. (Optical Society of America, Washington, DC, 1994) Vol. 21, pp. 217–228.

K. Furutsu, "Diffusion equation derived from the space-time transport equation," J. Opt. Soc. of Am. **70**, 360–366, 1980.

K. Furutsu, "Diffusion equation derived from the space-time transport equation in anisotropic random media," J. Math. Phys. **21**, 765–777, 1980.

N. Garcia, A. Z. Genack, and A. A. Lisyansky, "Measurement of the transport mean free path of diffusing photons," Phys. Rev. B, **46**, pp. 14475–14479, 1992.

A. Z. Genack, "Optical transmission in disordered media," Phys. Rev. Lett. **58**, 2043–2046, 1987.

J. W. Goodman, *Introduction to Fourier Optics*, (McGraw Hill, New York, 1968).

A. H. Grandjbakhche, G. H. Weiss, R. F. Bonner, and R. Nossal, "Photon path-length distributions for transmission through optically turbid slabs," Phys. Rev. E **48**, pp. 810–818, 1993.

J. C. Hebden, R. A. Kruger, and K. S. Wong, "Time Resolved imaging through a highly scattering medium," Appl. Lett. **30**, pp. 788–794, 1991.

A. Hecht, *Optics*, (Addison Wesley, New York, 1987).

P. P. Ho, P. Baldeck, K. S. Wong, K. M. Yoo, D. Lee, and R. R. Alfano, "Time dynamics of photon migration in semiopaque random media," Appl. Opt. **28**, pp. 2304–2310, 1989.

D. Huang, E. A. Swanson, C. P. Lin, J. S. Schuman, W. G. Stinson, W. Chang, M. R. Hee, T. Flotte, K. Gregory, C. A. Puliafito, and J. G. Fujimoto, "Optical coherence tomography," Science **254**, pp. 1178–1181, 1991.

D. Huang, J. Wang, C. P. Lin, C. A. Puliafito, and J. G. Fujimoto, "Micron-resolution ranging of cornea anterior chamber by optical reflectometry," Las. Surg. Med. **11**, 419–425, 1991.

A. Ishimaru, *Wave propagation and scattering in random media*, (Academic Press, New York, 1978).

J. A. Izatt, M. R. Hee, G. Tearny, G. M. Owen, E. Swanson, and J. G. Fujimoto, "Optical coherence microscopy," OSA Proceedings in Optical Imaging and Photon Migration, R. R. Alfano, ed. pp. 249–252, 1994.

M. R. Jerath, D. Kaisig, H. G. Rylander III, and A. J. Welch, "Reflectance feedback control of photocoagulation in vivo," Arch. Ophthalmol., **111**, pp. 531–534, 1993.

M. R. Jerath, D. Kaisig, H. G. Rylander III, and A. J. Welch, "Calibrated real time control of lesion size based on reflectance images," Appl. Opt. **32**, pp. 1200–1209, 1993.

M. Lax, *Symmetry principles in solid state and molecular physics*, (Wiley, New York, 1974).

M. Lax, V. Nayaramamurti, and R. C. Fulton, "Classical diffusive Photon transport in a slab," in Proc. of the Symposium on Laser Optics Of Condensed Matter edited by J. L. Birman, H. Z. Cummings, and A. A. Kaplyanskii (Plenum, New York, 1987), pp. 229–235

J. H. Li, A. A. Lisyansky, T. D. Cheung, D. Livdan, and A. Z. Genack, "Transmission and surface intensity profiles in random media," Europhysics Letters **22**, 675–680, 1993.

F. Liu, Ph. D. Thesis, The City University of New York, 1993.

F. Liu, K. M. Yoo, and R. R. Alfano, "Speed of the coherent component of femtosecond laser pulses propagating through random scattering media," Opt. Lett. 15, pp. 351–353, 1991.

F. Liu, K. M. Yoo, and R. R. Alfano, "Should the photon flux or the photon density be used to describe the temporal profiles of scattered ultrashort laser pulses in random media?," Opt. Lett. **18**, pp. 432–434, 1993.

F. Liu, K. M. Yoo, and R. R. Alfano, "Transmitted photon intensity through biological tissues within various time windows," Optics Lett., **19**, pp. 740–742, 1994.

J. A. Moon and J. Reintjes, "Achievable Image Resolution using non-diffuse multiply scattered light," OSA Proceedings on Advances in Optical Imaging and Photon Migration, edited by R. R. Alfano (Optical Society of America, Washington, DC, 1994), Vol. **21**, pp. 149–152.

P. M. Morse and H. Feshback, *Methods of Theoretical Physics* (McGraw Hill, New York, 1953).

OSA Proceedings on Advances in Optical Imaging and Photon Migration, edited by R. R. Alfano (Optical Society of America, Washington, DC 1994) Vol. 21.

M. S. Patterson, B. Chance, and B. C. Wilson, "Time-resolved reflectance and transmittance for the noninvasive measurement of tissue optical properties," Appl. Opt. **28**, pp. 2331–2336, 1989.

M. S. Patterson, S. Anderson-Engels, B. C. Wilson, and E. K. Osei, "Absorption spectroscopy in tissue-simulating materials: a theoretical and experimental study of photon paths," Appl. Opt. **34**, 22–30, 1995.

M. S. Patterson, B. W. Pogue, and B. C. Wilson, "Computer simulation and experimental studies of optical imaging with photon density waves," SPIE Vol IS11, Medical Optical Tomography: Functional Imaging and Monitoring, pp. 513–533, 1993.

L. T. Perelman, J. Wu, I. Itzkan, Y. Wang, R. Dasari, and M. S. Feld, "Photon paths in turbid media: Theory and Experimental observation," OSA Proceedings on Advances in Optical Imaging and Photon Migration, edited by R. R. Alfano (Optical Society of America, Washington, DC, 1994), Vol. **21**, pp. 153–155.

A. Ya. Polishchuk and R. R. Alfano, "Fermat photons in turbid media: An exact analytic solution for most favorable paths- a step towards optical tomography," submitted to Phys. Rev. Lett.

A. Ya. Polishchuk and R. R. Alfano, " "Fermat" photons in random media: Diffusion on the velocity sphere and principle of the least mean-square curvature," submitted to Phys. Rev. Lett.

OSA Proceedings on Advances in Optical Imaging and Photon Migration, edited by R. R. Alfano (Optical Society of America, Washington, DC 1994) Vol. 21.

A. E. Profio, "Light transport in tissue," Appl. Opt., **28**, pp. 2210–2215, 1989.

L. Reynolds, "Optical diffuse reflectance and transmittance from an anisotropically scattering finite blood medium," Ph. D. Dissertation, Seattle, 1975.

J. M. Schmitt, G. X. Zhou, and E. C. Walker, "Multilayer model of photon diffusion," J. Opt. Soc. A. 7, pp. 2141–2153, 1990.

K. Shimizu, A. Ishimaru, L. Reynolds, and A. P> Bruckner, "Backscattering of a picosecond pulse from densely distributed scatterers," Appl. Opt. **18**, pp3484, 1979.

J. R. Singer, F. A. Grunbaum, P. Kohn, and J. P. Zubelli, "Image reconstruction of the interior of bodies that diffuse radiation," Science **248**, 990–993, 1990.

S. L. Sobolev, Partial Differential Equations of Mathematical Physics, (Pergamon Press, New York, 1964).

SPIE series on Medical Optical Tomography: Functional Imaging and Monitoring, edited by G. J. Muller (SPIE, Washington, DC, 1993) Vol. IS11.

SPIE Proceedings on Photon Migration and Imaging in Random Media and Tissues, edited by B. Chance, R. R. Alfano (SPIE, Washington, DC, 1993) Vol. 1888.

I. Stakgold, *Green's Functions and Boundary Value Problems*, (John Wiley and Sons, New York, 1979).

H. Taitelbaum, S. Havlin, and G. H. Weiss, "Approximate theory of photon migration in a two-layer medium," Appl. Opt. **28**, 2245–2249, 1989.

S. Takatani and M. D. Graham, "Theoretical analysis of diffuse reflectance from a two-layer tissue model," IEEE Trans. Biomed. Eng. **BME-26**, pp. 656–664, 1979.

H. C. van de Hulst, *Light Scattering by Small Particles*, (Dover, New York, 1981).

L. Wang, P. P. Ho, C. Liu, G. Zhang, and R. R. Alfano, "Ballistic 2–D imaging through scattering walls using an ultrafast optical Kerr gate," Science **253**, pp. 769–771, 1991.

L. Wang, P. P. Ho, and R. R. Alfano, "Time-resolved Fourier spectrum and imaging in highly scattering media," Appl. Opt. 32, pp. 5043–5048, 1993.

K. M. Yoo, Ph. D. Thesis, The City University of New York, 1990.

K. M. Yoo and R. R. Alfano, "Time-resolved coherent and incoherent components of forward light scattering in random media," Opt. Lett. **15**, pp. 320–322 1990.

K. M. Yoo, K. Arya, G. C. Tang, J. L. Birman, and R. R. Alfano, "Coherent backscattering of a picosecond pulse from a disordered medium: Analysis of pulse shape in the time domain," Phys. Rev. A, **39**, pp. 3728–3731, 1989.

K. M. Yoo, F. Liu, and R. R. Alfano, "When does the diffusion approximation fail to describe photon transport in random media ?," Phys. Rev. Lett. **64**, pp. 2647–2650.

K. M. Yoo, F. Liu, and R. R. Alfano, "Imaging through a scattering wall using absorption," Opt. Lett. **16**, pp. 1068, 1991.

K. M. Yoo and R. R. Alfano, "Determination of attenuation lengths arising from scattering and absorption from the temporal profile of the back-scattered pulse," Opt. Lett. **15**, pp. 276 , 1990.